**UNIVERSITA' DEGLI STUDI DI NAPOLI FEDERICO II**

**Nicola Marrocco**

# ULTRAFAST PHOTORESPONSE OF SUPERCONDUCTOR/FERROMAGNET HYBRID NANOSTRUCTURES

**A dissertation submitted to the Dipartimento di Scienze Fisiche**

**In fulfillment of the requirements for the degree of PHILOSOPHIAE DOCTOR**
***in***
***Tecnologie Innovative per Materiali, Sensori ed Imaging***

**XXII CICLO (2007-2009)**

# Introduction

Even if modern electronics seems to be steadily based on silicon technology and more generally on semiconductor based devices, the research is deeply involved into the discovery and investigation of new solutions to the continuous request for always better performances. The choice of the materials is a possible way to proceed in searching for advanced functionalities. Not for case, INTEL electronics developed hafnium (Hf) gate based MOSFET to be engineered into the last families of multi-core processors or HEMT (High Electron Mobility Transistors) gallium-arsenide (GaAs) based devices able to reach hundreds of GHz operating frequencies very useful in radio-space applications. Ultra-fast computers, communication channels and relative industry answers with respect to Moore's law are requested.

Superconducting materials and devices, starting from the beginning of the last century, represent a very important target: the future outlook of a technological mind is "cold" and "light".

What really slowed a wider development of superconductors within industrial application has been probably the needed cryogenics (for electronics down to liquid helium temperature -273°C or less for novel quantum applications). Cold fingers system based on recycling of helium gas represents enough cheap systems which demonstrated to be good for allocating high quality factor filters for telecommunication applications or low noise SQUID amplifiers. Josephson junction based electronics also reached very interesting performances: beside high critical temperature superconducting cuprates (HTS) devices operating at liquid nitrogen temperature, many efforts are nowadays done toward the realization of high speed computing modules for numerical simulations in various fields such as biochemistry, particle physics, etc..

Among superconducting electronics applications, the development of advanced detectors present one of the field more explored by the scientific community in the last decades. Recently, the search for novel and high performances optical detectors has achieved a great interest due to particular characteristics and potentials proper of the superconducting state.
In fact, when the optical wavelength to be detected is confined up to the near-infrared radiation, superconducting technology offer the better answers in terms of response time, wavelength responsivity, quantum efficiency, and minimum detectable power. Superconducting devices are inherently fast and are ultrasensitive because of their quantum nature and low-noise cryogenic operation environment. The low energy gap, i.e. the miniu energy to create electron excitations by breaking cooper pairs, is two to three orders of magnitude lower than in a semiconductor; thus a photon absorption in a superconducting detector creates an avalanche electron charge two to three orders of magnitude higher for the same photon energy. This leads to the enhancement of the sensitivity to reach the ultimate limit-single quantum detection, extends the range of detectable energies well beyond the infrared part of the radiation spectrum, and results in an enhanced energy resolving device. Superconducting devices offer the viability of a broadband, single quantum detectivity, and picosecond response time quantum detector. They also offer very low dark currents and very low noise, a typical feature for any cryogenic electronic element.

Actually, NbN is the most used material for the development of advanced superconducting single photon nanowire detectors, and its high performances have been already demonstrated in many experiments also in in quantum optics and astrophysics. The work of this thesis aims to investigate the role of proximity effect which exists when a superconductor is in close contact with a normal metal, in photoresponse experiments on micro- and nano-sized wire-shaped devices employing both niobium and niobium nitrate (both low critical temperature SC) as "active" materials. These choices have mainly been suggested by the fast dynamics showed by electron excitations produced after the absorption of some external radiation. The investigation has been mainly focused on weak ferromagnetic materials used as thin overlayers on both Nb and NbN thin films, and they demonstrated to be very interesting not only for photoresponse results but also for involved fundamental physics aspects.

Some general theoretical descriptions about superconductivity, later used to analyze the experimental data, are briefly presented in Chapter 1 together with the working principle of a superconducting nanowire detectors.

The photoresponse mechanisms occurring in a superconducting material are presented and discussed in Chapter 2, including the energy cascade occurring after the photon absorption, the main scattering processes involving electrons, phonons and Cooper pairs, and the basic modeling used for obtaining the time dependence of both electron and phonon temperatures during the first picoseconds after photon absorption.

The main properties of the proximity effect between a superconductor and a normal metal in good electrical contact are presented in Chapter 3. Moreover, the extension of the theoretical modelling to superconducting/ferromagnetic bilayers is also discussed. The formalism is later used for calculating electron densities of states of S/F heterostructures, an important parameter for discussing all optical experiments.

In Chapter 4 and 5, the fabrication processes/technologies and measurement systems (cryogenics, electronics, optical pump-probe, photo-impedance, etc.) used to perform experiments on superconducting samples are presented.

Chapter 6 contains transient reflectivity measurements on Nb and Nb/NiCu thin film bilayers, and NbN and NbN/NiCu heterostructures. Results are discussed in terms of nonequilibrium physics and proximity effect.

Finally, in Chapter 7 the photo-response experiments performed on various nanowires fabricated in collaboration with the University of Saitama, Japan, are presented and discussed. The role of proximity effect and vortex physics are also introduced in the data analysis. Moreover, the accomplishments of the work performed in the thesis are presented, and some thoughts on future works are also given.

# 1. Superconducting nanowires as advanced photodetectors

## 1.1 Superconductivity: historical prelude

It was in 1911 that the superconductivity was first discovered by Hike Kamerlingh Onnes, the Nobel laureate for his pioneering work in low temperature physics and for liquefactions of helium. In his experiment, the resistance of mercury decreased sharply to zero when the temperature was decreased to around 4.2 K [1]. The temperature at which the materials changed from the normal state to the superconducting state was later termed as the superconducting transition temperature $T_C$. In the following years it was discovered that the superconducting state is very common in metals, composite and alloy, even if in most case the critical temperatures are well below 1 K.

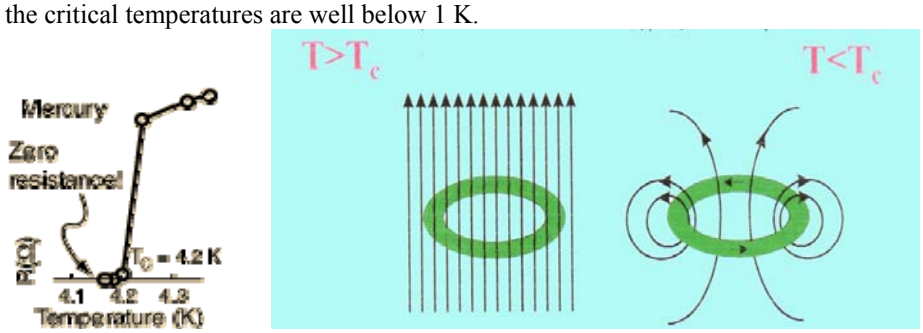


**Fig.1.1** (left) the critical temperature of a mercury wire; (right) self sustaining current and filed onto a superconducting ring.

The unique nature of the superconductivity appear clearly for a superconducting ring at $T>T_C$ in presence of a magnetic field. Lowering the temperature and then removing the field at $T<T_C$, the supercurrent previously induced in the ring persist indefinitely. Two years after his discovery of the superconductivity, Onnes found that the superconducting state could be suppressed if the superconductor was biased by a current higher than a critical value of $I_C$ or a magnetic field higher than a critical value of $H_C$. The dependence of $H_C$ on temperature is well represented by the phenomenological law:

$$\frac{H_C(T)}{H_C(0)} = 1 - \left(\frac{T}{T_C}\right)^2 \tag{1.1}$$

where $H_C(0)$ is the critical magnetic field at 0K. Another intriguing effect (the so called Meissner effect) which is characteristic of the superconducting state was discovered in 1933 by W. Meissner and R. Ochsenfeld. They saw that a superconducting material in the presence of a magnetic field at a temperature above $T_C$ is crossed by the field lines, according to the classical magnetism laws. But when the temperature is lowered below $T_C$, the magnetic field is expelled from the material, and the material became perfectly diamagnetic (Fig. 1.2).

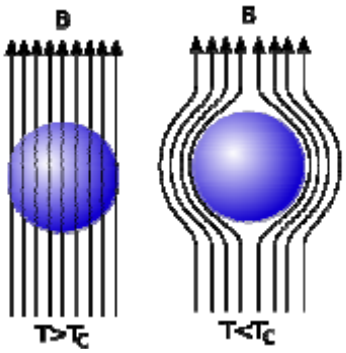


**Fig. 1.2** The Meissner effect

In order to take in account the Meissner effect, F. London and H. London (1935) developed a superconducting electrodynamics [2]. This model defines a clear explanation of the diamagnetic properties of superconductors in terms of surface supercurrents. Moreover, the model introduce a characteristic length, the London penetration dept $\lambda_L^2$, for the decay of the local magnetic field $h(r')$ in the material according to the equation:

$$\nabla^2 h(\vec{r}) = \frac{1}{\lambda_L^2} h(\vec{r})$$
$$\lambda_L = c\sqrt{\frac{m}{4\pi n_S e^2}} \quad (1.2)$$

$\lambda_L$ depends on the microscopic nature of the material: $n_S$ - density of superconducting electron, $m$ - electron mass, $e$ – absolute value of the electron charge, $c$ – light velocity.
The existence of a precise value of magnetic field above which the superconductor returns into the normal state also at $T<T_C$ is a characteristic of a limited class of superconductors, namely the "type I" superconductors. For the wider class of "type II" superconductors we have to distinguish two critical magnetic fields: $H_{C1}(T)$ under which the material is superconducting, and $H_{C2}(T)$ above which the material is a normal conductor. Within the intermediate values, the material is in a "mixed state" characterized by an incomplete Meissner effect: magnetic field lines partially penetrate into the material and produce "vorteices" of current with a conductive normal core (Abrikosov vortices, see further).
In 1950, Ginzburg and Landau, developed a generalized theory to describe cases in which the macroscopic wavefunction describing the superconducting state can change also in space [3]. From this theory naturally comes out a characteristic parameter $\chi = \lambda_L / \xi$ that relates $\lambda_L$ with $\xi$, the Pippard correlation length, that describe the characteristic length on which the density of superconducting electron can change. Finally, in 1957, J. Bardeen, L. N. Cooper and J. R. Schrieffer proposed the famous microscopic theory of superconductivity, the BCS theory [4], which successfully explained most of the phenomena in metallic superconductors. The BCS theory is based on the concept that electrons with opposite spins and momenta in the superconducting state are paired with each other by exchanging a virtual particle, i.e. phonon arising from the second quantization of lattice vibrations. The pairs of electrons are called Cooper pairs after L. N. Cooper, who first introduced this idea. The combination energy of Cooper is 2Δ:, to break the Cooper pair, the minimum energy required is 2Δ. This energy is also termed as "energy gap", according to a semiconductor-like description, but nevertheless it separates the ground state of paired electrons from the first excited state of quasiparticles. For superconductors the value of 2Δ is of the order of few meV, that is two or three orders of magnitude lower than that of semiconductors (e.g. for silicon $E_G$= 1.12 eV at room temperature). Nevertheless, it is important to stress that There is no any physical analogy between 2Δ and $E_G$, even if it is helpful to compare these values in many cases where analogies should be done with many analogous electronic devices coming from the semiconducting side. According to BCS theory, the energy gap 2Δ of a superconductor is related to its critical temperature Tc by the relation:

$$2\Delta(0) = 3.52 k_B T_C \quad (1.3)$$

where 2Δ(0) is the energy gap at temperature of zero Kelvin. The energy gap is maximized at 0 K and decreases to zero when $T$ is approaching $T_C$ . Such a bevaviour can be phenomenologically expressed as $\Delta(T) = 3.2 k_B T_C (1-T/T_C)^{1/2}$ when $T$ is approaching $T_C$. Thus, for a NbN film, with $T_C$=16K, the energy gap at 0 K is 4.85 meV, which corresponds to a wavelength of 255.5 μm. The extremely low 2Δ value makes superconductors very promising candidates for photon detectors in a wider spectral range (even beyond far-IR range) than semiconductors. Richards and Tinkham have measured far-IR photon absorption above 2Δ energy gap for selected conventional superconductors [5] as early as in 1960. Successive studies on High $T_C$ superconductors have been performed to investigate the possibility of realize a single photon detector working at liquid nitrogen temperature. Hegmann *et al* in 1994 has demonstrated picoseconds photoresponse for epitaxial $YBa_2Cu_30_{7-d}$ thin films [6]. Nevertheless, at the moment no single photon detector based on High $T_C$ superconductors has been demonstrated mostly due to the extreme difficulty to realize good quality ultra thin films, and to the difficulty to pattern them in a nanowire geometry, necessary to obtain the right sensitivity.

## 1.2 Detection principles

Practical quantum communications (QC) and, in particular, quantum cryptography are limited by the low efficiency and low counting rates of currently available single-photon detectors. The popular Si avalanche photodiodes (APD's) have their sensitivity restricted by the Si bandgap, so they cannot be directly implemented in the standard near-infrared (NIR) fiber-optic communication systems, while

photomultipliers are bulky and demonstrate low (<1%) quantum efficiency (QE) for detection of radiation with a wavelength longer than 1μm. In addition, semiconductor APD's have to be used in a time-gated mode to reduce dark counts that typically reduces their counting rates to 10 MHz or below. APD's are also characterized by parasitic after-glowing phenomena due to spontaneous photon emission during the intrinsic avalanche process. Limited performance of Si APD's in the NIR radiation range is the major current constraint for fiber-based QC. The modern telecom industry has already established standard fiber-optic wavelengths for communication: 1.3 μm and 1.55 μm. The NIR range also seems ripe for future free-space communication applications. The material of choice for semiconductor APD's at NIR is InGaAs. The InGaAs APD's in the 1.2- to 1.6-μm range have already achieved QE >20% in single-photon detection mode, but they suffer from large timing jitter and high (>$10^4$ per second) dark counts, as well as the other problems typical for APD's such as afterpulsing and afterglowing. The practical counting-rate limit of InGaAs devices is about a few kHz [7], resulting in the highest-achievable speed of the QC channel reduced down to hundreds of bits per second [8].
Superconducting devices are very attractive as radiation sensors because of their quantum nature and low-noise cryogenic operation environment. In addition, the superconducting energy gap 2Δ is two to three orders of magnitude lower than the gap in semiconductors; thus, each absorbed optical photon is able to generate a large number of secondary excited carriers, when hitting a superconducting detector [9].Submicron-width NbN superconducting nanostructures [10] demonstred to be high efficiency superconducting single-photon detector (SSPD) for its ultrafast timing, high sensitive for both the visible and NIR photons, and very low dark counts [11]. These devices have already found practical applications for non-contact debugging of CMOS very-largescale integrated circuits [12], and are now being implemented in practical QC systems. Efficient and fast SSPD's are also of great interest for other single photonics applications, such as single-molecule fiuorescence, high-resolution astronomy, and quantum metrology.

### 1.2.1 Ultrathin superconducting nano-bridge : the working principle

Upon absorption of a light quantum hν by a Cooper pair, a highly excited electron is created [13]. Due to the large physical size (coherence length) of a Cooper pair, only one electron absorbs a photon, while the second one becomes a low-energy quasiparticle (QP). Next, this excited (very hot) electron extremely rapidly (on a femtosecond time scale) loses its energy via electron-electron (e-e) scattering and creation of secondary electrons. The e-e process continues until the average energy of excited electrons is approximately the Debye energy): at this time the most efficient mechanism for redistribution of energy becomes the emission of Debye phonons by electrons (e-ph process). The mean free path of these phonons is very small, and they efficiently break additional Cooper pairs. As the average energy of electrons in the avalanche decreases down to values close to the energy gap 2Δ, their number increases, reaching ideally $h\nu/2\Delta$. the effective electron temperature Te increases locally during this energy cascade, resulting in local suppression of superconductivity and formation of a hotspot. The time evolution of the hotspot depends on the various QP and phonon relaxation processes, which are highly nonlinear: in fact, phonons emitted during the energy cascade can have enough energy to break other pairs, leading to the so-called phonon bottleneck, limited by the phonon escape time from the superconductor.

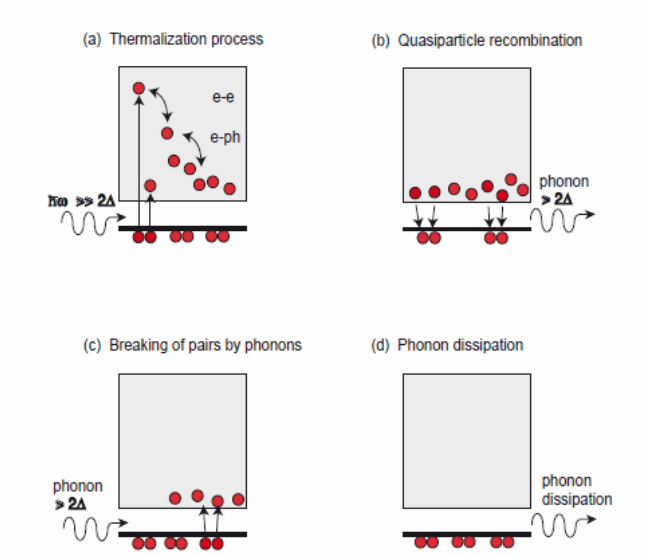


**Fig.1.3** Avalanche process in a superconductor excited by an optical phonon [14].

Fig. 1.3 schematically illustrates the dynamics of a photon absorption process in a superconductor and the subsequent nonequilibrium generation and relaxation of QP's. A single 800-nm-wavelength photon is able to produce in an ultrathin superconducting NbN film a cascade consisting of >300 QP's on a time scale (phonon escape) of less than 30 ps [15]. As we will show later, in SSPD's the QP avalanche results in an electrical pulse and allows for a precise detection of the photon arrival, while the picosecond QP relaxation ensures GHz repetition rates for superconducting NbN photon counters.

## 1.2.2 The Hot-Spot model

The operating SSPD consists of a superconducting stripe of a submicrometer width (comparable with the QP diffusion length and the hotspot size, whose radius is roughly the electron thermalization length $\lambda_T$ [13]. The device is maintained at a temperature lower than the superconducting transition Tc and it is biased at a current I close to the critical current Ic . The photoresponse mechanism is schematically presented in Fig. 1.4.

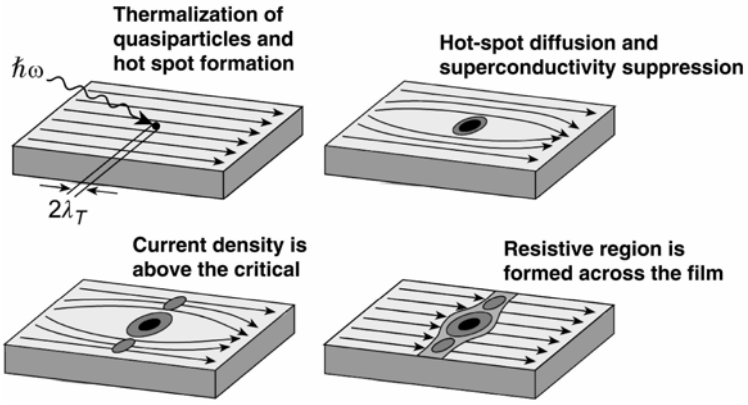


**Fig. 1.4** Schematics of the hotspot generation and supercurrent-assisted formation of a resisteive barrier in an ultrathin and sub-micron width superconducting stripe kept al temperature far below $T_c$. Arrows indicate flow direction of biasing supercurrent [13].

After photon absorption, a localized hotspot region, with suppressed or even destroyed superconductivity, is formed within the initial hotspot [Fig. 1.4(a)]. The initial hotspot size is determined by the $h\nu/2\Delta$ ratio, as well as the QP thermalization time and its diffusivity. During the e-ph thermalization, the hotspot grows [Fig. 1.4(b)] as hot electrons diffuse out of the hotspot core. The supercurrent, which biases the device, is expelled from the resistive hotspot volume and is concentrated in the "sidewalks" near the edges of the film [Fig. 1.4(c)]. If the current density after this redistribution exceeds the critical value outside the hotspot, phase-slip centers are formed in quasi one-dimensional sidewalks, and a resistive

barrier is established across the entire width of the device [Fig.1.4(d)]. This resistive barrier gives a rise to a voltage signal with the amplitude proportional to I. After the growth phase, the hotspot starts to decrease due to the relaxation and out-diffusion of excited QP's. Thus, in ultra-thin NbN, after about 30ps of relaxation time, the hotspot collapses, superconductivity is restored (zero voltage state) and the detector is ready to detect another photon [16].

## 1.3 Single Photon detectors

### 1.3.1 Superconducting nanowire Single Photon Detectors (SPD)

According to the detection mechanism described in the previous sub-section, Gol'tsman et al [16], in 2001 firstly experimentally demonstrated the supercurrent-assisted, hotspot- detection mechanism for single optical (790 (?) nm wavelength) photons. Fig. 1.5 shows a current–voltage (I –V) characteristics of a NbN microbridge (Fig. 1.6) operated at 4.2 K and voltage biased. The characteristics is typical of a long superconducting constriction [17] and show that the bridge can be operated in either of the two distinct modes: the superconducting and the resistive state. The hotspot plateau under dc conditions corresponds to the growing normal-state region, as the voltage across the device is increased, eventually reaching the bridge normal-state resistance. The thick, dashed line represents a 50Ω load line, when the device is connected to the output microwave transmission line.

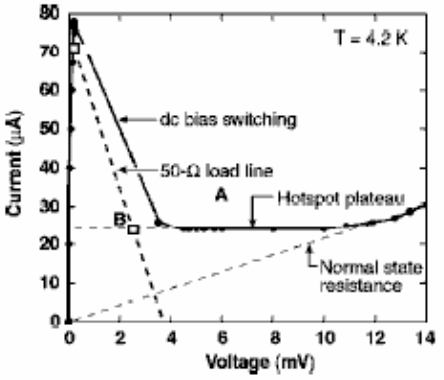


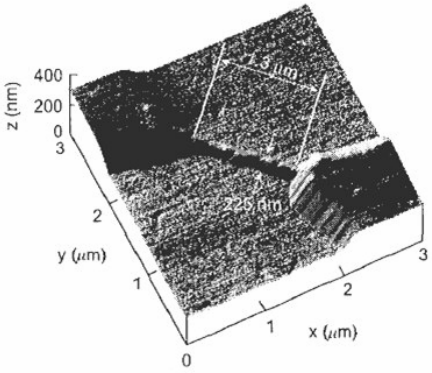


**Fig.1.5 (left)** *I –V* characteristics of a 0.2 mm wide and 1.2 mm long NbN superconducting microbridge are shown. Point A denotes the initial detector bias level in the superconducting state and point B corresponds to the switched state upon absorbing a photon, leading a voltage pulse generation, before relaxing back to point A.
**Fig.1.6 (right)** AFM image of a 1.3 μm x 0.23 μm microbridge device. [18]

. For a device biased near, but below $I_C$ (point A in Fig. 1.5), photon absorption triggers the supercurrent-assisted hotspot formation leading to a temporary switching from the superconducting state to the hotspot resistive state (point B in Fig. 1.5) along the 50 Ω load line. As a result, an output voltage is generated with a magnitude corresponding to the voltage level at point B, which is independent on the actual photon energy, as long as the photon energy is sufficient to form a hotspot large enough to trigger the supercurrent redistribution effect. The response time of the voltage pulses followed the formation and subsequent healing of the resistive state induced by the photon absorption [19]. (see Fig.1.7 )

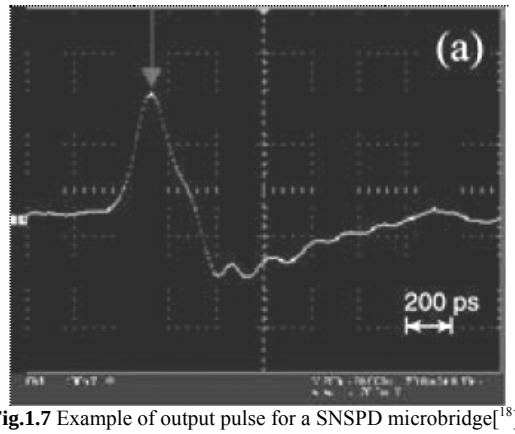


**Fig.1.7** Example of output pulse for a SNSPD microbridge[18].

Fig. 1.8 shows a collection of 'snapshots' recorded by a 1 GHz bandwidth oscilloscope for different energies per laser pulse, incident on the SSPD. Each snapshot presents an 80 ns long record of the response to six successive 100 fs wide pulses and was randomly selected out of a real-time detector output data stream. Trace A in Fig. 1.8 corresponds to an average of 100 photons per pulse hitting the detector. In this case, the SNSPD responded to each optical pulse in the laser train. The same 100%-efficient response was observed (trace B) when there were approximately 50 photons per pulse. As the incident laser intensity was further decreased (with other experimental conditions unchanged), the quantum nature of the detector response emerged. Instead of the linear decrease of the signal amplitude with incident light intensity, which is characteristic of the classical detector, the response amplitude of the single-photon SNSPD remained nominally the same. In addition, some of the response pulses were missing because of the limited quantum efficiency of the device as well as fluctuations in the number of photons incident on the detector. The quantum voltage response of the SNSPD is most apparent in the bottom two pairs of traces: C and D (five photons/pulse) and E and F (one photon/pulse). Each pair corresponds to two different randomly selected records obtained under exactly the same experimental conditions. Note that in each case the detector response is very different. Averaging over a long observation time, however, showed that both the average number of captured pulses and their magnitude remained constant if the pulse energy was unchanged. This unambiguously demonstrated the single photon operation of the device.

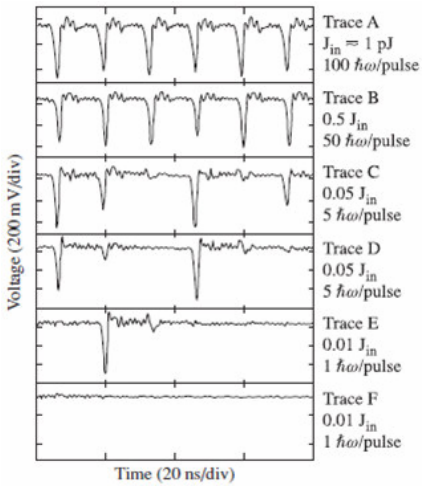


**Fig.1.8** Response of an NbN quantum detector to trains of 100 fs optical pulses with a different number of photons per pulse [18].

For a mean number of photons per pulse ($m$), the probability $P(n)$ of absorbing $n$ photons from a given pulse is proportional to:

$$P(n) \cong \frac{e^{-m}(m)^n}{n!} \tag{2}$$

When the mean number of photons $m$ « 1 (achieved, e.g. by attenuating the radiation fluence to reduce the total number of photons incident on the detector to an average of much less than one photon per pulse):

$$P(n) \cong \frac{m^n}{n!} \tag{3}$$

Consequently, for very weak photon fluxes, the probability of detecting one photon, two photons, three photons, etc is:

$$P(1) \cong m, P(2) \cong \frac{m^2}{2}, P(3) \cong \frac{m^3}{6}, etc. \tag{4}$$

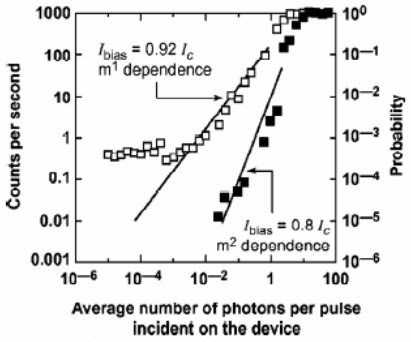


**Fig.1.9** Count rates and the corresponding counting probability for an NbN quantum detector as a function of the radiation intensity. Depending on bias current, the detector can count single-photon (open squares) or two-photon (solid squares) events[18].

Fig. 1.9 shows the probability of the detector producing an output voltage pulse as a function of the number of photons per pulse incident on the device area, at two different values of the bias current. The left vertical axis indicates the mean number of detector counts per second. The right vertical axis corresponds to the probability of detecting an optical pulse. Open squares correspond to the bias current $0.92I_C$, where $I_C$ is the critical current at the operation temperature. Saturation occurs at high incident photon fluxes. For smaller fluxes, as predicted by equation (3), the experimental data show the linear decrease of detection probability with the average number of incident photons over four orders of magnitude, clearly demonstrating the single-photon detection. At very low photon doses, experimental data points saturate at the level of 0.4 $s^{-1}$ counts (probability $4 \times 10^{-4}$) since the experiment was performed in an optically unshielded environment. This level is regarded as the laboratory photon background. The solid squares in Fig. 1.9 correspond to the same device, operated under the same conditions as those for the open-square data, but biased with $0.8I_C$. Experimental data points now follow a quadratic dependence of detection probability (see equation (4)), showing the two-photon detection. As expected for a two-photon process, the quantum efficiency is significantly lower than that for the single-photon detection. At the same time, the photon background is no longer observed since the probability of two uncorrelated, stray photons hitting the device within its response duration is negligibly small.

## 1.3.2 Quantum Efficiency and Noise Equivalent Power

The detection mechanism in this type of device is based on the overcoming of the density of critical current in the superconductive path around the hotspot created by the absorbed photon. The hotspot extension depend on the energy of the incident photon, so in order to have a good sensibility to very low energy photons (like Infra-Red photons) a very narrow nanowire is needed. Typical nanowires have a width of the order of 100 nm. On the other hand a so narrow detector has a very low active area, thus is very difficult to efficiently couple the incident light to the device. In order to increase the active area a meander structure is used (Fig. 1.10).

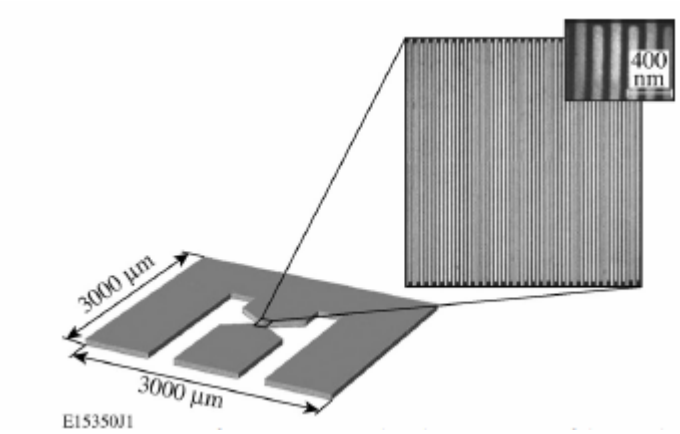


**Fig.1.10** Topology of SNSPD contact pads and an SEM image of the meander (NbN is black)[18]. The contact pads allow connection to a 50- coplanar transmission line.

The efficiency of radiation detector is usually measured by a parameter, called Quantum efficiency, defined by the ratio of the number of detected photon *NREG* and of the number of incident photons *NINC*, for a given time interval per the device area [20]:

$$QE = \frac{N_{REG}}{N_{INC}} \tag{21}$$

In continuous wave measurements, the value was determined from the power incident on the device nominal active area measured by a power meter. In experiments with pulsed sources, experimental QE is simply the probability of photon counting, measured at the one photon-per-pulse level, incident upon the SSPD nominal area and expressed in percent. Fig. 1.11 presents an example of the QE dependence on normalized bias current at two different operating temperatures, for a 4 nm thick and 100 nm wide meander shaped SNSPD, based on a NbN thin film. At 4.2 K, QE for visible light photons reaches a ~30% value. One can also note in Fig. 1.11 an evidence of QE saturation at 0.56 μm wavelength and T= 4.2 K. The saturation-like behavior is, however, more obvious looking at the 2 K, for 0.56 μm data. Furthermore, for visible light, the decrease of the operating temperature below 4.2 K did not lead to any improvement in QE. Thus, the observed saturation means that in the visible range, this SNSPD detects every photon absorbed by the superconducting NbN film. From the application point of view, the most interesting are the telecommunication 1.3 μm and 1.55 μm wavelengths. The QE at these wavelengths at 2 K is also presented in Fig. 1.11. One can see that at 1.3 μm, the QE also reaches 30% saturation value, while at 1.55 μm, the maximum QE is 17%. At 4.2 K, the QE for IR light is quite far from saturation. For example, the maximum QE at 1.55 at 4.2 K is only 3.7% and only for $I_B$ approaching $I_C$.

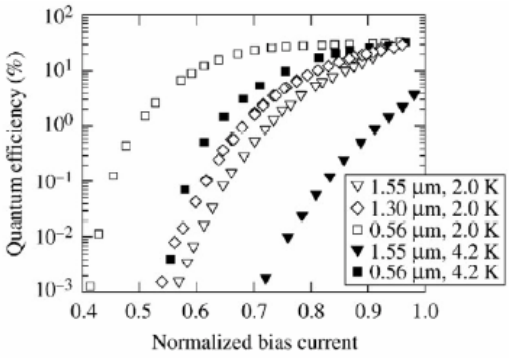


**Fig.1.11** Quantum Efficiency measured at different wavelengths at 4.2K and 2.0K temperature [18]

Even when the SNSPD is in a complete dark condition, the device produces spontaneous voltage pulses similar to the photoresponse pulses. These pulses are called dark counts and their rate is defined as their mean number occurring during a defined time (for example 1 s). Fig. 1.12 presents an example of the dark-count rate $R$ versus $I_B$. The curve follows a typical activation law dependence:

$$R = a \cdot \exp\left( b \frac{I_B}{I_C} \right) \tag{22}$$

with a and b constant.

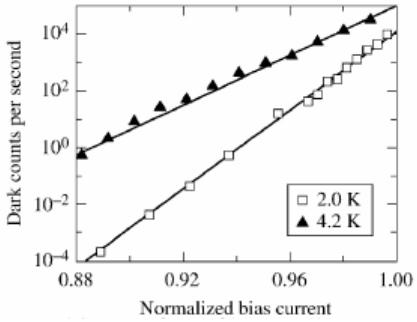


**Fig.1.12** SSPD dark counts versus normalized bias current at temp. of 4.2K and 2.0K [18] .

An optimal operation regime of the SSPD is a trade-off between QE and *R*. The maximum value of QE corresponds to rather high (~1000 $s^{-1}$ or above). Quantitatively this interplay between QE and R can be presented in terms of the noise equivalent power (NEP) [20], which can be defined for quantum detectors as:

$$NEP = \frac{h\upsilon}{QE}\sqrt{2R} \tag{23}$$

where $h\nu$ is photon energy. In Fig. 1.13 is shown the NEP as function of the bias current at 4.2 K filled symbol and 2.0 K open symbol.

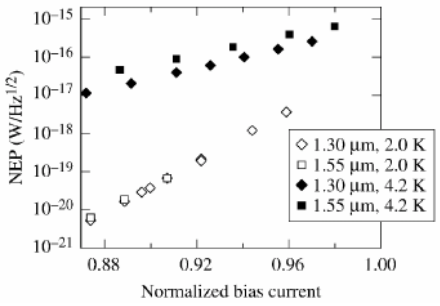


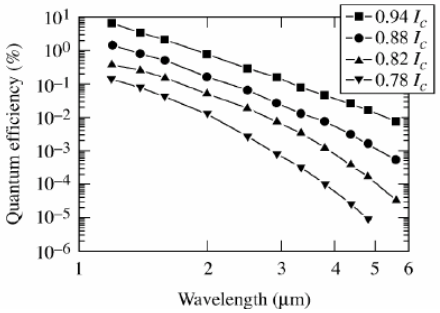


**Fig.1.13 (left)** The SSPD NEP at 4.2K (closed symbols) and 2.0K (open symbols), calculated for 1.3 μm (diamonds) and 1.55 μm (squares) using the experimental R and QE values from Figs. 19 and 20, respectively [13]

**Fig.1.14 (right)** Spectral sensitivity (QE versus wavelength) of SSPD measured at 3K for $I_B$ in the range of 0.78 to 0.94 $I_C$ .

References:
[1] H. K. Onnes; "The superconductivity of mercury"; *Comm. Phys. Lab. Univ. Leiden*, vol 120, 1911.
[2] F. London, H. London; "The electromagnetic equation of the superconductors"; *Proc. Roy. Soc. A*, vol 149, no./pp. 71, 1935.
[3] V. L. Ginzburg, L. D. Landau; "On the theory of superconductivity"; *Zh. Eksperim. I Teor. Fiz.*, vol 20, no./pp. 1064, 1950.
[4] J. Bardeen, L. N. Cooper, J. R. Schrieffer; "Theory of superconductivity"; *Phys. Rev.*, vol 108, no./pp. 1175, 1957.
[5] P. L. Richards, M. Tinkham; "Far-infrared energy gap measurements in bulk superconducting In, Sn, Hg, Ta, V, Pb, and Nb"; *Phys Rev.*, vol 119, no./pp. 575, 1960.
[6] F. A. Hegmann, R. A. Hughes, J. S. Preston; "Picosecond photoresponse of epitaxial YBa2Cu307-d thin films"; *Appl. Phys. Lett.*, vol. 64, no./pp. 23, 1994.
[7] G.Ribordy et alter Applied Optics 37,2272,1998
[8] R.J.Highes et alter,New Journal Physics 4,43,2002
[9] K.S.Ill'in,I.I.Milostnaya,A.A.Verevkin,G.N.Gol'tsman,E.M.Gershenzon, R.Sobolewski, Appl.Phys.Lett. 73,3938,1998
[10] G.N.Gol'tsman et alter, Appl.Phys.Lett. 79,705,2001
[11] A.Verevkin et alter,Appl.Phys.Lett. 80,4687,2002
[12] J.Zhang et alter,Electron.Lett. 39,1086,2003
[13] Goltsman et alter, Phys.Stat.Sol.(c), Vol. 2, N.5,1480-1488,2005
[14] Marat Kafizov, PhD Thesis,Photoresponse mechanism of Superconducting MgB2,Rochester University,2007

[15] K.S.Il'in, I.I.Milostnaya,A.A.Verevkin,G.N.Gol'tsman,E.M.Gershenzon and R.Sobolewski, Appl. Phys.Lett. 73,3938,1998

[16] G. N. Gol'tsman, O. Okunev, G. Chulkova, A. Lipatov, A. Semenov, K. Smirnov, B. Voronov, A. Dzardanov, C. Williams, R. Sobolewski; "Picosecond superconducting single-photon optical detector"; *Appl. Phys. Lett.*, vol. 79, no./pp. 705, 2001.

[17] W. J. Skocpol, M. R. Beasley, M. Tinkham; "Self-heating hotspots in superconducting thin-film microbridges"; *J. Appl. Phys.*, vol. 45, no./pp. 4054, 1974.

[18] Orlando Quaranta,PhD thesis,Development and characterization of innovative Superconductive Nanowire Single Photon Detectors, Univ.degli studi di Salerno,2008

[19] A. D. Semenov, G. N. Gol'tsman, A. A. Korneev; "Quantum detection by current carring superconducting film"; *Physica C*, vol. 351, no./pp. 349, 2001.

[20] A. Korneev, V. Matvienko, O. Minaeva, I. Milostnaya, I. Rubtsova, G. Chulkova, K. Smirnov, V. Voronov,G. Gol'tsman, W. Słysz, A. Pearlman, A. Verevkin, R. Sobolewski; "Quantum Efficiency and Noise Equivalent Power of Nanostructured, NbN, Single-Photon Detectors in the Wavelength Range From Visible to Infrared"; *IEEE Trans. Appl. Supercond.*, vol. 15, no./pp. 2, 2005.

# 2. Superconducting Photoresponse Mechanism

## 2.1 The energy cascade: characteristic times and energies

In the previous chapter (see 1.2.1), the thematic of hot spot creation caused by a photon absorption by superconducting thin layer has been introduced. A deeper analisys is needed to clear up the behaviour of the superconductor, considered as constituted by 4 sub-systems , i.e. quasiparticles, Cooper pairs, phonons in the film and phonon in the substrate, each of them interacting energetically.

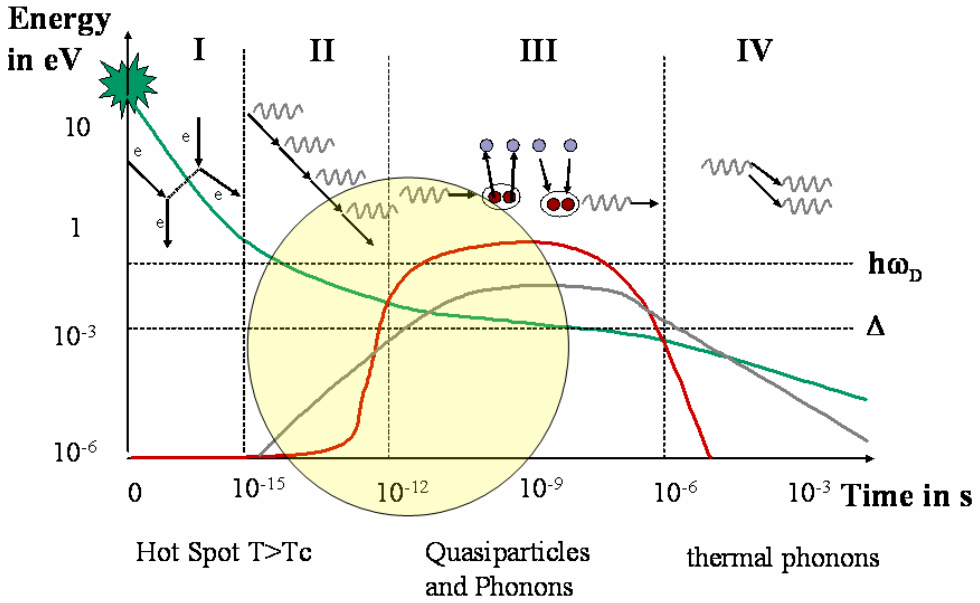


**Fig.2.1** Energy cascade of electron-phonon interactions.

When a photon, with an energy much higher then the Fermi energy, interact with a superconductor, produce a non-equilibrium state whose characteristics depends on the energy of the incident radiation. The energy deposited by the incident photon is relaxed through a "cascade" that ends with an excess of electron (quasiparticles) and phonons. Being the typical energy of the incident photons (≥ 1 eV) much higher than the energy gap (≅ 1 meV) and of the Debey energy (≅tenths ofmeV), the primary radiation-material interaction will not produce quasiparticle. These will be produced only during a secondary interaction phase. To describe the correctly the quasiparticle generation process is helpful to divide the energy cascade in three phase, defined by the characteristic energy and time.

**First stage:**

At the begin the primary excitation generate principally high energy electron .For example the adsorption of a photon of energy $E_0$ of the order of keV in the superconductor generate a photo-electron of energy $E_0$-$E_B$, where $E_B$ is the binding energy of the atomic shell of the photo-electron. The relaxation of the excited atom can happen by emission of photon (fluorescence), or emission of Auger electrons. The fluorescence photon can be adsorbed or not by the superconductor depending on the propagation direction and on the thickness of the material. The Auger electrons lose their energy by ionization. So the major relaxation process of the primary and secondary electrons is the electron-electron interaction, by which, after $10^{-12}$÷$10^{-11}$ s from the arrival of the incident photon, the electron system has reached an equilibrium effective temperature (the primary and secondary electrons have the same energy) higher than the phonon system, with an average energy of the order of eV [21].

**Second stage**

When the energy of the excited electrons reach a value of the order of $\sqrt{E_F \hbar\omega_D} \cong 100meV$ , with $\omega_D$ maximum Debye frequency and $E_F$ Fermi energy, the electron-phonon interaction becomes relevant and on a time scale of the order of $10^{-9}$ s from

the arrival of the incident photon the electron and phonon system thermalize in a new non-equilibrium distribution [21]. At the end of this second phase of the relaxation process will be an excess of quasiparticles of energy $E \cong \Delta$ and phonons of energy $\Omega \leq 2\Delta$. This second stage of the relaxation process is quite complex and it is determined by the time evolution of the energy distribution of the excess quasiparticles and phonons compared to the thermal equilibrium. Schematically can be described in terms of different process, depending on the energy scale $E$ compared to the Fermi energy $E_F$:

- $\sqrt{E_F \hbar\omega_D} < E < 1eV$ , most of quasiparticles production by pair braking via electron-electron interaction.
- $\hbar\omega_D - \Delta < E < \sqrt{E_F \hbar\omega_D}$ , still the most of quasiparticles production by electron-electron interaction, while the electron energy relaxation occurs by the emission of phonons. The maximum energy for phonons $\omega_D$ limit the production of quasiparticles with $E > \hbar\omega$ .
- $2\Delta \leq E \leq \hbar\omega_D - \Delta$, the quasiparticles come out from various process, over the electron-electron interaction and electron-phonon interaction, becomes dominating the pairs breaking process by phonons interaction, with consequent production of two quasiparticles. In fact, quasiparticles with energy $E > 2\Delta$ emit preferably phonons by electron phonon interaction, being small the probability of recombination. Moreover, phonons emitted by an electron-phonon process in which the quasiparticle has an initial energy lower than $3\Delta$ don't have sufficient energy to brake Cooper pairs. Quasiparticles with $E > 3\Delta$ contribute to the quasiparticle production only by electron-electron interaction process.
- $\Delta < E < 2\Delta$, the quasiparticles reach the minimum of energy and cannot produce more quasiparticles. The process active at this energy are the electron-phonon interaction and the quasiparticles recombination with emission of phonon.

The phonon produced during the radiation-material interaction can be distinguished in high energy phonons $2\Delta < \Omega < \hbar\omega_D$ , and low energy phonons $\Omega < 2\Delta$ . The first are generally produced by the electron-phonon interaction of quasiparticles of energy $\hbar\omega_D < E < \hbar\omega_D - \Delta$ and can produce other quasiparticles by pairs brake. The low energy phonons cannot produce other quasiparticles, and the phonon system reach the thermal equilibrium by diffusion.

**Third stage**

In the last stage the system returns to the initial thermal equilibrium, characterized by a temperature equal to the bath temperature, principally by quasiparticles recombination and emission of phonon in the substrate. This is the regime used for describing bolometric response.

## 2.2 Interaction models

### 2.2.1 The 2T model

The 2 temperature model is most relevant for non-equilibrium superconductors maintained at temperature $T$ near the superconducting transition temperature $T_C$, where quasiparticles and phonons can be described by thermal, normal-state distribution functions, each with its own effective temperature (second stage). The electron and phonon effective temperatures ($T_E$ and $T_P$) are assumed to be established instantly and uniformly throughout the whole specimen. This assumption implies that a rapid thermalization mechanism exists inside each subsystem. The main steps of the hot-electron phenomenon that lead to the global equilibrium are depicted in Fig.2.2.

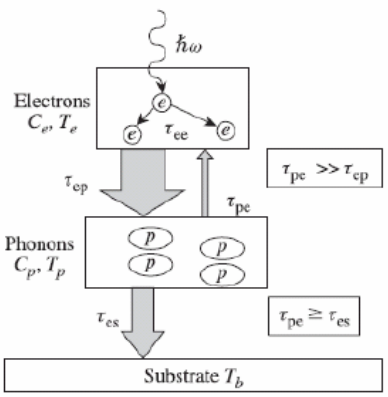


**Fig.2.2** Thermalization scheme showing subsequent channels of the energy transfer in a hot-electron device that relaxes towards global equilibrium.

Introducing characteristic times of the energy exchange between subsystems reduces the problem of the global equilibrium recovery to a pair of coupled heat-balance equations for $T_e$ and $T_{ph}$. The intrinsic thermalization time $\tau_T$ should be short compared to energy exchange times. This two-temperature (2-T) approach was used for the first time by Kaganov et al [22] to describe steady-state electron heating in metals. Below $T_C$, the electron specific heat exhibits an exponential temperature dependence that makes equations nonlinear for even small deviations from equilibrium. The description can, however, be simplified in the vicinity of $T_C$. At this temperature, the superconducting energy gap is strongly suppressed, concentration of Cooper pairs is very small and unpaired electrons exhibit no significant superconducting peculiarities: they are regarded as normal electrons having the ordinary Fermi distribution function. In the normal state, the specific heat of electrons has a much weaker temperature dependence, which can be neglected for small deviations of $T_e$ from equilibrium. With these assumptions, the equations describing the hot-electron effect in superconductors become linear and can be written as:

$$\frac{dT_e}{dt} = -\frac{T_e - T_{ph}}{\tau_{e-ph}} + \frac{1}{C_e} W(t) \tag{2.1a}$$

$$\frac{dT_{ph}}{dt} = \frac{C_e}{C_{ph}} \frac{T_e - T_{ph}}{\tau_{e-ph}} - \frac{T_{ph} - T_0}{\tau_{es}} \tag{2.1b}$$

where $W(t)$ represents the external perturbation (i.e. the power per unit volume absorbed by the electron subsystem), $t_{e\text{-}ph}$ and $t_{es}$ are the electron energy relaxation time via electron–phonon interaction and the time of phonon escape into the substrate, respectively, $C_e$ and $C_{ph}$ are the electron and phonon specific heats, respectively and $T_0$ is the ambient (substrate) temperature. To derive the 2-T equations the condition of the energy-flow balance in equilibrium $t_{ph\text{-}e}=t_{e\text{-}ph}(C_{ph}/C_e)$, where $t_{ph\text{-}e}$ is the phonon–electron energy relaxation time, has been used. The first implementation of the electron-heating model to superconductors was made by Schklovski [23], who used a more general, nonlinear form of the heat-balance equations to describe hysteresis of the critical current in a thin lead film. An analytical solution of equations (4) was first obtained by Perrin and Vanneste [24] for sinusoidal perturbations and by Semenov et al [25] for an optical pulse excitation. In the latter case, thermalization of electrons was interpreted as an increase of $T_e$. The increase was assumed to occur during a time interval that depended on both the duration of the optical pulse and the intrinsic thermalization time. The model was used to describe the response of superconducting NbN and $YBa_2Cu_3O_{7-\delta}$ (YBCO) films in the resistive state to near-infrared and visible radiation [23, 26]. Fig. 2.3.(a) and 2.3.(b) show a good agreement between experimental signals and the theoretical simulation.

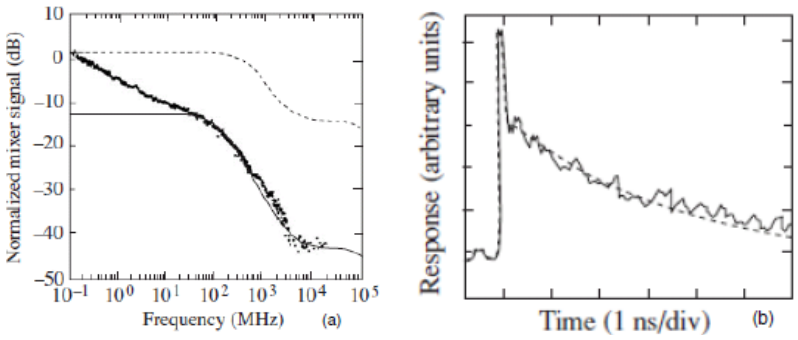


**Fig. 2.3**. (a) Response of a YBCO HEP to optical radiation (dots) versus modulation frequency [24]. The solid line was calculated using equations (1). The discrepancy at low frequencies is due to phonon diffusion in the substrate that was not accounted for in the model. (b) Response of a YBCO HEP to a femtosecond infrared pulse: experimental data (solid line) [22] and simulations (dashedline) based on the 2-T model.

Fitting the equation (4) with experimental photoresponse data has been obtained the following value for YBCO:
• $\tau_T$ = 0.56 ps;
• $\tau_{e\text{-}ph}$ = 1.1 ps;
• $\tau_{es}$ = 3.5 ns;

and the following value for NbN:
• $\tau_T$ = 6.5 ps;
• $\tau_{e\text{-}ph}$ = 10 ps;
• $\tau_{ph\text{-}e}$ = 65 ps;
• $\tau_{es}$ = 38 ps.

From this data is possible to note that, in general, the dynamic of the YBCO thermalization is roughly one order of magnitude faster than that of NbN. In both cases, the energy flow from electrons to phonons dominates the energy backflow due to reabsorption of non-equilibrium phonons by electrons; however, while the energy backflow in YBCO can be neglected because of the very large ratio $C_{ph}/C_e$ = 38, in NbN it constitutes a non-negligible 15% ($C_{ph}/C_e$ = 6.5) of direct electron–phonon energy relaxation. Consequently, in a YBCO film excited on the femtosecond timescale, the nonthermal (hot-electron) and thermal, bolometric (phonon) processes are practically decoupled, with the former totally dominating the early stages of electron relaxation. On the other hand, the response of NbN devices is determined by the 'average' electron-cooling time $\tau_e$, which is given by $\tau_e=\tau_{e\text{-}ph}+(1+C_e/C_{ph})\,\tau_{es}$ [24, 25] and corresponds to the time that elapses from the peak response until the magnitude of the response declines to 1/e of the maximum value. If the external perturbation is substantially longer than $\tau_{ph\text{-}e}$ (that is, >100 ps for YBCO films), the YBCO response is dominated by the bolometric process, as was shown by the bulk of the early photoresponse measurements [26]. The very large difference in the t*es* values for YBCO and NbN is mainly due to the drastic difference in thickness of the tested films. Additionally, NbN films are, in general, better acoustically matched to the substrate. This significantly reduces $\tau_{es}$. Electron heating in the limiting case of a very short phonon escape time, $\tau_{es}\ll\tau_{e\text{-}ph}$, $\tau_{ph\text{-}e}$, was first studied by Gershenzon et al [27] for Nb films. Although for this material [14] $C_{ph}/C_e \cong 0.25$ and, consequently, $\tau_{e\text{-}ph}>\tau_{ph\text{-}e}$, the effective escape of phonons to the substrate prevents energy backflow to electrons. As a result, $\tau_{e\text{-}ph}$ alone controls the response of ultrathin (<10 nm) Nb films. Typical electron relaxation time in Nb is ≅1 ns at 4.2 K, which is over an order of magnitude larger than in NbN. The 2-T model represented by equations (2.1) is essentially the small-signal model. Deviations of the effective temperatures from the equilibrium due to both the joule power dissipated by the bias current and the absorbed radiation power are assumed to be small compared to their equilibrium values. The theory of operation of a hot-electron photodetector (HEP) was developed on the basis of this model by Gershenzon et al [28], and a novel hot-electron mixer (HEM) was proposed [29]. The 2-T approach neglects, however, diffusion of electrons and assumes that the effective temperatures remain uniform within the whole device. A different approach was proposed by Prober [30], who considered diffusion of hot electrons out of the active area, rather than the energy transfer to phonons, as the main

mechanism of the electron cooling. If the device length $L$ is short compared to the thermal diffusion length $L_{th} = \sqrt{D_e \tau_e}$ , where $\tau_e$ is the electron-cooling time and $D_e$ is the electron diffusivity, relaxation of $T_e$ is controlled by the electron outdiffusion time $\tau_D=(L^2/\pi^2 D)$ . In the limiting case $L \ll L_{th}$, $T_e$ remains almost uniform throughout the device length. The device can then be described by equation (2.1.a), in which $\tau_{e\text{-}ph}$ and $T_{ph}$ should be substituted for $\tau_D$ and $T_0$, respectively. For longer devices, both the actual distribution of $T_e$ along the device length and the phonon contribution to the electron relaxation should be taken into account.

## 2.2.2 The Rothwarf and Taylor model

Another well known model for the description of superconductive detectors is the so called Rothwarf and Taylor model, valid especially when for devices that work at a temperature well below the critical temperature and number of excitations is a good physical parameter. Rothwarf and Taylor [31] were the first to successfully develop the phenomenological description for nonequilibrium Cooper-pair recombination and breaking processes. At low temperatures, when energies of nonequilibrium quasiparticles after thermalization are spread over a narrow interval above the superconducting energy gap 2Δ, the appropriate parameters to characterize this nonequilibrium state are the number, $\Delta_{nq}$, of excess quasiparticles and the number, $\Delta n_p$, of excess, the so-called, 2Δ phonons. The 2Δ phonons are emitted in the Cooper-pair recombination process and, since they have the energy of at least 2Δ, they are responsible for secondary breaking of Cooper pairs. For small perturbations, concentrations of $\Delta n_q$ and $\Delta n_p$ are given by the following linearized RT rate equations:

$$\frac{d\Delta n_q}{dt} = \frac{\Delta n_q}{\tau_R} + \frac{2\Delta n_p}{\tau_B} \tag{2.2a}$$

$$\frac{d\Delta n_p}{dt} = -\frac{\Delta n_p}{\tau_B} - \frac{\Delta n_p}{\tau_{es}} + \frac{\Delta n_q}{2\tau_R} \tag{2.2b}$$

where $\tau_R$ and $\tau_B$ are the quasiparticle recombination time and the time of breaking Cooper pairs by 2Δ phonons, respectively. It's interesting to note that equations (2.2) are mathematically analogous to the 2-T model (equations (2.1)). Like the 2-T model, the RT approach assumes that there is a quick, intrinsic thermalization mechanism inside both the quasiparticle and phonon subsystems decribed by the same temperature.

The knowledge of the excess number of excited quasiparticles can he helpfull to eva,uate a n inteesting parameter for explaining superconducting detectors' performances, i.e. the kinetic inductance. When photons with energy typically much larger than 2Δ are absorbed by a superconducting film maintained at $T \ll T_C$, they produce a time-dependent population $\Delta n_q(t)$ of nonequilibrium quasiparticles, leading to a temporary decrease in the superconducting fraction of electrons, $f_{SC}=(n_0 - n_q)/n_0$, where $n_q=n_q(0) + \Delta n_q(t)$ is the instant concentration of the quasiparticles, $n_q(0)$ is their equilibrium concentration and $n_0$ is the total concentration of electrons. Because the pairs are characterized by nonzero inertia, this process can be modelled as time-varying kinetic inductance [32, 33]:

$$L_{KIN}(t) = \frac{L_{KIN}(0)}{f_{SC}} \tag{2.3}$$

where $L_{KIN}(0) = \mu_0(\lambda_L)^2/d$ is the equilibrium value per unit area of the film, $\lambda_L$ is the magnetic penetration depth and $d$ is the film thickness. The $L_{KIN}$ of a superconducting film makes it possible to monitor the concentration of Cooper pairs. In a current-biased superconducting film, after the destruction of a certain number of Cooper pairs, the remaining pairs accelerate to carry the same bias current. Because of nonzero inertia of pairs, acceleration requires an electric field. This intrinsically generated electric field is seen from the exterior as a voltage pulse developing across the film. Mathematically, this voltage transient is given by:

$$V_{KIN}(t) = I \frac{dL_{KIN}(0)}{dt} \tag{2.4}$$

For the limiting case of very fast thermalization, i.e. when $\tau_T$ is small compared to both $\tau_R$ and $\tau_B$, the kinetic-inductive response was described by Semenov et al. [34] as the product of the analytical solution of equations (2.2) and a fitting factor exponentially growing in time. The latter parameter corresponds to the multiplication cascade of quasiparticles

during thermalization. This approach describes well the experimental results obtained with pulsed and modulated continues wave excitations for NbN films (Fig. 2.4).

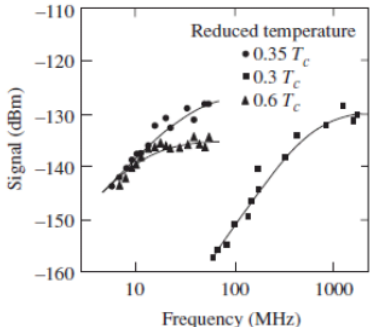


**Fig.2.4** Signal response of a NbN HEP to pulsed and modulated cw optical radiation compared to simulations by eq. (2.2) [33].

The above graph has been obtained by electro-optic technique (see further, photoresponse measurements).

## 2.3 Vortices in nonequilibrium conditions

In 1957, Alexei A. Abrikosov published a paper in which he investigated on superconductors whose magnetic field penetration length λ is larger than the coherence length ξ de facto starting the theorization of type-II superconductors. He proved how magnetic flux can penetrate the superconductor in spite of Meissner effect, creating a "mixed state" in which normal and superconducting state coexist. In such conditions the consecuting dissipation after applying a biasing current is not due to electrons motion but to vortices one. In 1965 John Bardeen and M.J. Stephen showed that vortices move into an homogeneous superconductor as particles inside a viscous medium showing a viscous resisting drag. Consequently, IV curves present a linear resistive branch (flux flow branch) similar to normal state one but scaled accordingly to applied magnetic field intensity. Because of the phenomenon known as *pinning*, in real superconductors the flux motion starts at non-zero current value. It comes out particularly inside $HT_C$ superconductors because it is strictly tied to inhomogeneities and asymmetries of lattice, but is equally present in $LT_C$ superconductors. One of the theories which deals with non-linear effects of vortices motion is the so-called *Larkin-Ovchinnikon Theory* (1975) which investigates the compression of moving vortices related to the viscosity drop within the superconductor. This phenomenon, known as flux-flow instability, presents itself as "jumps" in the IV curves from the flux-flow branch to normal state one. Another model is tied to non-linearities of flux-flow (FF) and is referred as dynamic ordering (DO): vortex in their structure and motion can be thought to be displaced as a lattice and the *vortex lattice* (VL) has got a periodic structure. The DO is a transition from a disordered moving lattice to an ordered one: for example, it comes out as a peak in the dynamic FF resistance dependence on the bias current within an superconductor's IV curve that takes an S shape. The DO is dependent on material's lattice and on pinning strength of vortex in a superconductor.

### 2.3.1 The Ginzburg-Landau theory

To describe vortices in superconductors, a phenomenological theory particularly suited is the Ginzburg-Landau Theory (in the following, GL Theory) [35] as mentioned in previous chapter. The GL Theory is based on the Landau's Theory of the second order phase transitions [36], in which the key-concept is the introduction of an order parameter which characterize the increasing of the order in the state of the system under analysis. In the case of a superconducting state, the order parameter is a complex wave-function:

$$\psi(r) = |\psi(r)| e^{i\varphi(r)}$$

which has the modulus corresponding to the local density of Cooper pairs:

$$|\psi(r)|^2 = n_S(r)$$

It follows that the $|\psi(r)|^2$ approaches to zero as the temperature T becomes close to the critical temperature $T_C$. It is possible to make an expansion of the free energy of the

superconducting state $F_S$ around $T \cong T_C$, in terms of $|\psi(r)|^2$ and its gradient in the presence of a magnetic field $h = \nabla \times A$:

$$F_S = F_N + \alpha|\psi|^2 + \frac{\beta}{2}|\psi|^4 + \frac{1}{2m^*}\left|(-i\hbar\nabla - 2eA)\psi\right|^2 + \frac{\mu_0 h^2}{2} \tag{2.5}$$

where $F_N$ is the free energy of the normal state, α and β are generally functions of T, m* the effective mass of the superconducting electrons and *e* is the electron charge. By minimizing the expression (2.5) with respect to $|\psi(r)|^2$ and to the vector potential, one obtains the GL equations [53]:

$$\alpha\psi + \beta|\psi|^2\psi + \frac{1}{2m^*}\left(\frac{\hbar}{i}\nabla - \frac{e^*}{c}A\right)^2\psi = 0 \tag{2.6a}$$

$$\frac{1}{4\pi}\left[\nabla\times(\nabla\times A)\right] - \frac{i\hbar}{2m^*c}\cdot\left[\psi\left(\frac{ie}{\hbar c}A\right)\psi^* - \psi^*\left(\nabla - \frac{ie}{\hbar c}A\right)\psi\right] = 0 \tag{2.6b}$$

From the GL equations it is possible to derive the expressions of the two characteristic lengths in a superconductor: the coherence length ξ that is the distance over which the order parameter can vary, and the penetration depth λ, in other words it is the length scale over which a magnetic field is screened by the supercurrents. For an inhomogeneous superconductor in absence of a magnetic field( $\nabla\psi \neq 0$ and A = 0) it was demonstrated that:

$$\xi^2 = \frac{\hbar}{2m^*\alpha}$$

while the expression of the latter length follows from the second GL Equation (1.4b); similarly, in the case of an homogeneous superconductor in presence of a magnetic field ( $\nabla\psi = 0$ and A≠ 0):

$$\lambda^2 = \frac{m^*c^2}{4\pi e^2|\psi_0|^2}$$

where *c* is the light of speed and $|\psi_0|$ is the order parameter in a homogeneous superconductor [37]. Superconductors' behavior in presence of a magnetic field can be classified by means of one parameter, the Ginzburg-Landau parameter defined as the ratio between the penetration depth and the coherence length κ=λ/ξ (see Fig. 2.5).

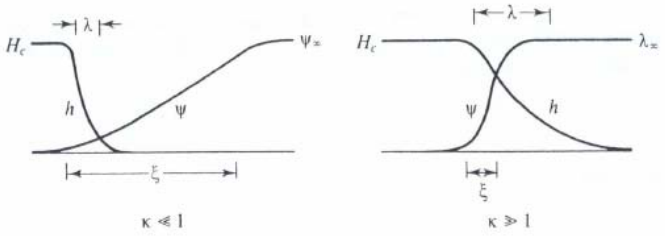


**Fig. 2.5** Schematic diagram of variation of the, magnetic field *h* and the, superconducting order parameter *ψ*, in a type-I (κ≪ 1) and in a type-II (κ ≫1) superconductor.

Ginzburg and Landau showed [35] that κ, is linked to the interface energy a between a normal and a superconducting region, so that the value $1/\sqrt{2}$ divides the superconductors in two categories:

- the superconductors with $\kappa<1/\sqrt{2}$ i.e. σ>0, are classified as Type I superconductors, which undergo to a sudden transition from Meissner state (i.e., the state of perfect diamagnetism) to the normal state as soon as the external magnetic field exceeds the (thermodynamical) critical magnetic field $H_C$ (Fig. 2.6a)
- the superconductors with $\kappa>1/\sqrt{2}$ i.e. σ<0 are classified as Type II superconductors, in which between the Meissner state and the normal state there is a state in which the magnetic flux could penetrate inside the superconductor (the so called mixed or vortex state). As a consequence, two critical magnetic fields exist: the lower critical magnetic field $H_{C1}$, which separates the Meissner state

from the mixed state, and the upper critical magnetic field $H_{C2}$, which characterizes the border between the mixed state and the normal state (Fig. 2.6b).

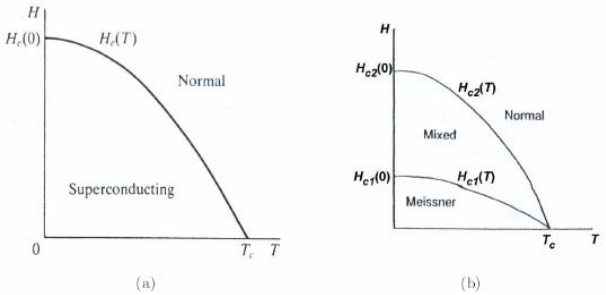


**Fig. 2.6** Ideal magnetic field versus temperature phase diagrams for a type-I (a) and a type-II (h) superconductor.

## 2.3.2 Vortices in Type-II superconductors

According to the London model (which assumes $\kappa \gg 1$), a magnetic flux can penetrate into a Type-II superconductor and this penetration occurs in the form of flux tubes which have the radius of the order of $\xi$. Within this region the order parameter is strongly suppressed, so that it is commonly considered as a normal state region. The tubes are surrounded by a region in which superconducting screening currents flow over a distance of the order of $\lambda$ (Fig. 2.7) [38]. Due to this structure, the whole region is called Abrikosov vortex [39] or simply vortex. In the following we will refer to this entities both as vortex and as flux lines.

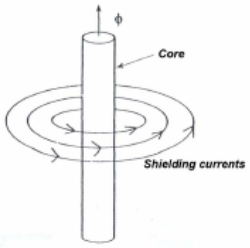


**Fig. 2.7** Abrikosov vortex.

A proper theoretical description of the vortex state requires solutions of the microscopic BCS theory: we limit to describe the picture that arises from these solutions. Close to $H_{Cl}$ quasi-particles whose energy E is less than the bulk energy gap $\Delta_0$ form bound states in the vortex core due to repeated Andreev scattering [40]. The total density of bound states in the range of energy below the gap is approximately equal to the density of states associated with a cylinder of normal metal of generic radius r (see picture of a flux line having a "normal core" [41]).

Close to $H_{C2}$ the concept of an individual vortex ceases to be meaningful: there is a significant overlap of the bound states wave functions of neighboring vortices, so that they form bands throughout the whole sample analogous to those of a gapless superconductor [41]. The vortex core structure is influenced not only by the intensity of the magnetic field, but also by temperature, the anisotropy of the energy gap and the anisotropy of the Fermi surface. In particular, Kramer and Pesch [42]showed how reducing the temperature, the vortex core size is reduced. This phenomena is connected with the thermal depopulation of the higher energy bound core states: by decreasing temperature the quasi-particles goes to occupy the lower energy bound states, the wave functions of which do not extend as far out the vortex center as the high energy ones.

The quantity of magnetic flux confined inside a single vortex comes from the "fluxoid quantization condition" [53]

$$\int_V B \cdot dS + \frac{\mu_0 m^*}{c^2} \int_0^r \frac{J \cdot dl}{|\psi|^2} = n\Phi_0 \tag{2.7}$$

where B is the magnetic field inside the material and n is the number of flux quanta $\Phi_0$ that could be inside the vortex region. For the case of an isolated vortex, the first integral could be taken over all the superconductor, while the second integral could be take from r = 0 to r $\infty$. Since J becomes negligibly small at large distances, the second integral becomes zero.

Generally n=1 but it is possible to find multi-quanta vortices [43 ]. The local magnetic field h(r) outside the normal vortex core for $\kappa \gg 1$ is [38] proportional to flux quanta $\Phi_0$, i.e.

$$h(r) = \frac{\Phi_0}{2\pi\lambda^2} K_0\left(\frac{r}{\lambda}\right) \tag{2.8}$$

where $K_0$ is the Henkel function of zero order.

## 2.3.3 Vortex interactions

For giving a brief overview on vortex-vortex interaction, first let's consider the steady-state regime particularly in presence of a constant biasing current. Between 2 vortices of the same magnetic polarity spaced at distance d, the Lorenz force per unit of length $f_{21}$ due to the first vortex acting on the second one is $f_{21} = J_2 \times B_1$. Integrating within the volume including the two vortices and considering the current constant in it, we obtain $f_{21} = J_2(d) \times \Phi_0$. For $\kappa \gg \lambda$, the previous relation becomes

$$f_{21} = \frac{\Psi_0^2}{2\mu_0\sqrt{2\pi\lambda^5 d}} \exp\left(\frac{-d}{\lambda}\right) \tag{2.9}$$

To estimate the interaction energy between vortices, we need to evaluate the overall magnetic field h generated by vortices themselves as superposition of the $h_i(|r-r_i|)$ generated field where $r_i$ is the position of the center of the i-th vortex, where contribution of the normal core is negligible.

$$E_{12} = \frac{\lambda^2}{8\pi}\left[\oint h_1 \times (\nabla \times h_2) ds_2 + \oint h_2 \times (\nabla \times h_1) ds_1\right] \tag{2.10}$$

Sobstituting Eq. (2.8) in (2.10) we obtain [38]

$$E_{12} = \frac{\Phi_0^2}{8(\pi\lambda)^2} K_0\left(\frac{|r_1 - r_2|}{\lambda}\right) \tag{2.11}$$

As a consequence, *interaction* between vortices of the same polarity is *repulsive*. Abrikosov predicted that vortices arrange themselves in a lattice (Abrikosov lattice [39] or Vortex-Lattice) that for a pure SC is square and a pair of vortices are settled with a distance $a_\square = \sqrt{\frac{\Phi_0}{B}}$. Kleiner, Roth and Autler [44]demonstrated that the real Abrikosov lattice has a hexagonal array (see Figure 2.8), and the distance between two vortices (usually referred as $a_0$) is given by: $a_\Delta = 1.075\sqrt{\frac{\Phi_0}{B}}$.

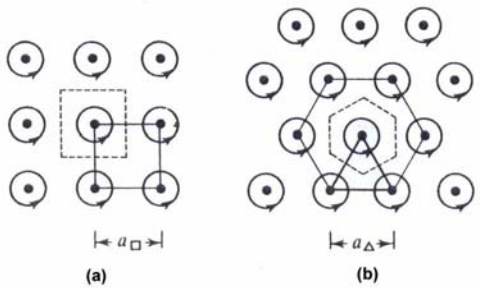


**Fig.2.8** Schematic diagram of vortex lattice: dashed lines are basic unit cells.

However, there is an exception to the repulsive nature of the vortex-vortex interaction in Type II superconductors. This exception takes place in superconductors with a GL parameter K near the threshold value $1/\sqrt{2}$ and it reveals itself as an attractive interaction [38]. This attractive interaction results in a new type of magnetic flux structure consisting of a mixture of flux-free domains and domains containing a vortex lattice.

## 2.3.4 Flux pinning, pinning force and pinning interaction

In the previous section vortex lattice has been presented as in a pure and homogeneous superconductor. When, as really happen, there is a lack of homogeneity and purity, vortex may stand steady even in presence of an external current, by density $J_{ext}$, that act on vortices with the Lorentz force $J_{ext}\times\Phi_0$. This effect is called *flux-pinning* (FP) and a vortex is fixed on a *pinning site*. There are different kind of pinning sites, but all of them are characterized by a strong suppression of the order parameter. They could be inhomogeneities in the material (for example: dislocations, vacancies, grain boundaries, etc...), also artificially realized or tied to strong anisotropy of the crystalline structure.
Pinning produces the following effects:

- the current-voltage curve of a superconductor in a magnetic field is highly nonlinear,
- the magnetization curve is irreversible and performs a hysteresis loop when the applied magnetic field is cycled,
- pinned vortices exert a force on the atomic lattice which leads to magneto- mechanical effects such as "giant magneto-restriction" or a strong "internal friction" which enables superconductors to levitate firmly above (or below) an asymmetric permanent magnet,
- the key role of the pinning is that *only with pinned vortices does a superconductor exhibit zero resistivity*, only when the Lorentz force exceeds the pinning force FP , i.e. $J_{ext}\times\Phi_0>F_P$ injected current density exceeds the critical current density $J_C$, vortices occur in depinning and start motion.

A critical state is the boundary state between two different regimes of the system. In the case of a superconductor, it is in a critical state when the Lorentz force exactly equals the pinning force. Thus, if we consider the critical current density $J_c(B)$ at a fixed induction field and the pinning force $F_P(B)$ per unit volume, the critical state may be represented by $F_P(B)=J_C(B)\cdot B$ . FP must be zero at B=0 and at $B=\mu_0 H_{C2}$ so pinning force must present a maximum. A good approach for measuring $F_P$ has been proposed by Dew-Huges [45] who presented pinning force as :

$$F_P = -\frac{\eta L \Delta W}{x} \tag{2.12}$$

where ΔW is the work done to move a unit length of flux-line (i.e. vortex) from a pinning center to the nearest position where it is unpinned, x is the effective range of the pinning interaction, L is the total length of flux-line per unit volume that is directly pinned and η is an efficiency factor determined by the extent to which its neighbours in the flux-lattice allow to relax toward a position of maximum pinning . The quantities in (2.12) are influenced by four features:

- The nature of the pinning center, as it is the difference between their superconducting properties and those of the material which determines the strength of the local interaction. In fact, there are two types of pinning center: (1) the κ pinning sites, which are characterized by a small difference between the κ, value of the material and the one of the site, and (2) the normal pinning sites, i.e. sites which are zones of a strong order parameter suppression.
- The size of the pinning centers, as it determines the total length of interacting flux-line and the geometrical nature of the interaction.
- The rigidity of the flux lattice, as it determines whether displacements of flux-lines under local pinning forces are purely elastic or the pinning force are so strong to disrupt the lattice and allow each flux-line to act individually.
- The size and spacing of the pinning micro-structure compared to λ, as only if this is greater than λ can the local equilibrium value of *B* be established.

## 2.4 Phase-slip centers

The traditional interpretation of the resistance in type-II superconductors [46], by vortices crossing the current lines, fails in structures too narrow to accommodate a single vortex. Webb and Warburton [47], then Meyer *et al.* [48], measuring the resistive transition *R*(*T*) of crystalline tin lines, were the first to observe tiny resistance steps, just below the critical temperature *T*c, instead of a continuous increase. These steps, confirmed soon after in narrow thin films [49], were supposed to arise from Josephson-like pulsations in Phase-Slip Centers (PSCs) which, in one-dimensional (1D) microbridges, are the substitutes to the vortex flow process. In the commonly used voltage-bias configuration, *I–V* (current–voltage) characteristics conceal some ambiguities, because simple hot spots (HS) also manifest themselves as voltage jumps [50, 51].

A superconducting bridge is one-dimensional if a current-carrying state may be considered homogeneous over the width of the bridge. In what may be called the standard PSC model[4], a PSC is a localized dissipation unit extending over twice the quasiparticle diffusion length $\Lambda_{qp}$ (typically 1 Ωm), where the current periodically alternates between the superfluid and the normal forms at the Josephson frequency Ω=2eV/h. If the normal resistance of the $\Lambda_{qp}$ zone is $R_u$, the voltage drop along the filament increases by a quantity $\Delta V$ of the order of $(1/2)R_u I_c$ for each new PSC created (Fig. 2.9). Above each critical current $I_c$, there is a linear increase of the voltage, with a differential resistance $dV/dI = R_u$. Let us mention also the flux-flow regime sometimes observed in thin films (Fig. 2.9) at temperatures very close to $T_c$, although not in strictly 1D systems such as whiskers [47,48].

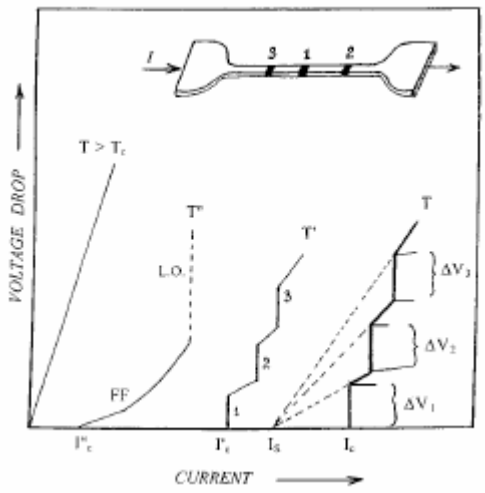


**Fig.2.9** Ideal voltage current characteristic curve of along bridge in th enormal ($T>T_c$) linear and non linear flux-flow(FF), and phase-slip regimes[52], according to temperature. The critical currents bear the same index as the corresponding T<T'<T''. Is is the time-averaged superfluid current flowing through PSCs1,2,and 3.

Dissipation causes some temperature rise at the PSC location, proportionally to the Joule power $\Omega I_c^2$, where Ω is the normal state resistivity. This heating may be neglected close to $T_c$, owing to the specific temperature dependence of the critical current; however, a transition into the normal state is not excluded at lower substrate temperatures. So, although we challenge this idea, the PSC regime is usually considered [49,53] to be confined to a small temperature range, of the order of 1 K or even less, close to $T_c$.
The changes in currents and potentials occurring inside a PSC may be compared to those experienced by an observer placed in a vortex street. At each vortex crossing (frequency Ω), the superconducting order parameter falls off to zero, then rebuilds, and the phenomenon repeats itself. Each cycle is accompanied by a phase slip between the two sides of the superconducting wave function, thereby allowing a voltage drop. If the phase slippage is quantized (by amounts of $\cong 2\pi$), there will be no overall loss of coherence of the wave function along the bridge.

It is possible to make some general considerations useful to discuss compare the resistive state of current-carrying bridges

**Delay Time**
No latency period has ever been reported at the onset of vortex flow or creep, while the delay $t_d$ appears as an unmistakable signature of the opening of a PSC.

**Stable, or Linearly Changing, Voltage Signals**
PSCs are in principle well-defined structures which, apart from heating effects, have a length $2\Lambda_{qp}$ not expected to change in time once they have been created, that is, after $t_d$. In contrast, a hot spot has a time-dependent size: a current able to sustain the normal state on a certain length is a fortiori able to sustain twice this length, and so on, propagation taking place by heat diffusion. Therefore, in constant-current bias, HS will manifest themselves as signals linearly rising with time.

**Differential Resistance**
The I-V isotherm of a PSC structure (see Fig. 8 of [49]), taken on the top of the voltage response, extrapolates to zero voltage at a value $I_s$, which is the time-averaged superconducting component of the current.

## 2.4.1 Hot Spot time creation

Let us consider (Fig. 2.10, top) a thin film of normal resistivity $\rho$ holding a current density $J$, in the situation where a hot spot has formed. The Joule power generated, $\rho J^2$ per unit volume, is shared between the heat flux to the substrate, $C\tau^{-1}(T\text{-}T_b)$ per unit area, ($C$=specific heat per unit volume ) and a longitudinal component which can be equated to $-k(\partial^2 T/\partial x^2)$ per unit cross section of the film. Here, $T(x, t)$ is the position and time-dependent temperature of the film and $k$ is the bulk coefficient of thermal conductivity of the superconductor, related to $D$, the diffusivity of heat, by $k=C\cdot D$. For simplicity, we assume all parameters to be temperature independent, and identical (except $\rho$) in the normal and superconducting part of the system. In the normal state, the heat rate equations are verified:

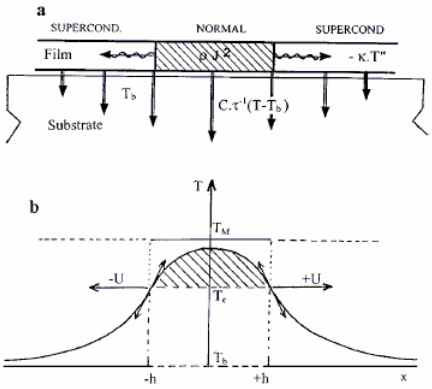


**Fig.2.10** (a) Thermal transfers into and out of a hot spot: dissipation $\rho J^2$ above $T_c$, heat conduction along the film –kT'', and escape to the substrate (double arrows), proportional to ($T$ - $T_b$). (b) Hot spot temperature profile at instant $t$.$T_b$: bath temperature; $T_M$: asymptotic temperature. $U$ is the HS wall velocity[52].

$$C\frac{\partial T}{\partial t} = kT'' - \frac{C}{\tau}(T - T_b) + \rho J^2 \tag{2.13}$$

and a similar equation (excluding the term $\rho J^2$) in the superconducting regions. At the superconducting/normal interface, the two temperatures equal $T_c$ and the first space derivatives $(\partial T/\partial x)$ must be equal. A progressive solution of this coupled set can be found, with an interface velocity $U$ given by

$$U = \frac{y^2 - 2}{\sqrt{y^2 - 1}}\sqrt{\frac{D}{\tau}} \tag{2.14}$$

Here $y$ is the ratio $I/I_1$, with $I_1$=Volume*(C(T-$T_b$)/τρ)$^{1/2}$: Equation (2.14) predicts not only the positive values of $U$ but also an interval $I_1<I<I_h$, where $U$ is defined and negative. Then, the situation is that of a receding hot spot with a central temperature $T > T_c$. A plausible temperature profile at a fixed instant is drawn in Fig. 2.10. It is constrained between the limits $T_b$ and $T_M$ such that

$$\rho J^2 = C\cdot\tau^{-1}(T_M - T_b). \tag{2.15}$$

For example, the normal zone expands or shrinks with velocity $2U$ ($U$ on each side). An illustration of the current dependence of the velocity is given in Fig. 2.11. It is interesting to compare HS velocities in two materials such as YBCO and Nb. (For the measurement procedure, see

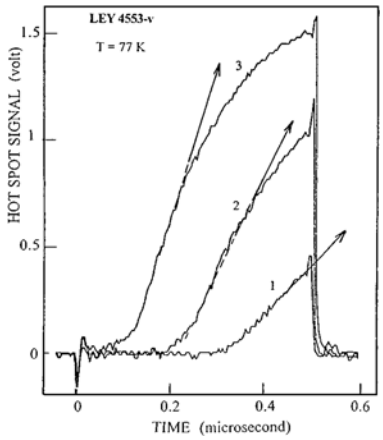


**Fig.2.11** Change of the HS velocity of growth along with amplitude of the current.YBCOsampleLEY4553-v ($d$ = 120 nm)[52]. HS velocities are, from 1 to 3: 14 m/s; 30 m/s; 38 m/s. Corresponding current densities in MA/cm2: 3.04; 3.10; 3.23; $I_c$ (77 K) = 3.02.

[**Errore. Il segnalibro non è definito.**].). The factor $(D/\tau)^{1/2}$ is equivalent to $(vl=3\tau)^{1/2}$, where $v$ is the velocity of the heat carriers and $l$ their mean free path. Let us assume that heat is transported by the electrons in Nb and by the phonons in YBCO, with approximately the same $l$ of the order of 2–3 nm. Cooling times in our films are also of the same order of magnitude, around 10 ns. So, the main difference between the two materials is in the velocity of the heat carriers, $\cong 2\cdot 10^{-6}$ m/s for electrons in niobium and $\cong 3$ km/s for phonons in YBCO. This difference accounts for a factor of about 20 in the observed HS experimental velocities between the two materials.

## 2.5 The kinetic inductance

### 2.5.1 The kinetic inductance of a metallic conductor

The kinetic inductance of a metallic conductor [54] is generally referred to the inertial mass of current carriers. It is well distinguished from geometrical inductance of the conductor and is deeply tight to the material whom the conductor is made by. If we consider the energy associated with the electric current carried by particles of mass $m$ and number density $n$:

$$E = \int_{all\_space} \frac{1}{2}\mu H^2 dr + \int_{conductor} \frac{1}{2} m v^2 n dr \tag{2.16}$$

for an homogeneous conductor whose material properties ($n$,$m$,$\mu$) are independent of $H$ and $J$:

$$E = \frac{1}{2} L_M I^2 + \frac{1}{2}\left[\frac{m}{ne^2}\cdot\frac{l}{\sigma}\right]\cdot I^2 \tag{2.17}$$

$L_M$ is the magnetic (geometrical) inductance. The kinetic inductance is the term in parenthesys

$$L_K = \frac{m}{ne^2}\cdot\frac{l}{\sigma} \tag{2.18}$$

According to the London theory, the energy density of the superconducting surface currents is :

$$\varepsilon_{London} = \frac{1}{2}\cdot\frac{m}{ne^2}J^2 + \frac{1}{2}\mu H^2 \tag{2.19}$$

The resistance of a wire can be written as:

$$R = \left(\frac{m}{ne^2}\cdot\frac{l}{\sigma}\right)\cdot\frac{1}{\tau} \tag{2.20}$$

where $\tau$ is the electron collision time. The kinetic reactance of the same wire is:

$$\omega L_K = \omega\left(\frac{m}{ne^2}\cdot\frac{l}{\sigma}\right) \tag{2.21}$$

Only when $\omega > \frac{1}{\tau}$ the kinetic reactance will dominate the resistance ; this will occur at a frequency of the $10^{13}$ Hz order at room temperature. However, in a superconductor $\tau \to \infty$ and $\omega L_k$ dominates R at any frequency.

An easy way to measure $L_K$ is to realize an oscillator (e.g. tunnel diode oscillator or others in which the resonance is governed by R,C and L parameters), not in the target of this work, but it is important to observe that the relation between the inductance change and the frequency change (for small fluctuations) is obtainable by differentiating the resonance condition

$$\omega^2 = \frac{1}{LC}\left[1 + \frac{R^2 C}{L}\right] \tag{2.22a}$$

thus obtaining

$$\frac{\Delta\omega}{\omega_0} = -\frac{\Delta L}{2L_0}\left[1 - \frac{2}{Q^2}\right] - \frac{\Delta R}{R}\cdot\frac{1}{Q^2} \tag{2.22b}$$

with $\omega_0^2=1/LC$. For high values of Q (e.g. Q≥100) the frequency changes are proportional to inductance changes and resistive effects can be neglected (except very near the $T_C$).

## 2.5.2 The calculation of the kinetic inductance

Let's consider the cases in which the conductor is an homogeneous superconducting cylinder of uniform rectangular cross section. Equation (2.18) assumes a uniform current density and applies only when the lateral dimensions are much smaller than the penetration depth. If so, the kinetic inductance is a function of the penetration depth λ as

$$L_K = \mu_0 \lambda^2 \frac{l}{\sigma} \tag{2.23}$$

where $\lambda^2=m^*/\mu_0 n_s e^{*2}$ and $n_s$, $m^*$ and $e^*$ are the carrier concentration, the effective mass and the effective charge of the current carriers, $l$ and $\sigma$ are the length and the cross-section area of the superconductor. In the general case, when the current density varies across the section area, $L_K$ is

$$L_K = \left(\frac{m^*}{ne^{*2}}\right)\cdot l \cdot \frac{\int_\sigma J^2 d\sigma}{I^2} \tag{2.24}$$

where the last factor is the reciprocal of the effective cross-section area with $I$ the total current. In the London theory , the supercurrent density is the solution of the equation

$$\nabla\times\nabla\times J_S = \frac{J_S}{\lambda^2} \tag{2.25a}$$

and the magnetic field inside the superconductor is solution of

$$\nabla\times\nabla\times H = \frac{-H}{\lambda^2} \tag{2.25b}$$

For a circular conductor in which the radius a≫λ the current is carried through a thin surface layer circa λ in thickness and the total energy associated with the current is

$$E = l\cdot\int_{r=a}^{r=b}\frac{1}{2}\mu_0 H^2\cdot 2\pi r dr + l\cdot\int_{r=0}^{r=a}\frac{1}{2}\mu_0 H^2\cdot 2\pi r dr + l\cdot\int_{r=0}^{r=a}\frac{1}{2}\mu_0\lambda^2 J^2\cdot 2\pi r dr \tag{2.26}$$

Since a≫λH and J lie essentially in the layer on the wire surface and in the London theory they can be well approximated by

$$H = H_a \exp(-x/\lambda) \tag{2.27a}$$

$$J = (H_a/\lambda)\exp(-x/\lambda) \quad \text{for } r\le a \tag{2.27b}$$

where x=a-r and x≪a. Outside the wire, the magnetic field is

$$H = H_a(a/r) \qquad \text{with } r\ge a \tag{2.27c}$$

while for Ampere's law the field at the surface is

$$H = I/2\pi a$$

When Eq.(2.26) is evaluated using Eqs. (2.27), we obtain

$$E = \frac{1}{2}\left[\left(\mu_0 l / 2\pi\right)\ln\left(b/a\right) + \left(\mu_0 l\lambda / 4\pi a\right) + \left(\mu_0 l\lambda / 4\pi a\right)\right] \cdot I^2 \qquad (2.28)$$

The first term is the energy stored in the external magnetic field and is not temperature dependent. We are interested in temperature dependant behaviour and will disregard it. The second and third terms are inductances from magnetic field in penetration depth $L_M$ and the kinetic inductance $L_K$ , so the total temperature dependent inductance is

$$L_T = L_M + L_K = \mu_0 l\lambda / 2\pi a \qquad (2.29)$$

that shows why for bulk superconductors, to which Eqs. (2.27a) and (2.27b) apply, it is verified $L_M$=$L_K$ ; when at least one lateral dimension is less then λ, the kinetic inductance dominates the internal magnetic inductance.

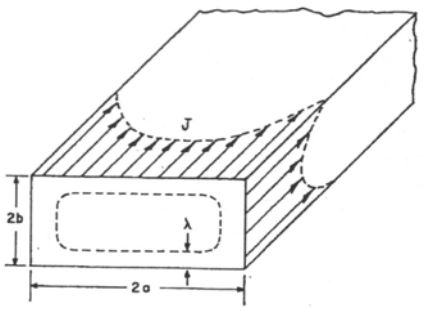


**Fig.2.12** Current distribution in a rectangular cross section cylinder.

Fig. 2.12 shows the nonuniform distribution in a thin-film strip with a≫b and b>λ. However, it should be noted that in the specimen actually measured the width to thickness ratio a/b is 2500 circa and is thus orders of magnitude wider than that shown in Fig. 2.12. The current and field distribution corresponding to the London equation for a current carrying rectangular cylinder is very hard to solve exactly. Cooper [55] discussed the problem and Marcus [56] gave an approximate solution together with some numerical results. In the present study an approximate solution is shown, given by Edwards and Newhouse[57] which yields a simple and apparently rather accurate value for the self-inductance of at least the thicker films. In this solution it is assumed that the magnetic field is everywhere parallel to the surface of the film and it is solved for H outside the cylinder by a conformal transformation of a circular cylinder into an ellipse. The width to thickness ratio is large and the rectangular cross section is approximated by the ellipse as the eccentricity tends to infinite and the ellipse reduces to a line. The result is that the field distribution on the film surface is in mks units

$$H_s = \frac{I}{2\pi\left(a^2 - x^2\right)^{1/2}} \qquad (2.30)$$

where the lateral dimension as measured from the center is x and a is the half-width of the film. Equation (2.30) is for the limit b→0 and b≫λ. In this limit HS becomes infinite at x=±a and there is a logarithmic singularity in the calculated inductance. To remove this mathematical singularity, it needs to introduce a finite thickness of the film 2b. To do this, equation (2.30) must be modified:

$$H_s = \frac{I}{2\pi\left(\left(a+\delta\right)^2 - x^2\right)^{1/2}} = I \cdot f(x) \qquad (2.31)$$

where δ is a small distance to be determined so that Ampere's law is still satisfied around the film boundary. The field at x=a is HS(a) and is now finite. For films where b<λ, HS(a) is nearly constant along the distance 2b at the ends of the film. In this case Ampere's law requires

$$\delta = b/2 \quad \text{with} \quad b < \lambda \,. \qquad (2.32a)$$

When b>λ an exponential decrease of field may be expected along the end which leads in a similar manner to the cutoff

$$\delta = \lambda/2 \quad \text{with} \quad b > \lambda \,. \qquad (2.32b)$$

The value of δ is certainly not exact but because we are interested in the energy, an integral quantity, and because the singularity is logarithmic the exact value of the cutoff does not greatly affect the results and the results given above are adequate.

Equation (2.31) is essentially one-dimensional and gives us a distribution of HS in the x direction. For films thicker than 2λ there is also a rapid variation of H and J in the y direction (perpendicular to the plane of the film). Near x=0 for a≫b, the x variation is slow and we approach the solutions for the one-dimensional case,

$$H(y)=H_S\left[\sinh\left(\frac{y}{\lambda}\right)/\sinh\left(\frac{b}{\lambda}\right)\right]=H_S\cdot g_1(y) \tag{2.33a}$$

$$J(y)=H_S\left[\cosh\left(\frac{y}{\lambda}\right)/\lambda\sinh\left(\frac{b}{\lambda}\right)\right]=H_S\cdot g_2(y) \tag{2.33b}$$

Because of the large value of the ratio a/b (typically 1000) we have assumed that the two-dimensional solutions can be written in product form,

$$H=I[f(x)\cdot g_1(y)] \tag{2.34a}$$

$$J=I[f(x)\cdot g_2(y)] \tag{2.34b}$$

The x dependence of the field and current is assumed to be identical in keeping with the original assumption that H is almost everywhere parallel to the film surface, which is plausible for b≫λ. The product form of the solution seems justified by the following consideration. It will evidently breakdown when dJ/dx=dJ/dy, but Eqs. (2.31) and (2.32b) imply that dJ/dx only becomes equal to dJ/dy within a distance λ of the edge. For a distance greater than 10λ from the edge, dJ/dx< (1/10)dJ/dy and the product solution seems justified. The contribution to the energy from an inaccuracy in this small region should be very small. An additional fact supporting the above picture is that the values of the gradients near the film edge obtained by the numerical calculations of Marcus [58] agree reasonably well with those estimated from Eq. (2.31). The energy of the internal magnetic field and the kinetic energy of the carriers

$$E=\frac{1}{2}\mu_0 l\int_\sigma\left[H^2+\lambda^2J^2\right]dxdy$$

which becomes, accordingly to Eqs. (2.34a) and (2.34b)

$$E=\left(\frac{I^2}{2}\right)\mu_0 l\int_\sigma f^2(x)\left[g_1^2(y)+\lambda^2 g_2^2(y)\right]dxdy \tag{2.35}$$

From Eqs. (2.31),(2.33a) and (2.34a), the inductance corresponding to previous energy is

$$L_T=L_M+L_K=4\mu_0 l\int_0^a\left\{\left[(a+\delta)^2-x^2\right]^{-1}\cdot 1/4\pi^2\right\}dx\cdot \tag{2.36}$$

$$\cdot\int_0^b\left\{\left[\sinh(y/\lambda)/\sinh(b/\lambda)\right]+\left[\cosh(y/\lambda)/\sinh(b/\lambda)\right]\right\}dy$$

that is

$$L_T=(\mu_0 l\lambda/4a)\left[\frac{2}{\pi^2}\ln\left(\frac{4a}{b}\right)\right]\cdot\left[\frac{\sinh\left(\frac{2b}{\lambda}\right)}{\cosh\left(\frac{2b}{\lambda}\right)}-1\right] \tag{2.37}$$

In Eq. (2.37) the first factor can be interpreted as the inductance if the surface current distribution were uniform across the width of a film in which b≫λ. The second factor corrects for the variation of current density across the width of the film The last factor corrects for film thickness when b is of the same order of magnitude as λ. Thus when b≫λ

$$L_T=(\mu_0 l\lambda/4a)\left[\frac{2}{\pi^2}\ln\left(\frac{4a}{b}\right)\right] \tag{2.38a}$$

and when b≪λ Eqs.(2.37) gives

$$L_T=(\mu_0 l\lambda^2/4ab)\left[\frac{2}{\pi^2}\ln\left(\frac{4a}{b}\right)\right] \tag{2.38b}$$

It should be noted that the last factor in (2.38b) is not rigorous because the *x* dependence was derived on the assumption that the magnetic field perpendicular to the film is zero. Actually it is obvious that as b tends to 0 the current approaches a uniform distribution and

$$L_T = \left(\mu_0 l \lambda^2 / 4ab\right) \tag{2.38c}$$

Although (2.38c) gives the inductance from the internal field and the current density, one would expect that at large enough values of current and width, quantized flux lines from the self-field of the current might cause additional inductance and/or resistance. Furthermore it should be remembered that the x distribution was derived for b>λ and only with this assumption is it reasonable to expect that the inductance associated with the external magnetic field will be independent of temperature. Thus the inductance calculation is less rigorous for the thin films than for the thick ones and needs experimental confirmation. However, Eq. (2.38c) certainly provides a lower limit to $L_T$.

For a circular wire or thick film, the temperature dependent part of the inductance is proportional to the penetration depth which is assumed to follow the BCS [59] temperature dependence $z= E[\lambda(t)/\lambda(0)]_{BCS}$. The function z(t) is equal to unity at t=0 and increases rapidly as T approaches $T_C$. This behaviour is similar to that of the function $y(t) = (1-t^4)^{-1/2}$ predicted by the Gorter-Casimir model . Most investigators plot their data against y(t). For temperatures near $T_C$, the temperature dependences of y(t) and z(t) are nearly alike. At lower temperatures, however, z(t) changes more rapidly than y(t). The inductance as a function of z is

$$L = L_0 + L_T(0)\cdot z \text{ and } dL/dz = L_T(0)$$

where $L_T(0)$ is the value of the temperature-dependent inductance at t=0. For a small fractional change in frequency we have from Eq. (2.38b)

$$\frac{df}{dz} = \frac{df}{dL}\cdot\frac{dL}{dz} = -\frac{f_0}{2L_0}\cdot L_T(0) \tag{2.39}$$

where $f_0$ is the frequency measured in a test oscillatory circuit in whom the inductance constitutes part of oscillating LC dipole[54].

For a thick rectangular film (b≫λ) Eq.(2.29) , (2.39) and (2.38a)

$$\lambda(0) = -\frac{df}{dz}\cdot\frac{2L_0}{f_0}\cdot\frac{4a}{\mu_0 l}\cdot\left[\frac{\pi^2}{2\ln(4a/b)}\right] \tag{2.40}$$

For a thin film (b<λ)

$$L = L_0 + L_T(0)\cdot z^2 \text{ and } dL/d(z^2) = L_T(0) \tag{2.41}$$

and Eq. (2.38b) gives λ(0) in terms of the measured value of df/d ($z^2$).

$$\lambda^2(0) = -\frac{df}{d(z^2)}\cdot\frac{2L_0}{f_0}\cdot\frac{4ab}{\mu_0 l}\cdot\left[\frac{\pi^2}{2\ln(4a/b)}\right] \tag{2.42}$$

When the film is very thin λ(0) must approach the value for a uniform current distribution

$$\lambda(0) = -\frac{df}{d(z^2)}\cdot\frac{2L_0}{f_0}\cdot\frac{4ab}{\mu_0 l} \tag{2.43}$$

When the thickness is dose to 2λ the asymptotic formulas are not accurate and we must use the full expression for $L_T$

$$L_T = \left(\mu_0 l\lambda/4a\right)\left[\frac{2}{\pi^2}\ln\left(\frac{4a}{b}\right)\right]\cdot\left\{\left[\frac{\sinh\left(\frac{2b}{\lambda}\right)}{\cosh\left(\frac{2b}{\lambda}\right)-1}\right]-1\right\} \tag{2.44}$$

Since the temperature dependence is contained not only λ but also in the last factor, the plot of frequency versus z will not be a straight line and λ(0) can only be obtained as the value which gives the best fit to the theoretical temperature dependence.

All the above considerations will be further used to esteem kinetic inductance on manufactured samples.

Under dc bias , a superconductor will ideally exhibit zero resistance. If an alternating bias is supplied, a finite voltage will appear across the superconductor due to the inertia of the superconducting carriers. The kinetic inductance, which gives rise to this impedance in the superconductor, for a superconducting strip of length l, width w, and thickness d can be expressed as [ 60]:

$$L_{KIN} = \frac{m}{n_{SC}e^2}\left[\frac{l}{wd}\right] = \mu_0\lambda_L^2\left[\frac{l}{wd}\right] = \frac{1}{\varepsilon_0\omega_P^2}\left[\frac{1}{f_{SC}}\right]\left[\frac{l}{wd}\right]$$

where m is the effective mass of the superconducting carriers, $n_{SC}$ is the density of superconducting carriers in a two fluid model, $\mu_0$ is the permeability of free space, $\varepsilon_0$ is the permittivity of free space, $\lambda_L$ is the temperature –dependent London penetration depth, $\omega_P$ is the plasma frequency and $f_{SC}$ is the superfluid fraction equal to $n_{SC}/n$ where n is the total density of carriers. If a laser pulse hits a superconductor will break Cooper pairs and reduces the superfluid fraction from its initial value, thereby increasing the kinetic inductance.

The superfluid current density is given by:

$J_{SC}=n_{SC}ev_{SC}$

Where $v_{SC}$ is the velocity of the superfluid carriers. If a constant current bias is applied to the bridge, then the velocity of the superfluid carriers will have to increase in order to maintain a constant current density while superfluid carriers velocity decreases. The resulting acceleration of the superfluid carriers will produce a voltage across the bridge. Indeed if we differentiate the previous eq.:

$$\frac{\partial J_{SC}}{\partial t} = n_{SC}e\frac{\partial v_{SC}}{\partial t} + ev_{SC}\frac{\partial n_{SC}}{\partial t}$$

From the condition of constant bias current I, the eq. becomes:

$$0 = \frac{n_{SC}e^2}{m}E + J_{SC}\frac{1}{n_{SC}}\frac{\partial n_{SC}}{\partial t}$$

where E is the electric field generated across the bridge by the acceleration of the carriers. Substituting the voltage V across the bridge V=El and $J_{SC}$=I/wd :

$$V = -I\frac{ml}{e^2wd}\frac{1}{n_{SC}^2}\frac{\partial n_{SC}}{\partial t} = I\frac{d}{dt}\left(\frac{ml}{n_{SC}e^2wd}\right) = I\frac{d}{dt}L_{KIN}$$

Approximately:

$$V_{KIN} \cong I\frac{\Delta L_{KIN}}{\Delta t}$$

If $f_{SC0}$ and $f_{SC}$ are the initial and final superfluid fractions at time t and t+Δt, then:

$$\Delta L_{KIN} = \frac{1}{\varepsilon_0\omega_P^2}\left(\frac{l}{wd}\right)\left(\frac{1}{f_{SC}} - \frac{1}{f_{SC0}}\right) \qquad (2.45)$$

This equation predicts a positive voltage while the superfluid fraction is decreasing followed by a negative voltage as the superfluid density recovers to its initial value.

## 2.6 The meander shaped detector

### 2.6.1 Meander structures inductance calculation

Considering that our samples are patterned structures as stripes (bridges) or generally more complicated meander structures with serial/parallel stripes, let's consider the more general case of a simple meander structure of whom we want to calculate inductance taking into account mainly its geometrical characteristics.

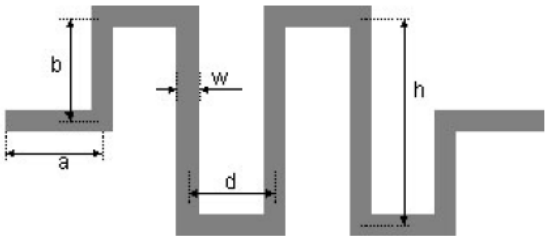


**Fig. 2.13** Meander structure and its characteristic dimensions

The starting point for the derivation of proposed formula is *Greenhouse* theory [61]. *Greenhouse* decomposed inductor into its constituent segments. Basically, meander inductor is divided into straight conductive segments. Then the total inductance of the meander inductor is a sum of self-inductances of all segments and the negative and positive mutual inductances between all combinations of straight segments. In addition to *Greenhouse's,* the great contribution to the inductance calculation is given by *Grover* [62]. He has considered the concept of partial inductance, i.e. contribution of individual segments to the overall inductance, and he also has introduced the ideas of the geometric mean distance GMD and arithmetic mean distance AMD. When studying of mutual inductance as filament we take the middle lines of the observed meander as in Fig. 1. The filaments are the straight segments of the meander inductor having negligible cross section in relation to the length.

Expression for self-inductance of the conductive segment, as in Fig. 2, as can be found in literature [5] ,is given by the following equation

$$L = 0.002 \cdot l \cdot [\ln(2 \cdot l / GMD) - 1.25 + AMD/l + (\mu / 4) \cdot T] \quad (28)$$

with the following: *L* is inductance in micro henries, *l* is length of conductive segment in centimeters, GMD and AMD represent geometrical and arithmetical mean distance of the conductor's cross-section, μ is conductor's permeability, and *T* is frequency dependant correction factor.

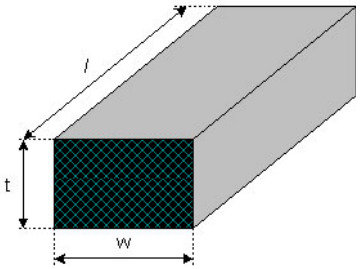


**Fig.2** Cross section of conductive segment

For inductors with rectangular cross-section, whose width is w and thickness t, GMD=0.2232(w+t); for a single conductor, the AMD is the average of all possible distances within the cross-section, has been calculated [63] and a good approximation (to 2%) is

$$AMD \cong \frac{\sqrt{w^2 + t^2 + 0.46tw}}{3}$$

For w≫t, AMD converges to w/3 and for w≪t, it converges to t/3. An useful approximation implies AMD≅(w+t)/3, so the expression for self-inductance is

$$L = 0.002 \cdot l \{\ln[2 \cdot l / 0.2232(w + t)] - 1.25 + [(w + t) / 3l] + (\mu / 4)T\} \quad (29)$$

where w and t are dimensions of the cross-section, as it is shown in Fig. 2. If we suppose that magnetic permeability μ=1 and neglect T (i.e. T=1), Eq. (29) becomes

$$L = 0.002 \cdot l \{\ln[2 \cdot l / (w + t)] + 0.50049 + [(w + t) / 3l]\} \quad (30)$$

that is the basic expression of single straight element. A further semi-experimental formula was obtained [64]

$$L = 0.002 \cdot l \left[ \ln\left( \frac{2 \cdot l}{w + t} \right) + 0.5 + \frac{w + t}{3l} + 0.028 \frac{\min(w, t, \delta)}{\min(w, t)} \right] \quad (31)$$

where $\delta = \sqrt{\rho / \pi f \mu}$ is the skin depth that takes into account the magnetic permeability. It is important also to notice that relation (30) is not strictly valid for wires having cross section dimensions grater than twice their length. Let's consider now the structure in Fig.(3):

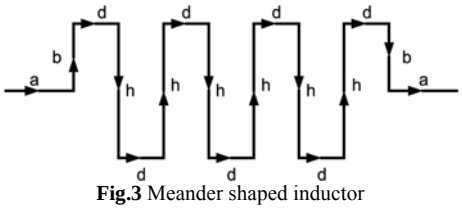


**Fig.3** Meander shaped inductor

the total self-inductance $L_{selftot}$ is calculated as a sum of self-inductances of all individual line segments, which form meander inductor,

$$L_{selftot} = 2 \cdot La + 2 \cdot Lb + N \cdot Lh + (N+1) \cdot Ld \tag{31}$$

This is a generalized equation where La,b,h,d are self-inductances of segments where the length is l = a, b, h, d (respectively) and are calculated by means of the expression for self-inductance (30). In the equation (31), N represents a number of segments of the greatest length h (for the example given in Fig. 3, N = 6 ).

In order to get the final expression for the total mutual inductance, let's consider the two cases of inductors, with even and odd number of the longest segments (length h). In Figure 4, there are some characteristic situations of the position of two segments that can appear in meander inductors and the formulae are given for calculation of their mutual inductance over the special case of two parallel conductors of the equal length at the corresponding mutual distance. The equation (32) [15] calculates mutual inductance (referred as $M_c$) of the segments with equal length l, at distance r and are place opposite one to another :

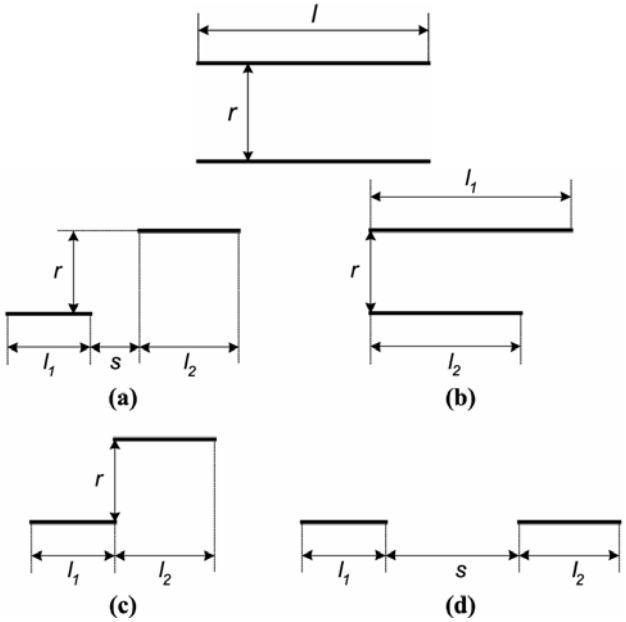


**Fig.4** Typical segment combinations in a meander structure

The mutual inductance for other segment positions can be expressed by linear combinations of the expression for calculation of mutual inductance of segments with equal length (first case inside the Fig. (4)), at distance r and which are positioned one opposite the other, using Eq. (32).

$$M_C(l,r) = \pm \frac{\mu_0}{2\pi} l \left[ \ln\left( \frac{l}{r} + \sqrt{1+\left(\frac{l}{r}\right)^2} \right) - \sqrt{1+\left(\frac{r}{l}\right)^2} + \frac{r}{l} \right] \tag{32}$$

Equation for the segment combinations as shown in Figure 4(a), for unequal parallel filaments, is:

$$M_{a1}(l_1, l_2, r, s) = 0.5\left[M_c(l_1 + l_2 + s, r) + M_c(s, r) - M_c(l_1 + s, r) - M_c(l_2 + s, r)\right] \quad (32a)$$

For the situation in Figure 4(b), where the filaments have their ends in the common perpendicular, the valid equation is:

$$M_{a2}(l_1, l_2, r) = 0.5\left[M_c(l_1, r) + M_c(l_2, r) - M_c(l_1 - l_2, r)\right] \quad (32b)$$

For the situation in Figure 4(c), appearing only in case when N-odd for the couple of filaments with length b, the following equation is used:

$$M_{a3}(l_1, l_2, r) = 0.5\left[M_c(l_1 + l_2, r) - M_c(l_1, r) - M_c(l_2, r)\right] \quad (32c)$$

For the position as in Figure 4(d) when the two segments are in the same axis (segments pairs a-a and d-d) at the corresponding distance between each other the expression designed with $M_b$ is:

$$M_b(l_1, l_2, s) = \frac{\mu_0}{4\pi}\left[(l_1 + l_2 + s)\ln(l_1 + l_2 + s) - (l_1 + s)\ln(l_1 + s) + \right.$$
$$\left. - (l_2 + s)\ln(l_2 + s) + s\ln(s)\right] \quad (32d)$$

The following table summarize and clearly enumerates all possible cases :

$$L = 0.002 \cdot l \cdot \{\ln[2l/(w+t)] + 0.50049 + [(w+t)/3l]\}$$

$$L_{selftot} = 2 \cdot L_a + 2 \cdot L_b + N \cdot L_h + (N+1) \cdot L_d$$

$$M_1 = \sum_{i=1}^{\frac{N}{2}} (2N + 4 - 4i) \cdot M_{a1}(d,d,h,(2i-2)d), \text{ for N even}$$

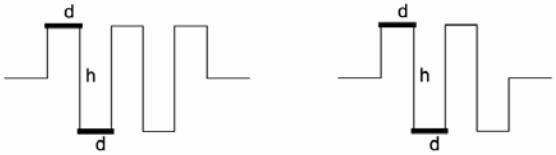


$$M_1 = \sum_{i=1}^{\frac{N+1}{2}} (2N + 4 - 4i) \cdot M_{a1}(d,d,h,(2i-2)d), \text{ for N odd}$$

$$M_2 = \sum_{i=1}^{\frac{N}{2}} (2N + 2 - 4i) \cdot M_b(d,d,(2i-1)d), \text{ for N even}$$

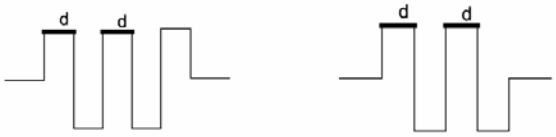


$$M_2 = \sum_{i=1}^{\frac{N-1}{2}} (2N + 2 - 4i) \cdot M_b(d,d,(2i-1)d), \text{ for N odd}$$

$$M_3 = 2 \cdot M_b(a,a,(N+1)d)$$


$$M_4 = \sum_{i=0}^{N} 4 \cdot M_{a1}(a,d,b,id)$$

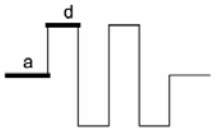


$$M_5 = \sum_{i=1}^{N-1} (-1)^i \cdot 2 \cdot (N-i) \cdot M_c(h,id)$$

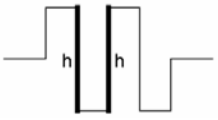


$$M_6 = -2 \cdot M_c(b,(N+1)d), \text{ for N even}$$


$$M_6 = +2 \cdot M_{a3}(b,b,(N+1)d), \text{ for N odd}$$

$$M_7 = \sum_{i=1}^{N} (-1)^i \cdot 4 \cdot M_{a2}(b,h,id)$$

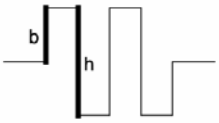


$$M_{tot} = M_1 + M_2 + M_3 + M_4 + M_5 + M_6 + M_7$$

$$L_{tot} = L_{selftot} + M_{tot}$$

**Table 1 :** Calculation of inductance for N-even and N-odd segment combinations meander

[21] N.E.Booth, Quasiparticle trapping and the quasiparticle multiplier, Appl.Phys.Lett.,vol.50,pag.293,1987

[22] Kaganov,Lifshitz,Tanatarov, Sov.Phys.JETP,vol.4,pag.173,1957
[23] Schklovski,Sov.Phys. Solid State,vol.17,pag.3076,1975
[24] N. Perrin, C. Vanneste; "Response of superconducting films to a periodic optical irradiation", *Phys. Rev. B*, vol. 28, no./pp. 5150, 1983.
[25] A. D. Semenov, R. S. Nebosis, Yu P. Gousev, M. A. Heusinger, K. F. Renk; "Analysis of the nonequilibrium photoresponse of superconducting films to pulsed radiation by use of a two-temperature model"; Phys. Rev. B, vol. 52, no./pp. 581, 1995.
[26] M. Lindgren, M. A. Zorin, V. Trifonov, M. Danerud, D. Winkler, B. S. Karasik, G. N. Gol'tsman, E. M. Gershenzon; "Optical mixing in a patterned YBa2Cu3O7−d thin film"; *Appl. Phys. Lett.*, vol. 65, no./pp. 3398, 1994.
[27] E. M. Gershenzon, M. E. Gershenzon, G. N. Gol'tsman, A. D. Semenov, A. V. Sergeev; *Sov. Phys.–JETP*, vol. 59, no./pp. 442, 1984.
[28] E. M. Gershenzon, M. E. Gershenzon, G. N. Gol'tsman, A. M. Lyul'kin, A. D. Semenov, A. V. Sergeev; *Sov Phys.–Tech. Phys.*, vol. 34, no./pp. 195, 1989.
[29] B. S. Karasika, A. I. Elantiev; "Noise temperature limit of a superconducting hot electron bolometer mixer"; *Appl. Phys. Lett.*, vol. 68, no./pp. 853, 1996.
[30] D. E. Prober; "Superconducting terahertz mixer using a transition-edge microbolometer"; *Appl. Phys. Lett.*, vol. 62, no./pp. 2119, 1993.
[31] A. Rothwarf, B. N. Taylor; "Measurement of Recombination Lifetimes in Superconductors"; *Phys. Rev. Lett.*, vol. 19, no./pp. 27, 1967.
[32] E. N. Grossman, D. G. McDonald, J. E, Sauvageau; "Far-infrared ineticinductance detectors"; *IEEE Trans. Magn.*, vol. 27, no./pp. 2677, 1991.
[33] N. Bluzer; "Analysis of quantum superconducting kinetic inductance photodetectors"; *J. Appl. Phys.*, vol. 78, no./pp. 7340, 1995.
[34] A. D. Semenov, M. A. Heusinger, K. F. Renk, E. Menschikov, A. V. Sergeev, A. I. Elant'ev, I. G. Goghidze, G. N. Gol'tsman; "Influence of phonon trapping on the performance of NbN kinetic inductance detectors"; *IEEE Trans. Appl. Supercond.*,
vol. 7, no./pp. 3083, 1997.
[35] V.L.Ginzburg and L.D.Landau,Zh.Eksp.Theor.Fiz.20,1064 (1950),pag.1-3
[36] L.D.Landau, Zh.Eksp.Theor.Fiz.7,371 (1937),pag.1
[37] C.P.Poole,H.A.Farach and R.J.Creswick,Superconductivity, Academic Press,San Diego,USA,1995
[38] R.P.Huebener,magnetic flux structures in superconductors,Springer-Verlag,Heidelberg,Germany,2000
[39] A.A.Abrikosov,Sov.Phys. JETP 5,1174 (1957)
[40] D.Rainer,J.A.Sauls,D,Waxman,Phys.Rev.B 54,10094 (1996)
[41] A.L.Fetter,P.C.Hoenenberg, Superconductivity, R.D. Parks editor, Marcell Dekker, New York (1969)
[42] W.Pesh,L.Kramer, J.Low.Temp.Phys.15,167,1974
[43] I.Buzdin,phys.Rev.B,47,11416,1993
[44] W.H.Kleiner,L.M.Roth, S.H.Autler,Phys.Rev.133,A1226 (1964)
[45] D.Dew-Huges,Ph.Mag.30,293 (1974)
[46] R. Tidecks, Non-Equilibrium Phenomena in One-Dimensional Superconductors (Springer-Verlag, Berlin, 1990).
[47] W.W.Webb and R. J.Warburton, *Phys. Rev. Lett.* 20**,** 461 (1968).
[48] J. Meyer and G. von Minnigerode, *Phys. Lett.* 38 A**,** 529 (1972); J. D. Meyer, *Appl. Phys.* 2, 303 (1973).
[49] W. J. Skocpol, M. R. Beasley, and M. Tinkham, *J. Low Temp.Phys.* 84**,** 289 (1974).
[50] W. J. Skocpol, M. R. Beasley, and M. Tinkham, *J. Appl. Phys.*45**,** 4045 (1974).
[51] T. M. Klapwijk, M. Sepers, and J. E. Mooij, *J. Low Temp. Phys.*27, 801 (1977).
[52] J.P.Maneval et alter, JOS:incorporating Novel Magnetism, Vol.14,n.2,2001
[53] M. Tinkham, *Introduction to Superconductivity*, 2nd edn. (McGraw-Hill, 1996).
[54] R.Meservey and P.M.Tedrow , Journal of Applied Physics, Vol.40,Num.5,April 1969
[55] L.Cooper, Proceedings of the seventh International Conference on low temperature Physics ,Univ.of Toronto Press,1961) pag.416
[56] Ref. 10, pag.418
[57] V.L.Newhouse , Applied superconductivity (John Wiley & Sons,Inc.,New York,1967), pag.267
[58] P.Marcus,Ref.7,pag.418
[59] J.Bardeen and J.R.Schrieffer, Progress in low temperature physics (Nort-Holland Publ. Co.,Amsterdam,1961), Vol. III
[60] F.Hegman,J.Preston, Origin of the fast photoresponse of epitaxial YBCO thin films, PRB vol.48,N.21,1993
[61] H.M.Greenhouse,Design of planar rectangular microelectronic inductors, IEEE Trans. Parts Hybrids Packaging,Vol.PHP-10,1974,pag.101-109
[62] F.W.Grover, Inductance calculations,working formulas and tables, Princeton, D.Van Nostrand company inc., 1946, Dover Publications, New York,1954
[63] S.Mohan et alter,1999, Simple accurate expressions for planar spiral inductances, IEEE Journal of solid-state circuits,Vol.34, N.10,pp.1419-1424
[64] Z.Zhu et alter, 2001, Closet form formulae for frequency-dependent 3-D interconnect inductance, Microelectronic Engineering, Vol.56,Nos ¾, pp.359-370

# 3. The Proximity effect

## 3.1 The proximity effect

When a superconducting layer is put in contact with a non-superconducting film, that is normal metal or ferromagnetic material, some physical properties of the former are transferred to the second within a certain spatial region. This phenomenon, named *proximity effect*, has been extensively studied (see Misener [65] , Smith et al. [66], but McMillan [67] was the first to introduce a simple model to describe multi-layer characteristics of double laeyer structures when they are sufficiently thin to neglect any spatial dependence of the physical parameters. More recently, Golubov et al. [68] proposed a model based on Usadel equations, and generalizing McMillan's model adding coordinate dependence of the order parameter.. The basic channel to have a coupling between a normal and a superconducting layer leading to a transfer of carriers through the interface is related to the so called Andree reflection. In the following, we present the general charactirstics of such a charge and phase mechanism.

### 3.1.1 Particle transmission through a S-N interface : Andreev reflections

Macroscopic description of particle transmission through a Supercondicting-Normal metal (SN) interface has been proposed firstly by Andreev [69] in 1964. He showed that quasi-particle waveform functions for electrons and holes are correlated because they have both to satisfy a continuity relation at interface S-N. The behaviour of excited carriers within an S-N type system is well described by wave-functions solutions of Bogoliubov and De Gennes [70] equations, quite similar to BCS theory ones [71] for homogeneous superconductors but now in the presence of position-dependant potentials.
A system of equations can be written : it involves electron wavefunctions $\eta(x,t)$, hole ones $\chi(x,t)$ and the potential $\Delta(x)$, that represents the condensation energy of a Cooper pair in the superconductor:

$$\begin{cases} \left[ -\frac{\hbar^2}{2m}\nabla^2 - \mu \right]\eta + \Delta\chi = i\hbar\frac{\partial\eta}{\partial t} \\ \left[ -\frac{\hbar^2}{2m}\nabla^2 - \mu \right]\chi + \Delta\eta = i\hbar\frac{\partial\chi}{\partial t} \end{cases} \tag{3.1}$$

Typical solutions for eta and chi are sketched in Fig. 3.1.

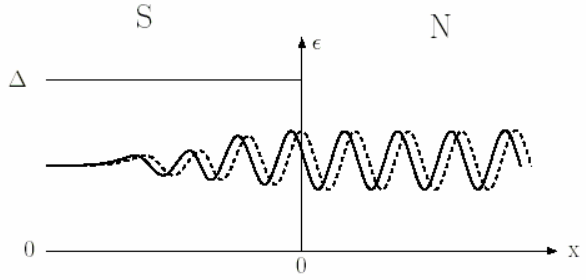


**Fig 3.1**: Representation of an Andreev state at interface o fan S-N bylayer: electron wave functions (continuous line) and hole ones (dotted) present a constant magnitude by N side but they attenuate in S side. Notice the $\varphi_0$ dephasing occurring at interface.

In the case of a perfect interface, solutions for energies $\varepsilon$ $0<\epsilon<\Delta$ ($\epsilon$ is measured with respect to Fermi level $\mu$) and wave vector $k>0$ can be found in the form

$$x>0,\begin{bmatrix}\eta\\ \chi\end{bmatrix}_N = e^{i(k_e x-\varepsilon\, t/\hbar)}\begin{bmatrix}e^{i\phi_0}\\ 0\end{bmatrix}+e^{i(k_h x-\varepsilon\, t/\hbar)}\begin{bmatrix}0\\ 1\end{bmatrix} \tag{3.2}$$

$$x<0,\begin{bmatrix}\eta\\ \chi\end{bmatrix}_S = e^{i(k_S x-\varepsilon\, t/\hbar)}\begin{bmatrix}e^{i\phi_0}\\ 0\end{bmatrix} \tag{3.3}$$

$$k_e = k_F + \frac{\varepsilon}{\hbar \mathrm{v}_\mathrm{F}} \tag{3.4}$$

$$k_h = k_F - \frac{\varepsilon}{\hbar \mathrm{v}_\mathrm{F}} \tag{3.5}$$

$$k_s = k_F - i\frac{\sqrt{\Delta^2-\varepsilon^2}}{\hbar \mathrm{v}_\mathrm{F}} \tag{3.6}$$

$$\phi_0 = \varphi - \arccos\left(\frac{\varepsilon}{\Delta}\right) \tag{3.7}$$

Inside the superconductor, an excited state at energy $\epsilon<\Delta$ is an evanescent wave (see complex nature of $k_S$), while in a normal metal the overall state is made by one excited electron on k>kF and a hole at k<kF at the same energy but at a phase difference $\varphi_0$. This parameter depends on the ratio $\frac{\varepsilon}{\Delta}$ and on the macroscopic phase of the superconductor according to equ. (3.7) [72]

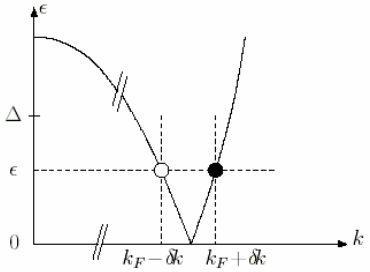


**Fig. 3.2:** Dispersive relation of the excitation electron type and hole type in a normal metal ; wave vector difference between electron and hole of an Andreev pair by energy $\epsilon<\Delta$.

Within the normal metal, electron-type and hole-type components are departed because the different nature of their excitations. The two particles have different wave vectors, the electron above Fermi level with a $k_e=k_F+\delta k$ , the hole with a $k_h=k_F-\delta k$ , both equal excitation energy $\epsilon$ (Fig.3.2). Relation of continuity with fading state in the superconductor is the origin of their phase coherence at the S-N interface (see Fig 3.1). .

When an electron with $k_{e1}= k_F+\delta k$ reaches normal metal interface (see Fig.3.3), he "tries" to pass over into the normal metal but he cannot since the condensate must o contain only paired electrons as Cooper pairs. It follows that a second electron is compelled to leave S positioning itself under the Fermi level with an opposite wave vector $k_{e2}=-(k_F-\delta k)$ and recombining together with a hole by $k_h=k_F-\delta k$ in the normal metal. Transferred electron and absorbed hole constitute an *Andreev pair* by energy $\epsilon=\hbar v_F \delta k$ respect to $E_F$.

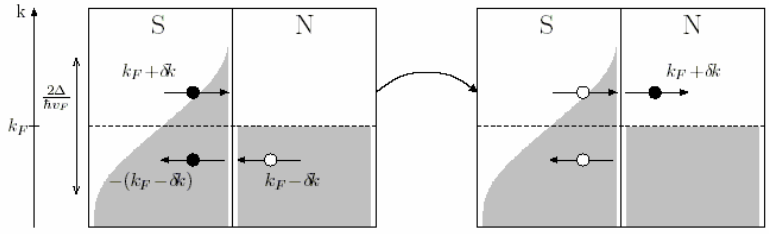


**Fig. 3.3:** Two electrons passing from superconducting "condensate" (S) to normal metal (N): passage is direct for the electron below Fermi level when it recombines with a hole of Andreev state.Grey zones represent busy states versus wave vector k at T=0 in both the condensate S and the Fermi sea in N.

The existence of a pair of electrons by $k>k_F$ in the superconducting state is the origin of the presence of electrons above $E_F$ in the normal metal also at T=0. Such a transfer of electrons from superconductor can be seen as a reduction (depletion) of super-electrons condensate near the interface: this is the *inverse proximity effect*.

Let's consider the case when (see Fig. 3.4) an electron with $k_{e1}= k_F+\delta k$ comes from normal metal above the Fermi level and penetrates the superconductor.

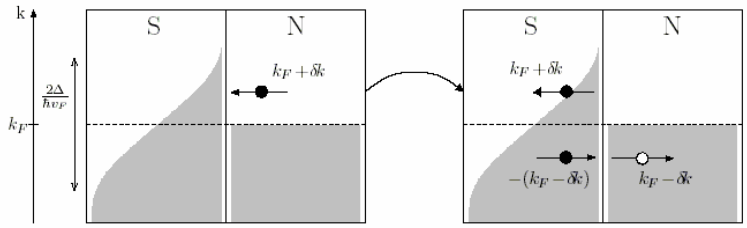


**Fig. 3.4**: An electron passing from normal metal (N) to superconductor (S): in this case Andreev state is made of the elecrton coming (recalled) under the Fermi level from N to S and of the hole that , in N, moves away from interface in the Fermi sea.

Condensate must now integrate a pair number of electrons so a second electron by $k_{e2}=-(k_F-\delta k)$ is taken under Fermi level leaving a hole by $k_h=k_F-\delta k$ in the normal metal. The hole is told "back-reflected" treating of vectors by the same direction of incident electron.The couple of electrons that overlapped interface are further integrated into the condensate, so this mechanism equals to a Cooper pair transfer starting from an incident electron from N.

Within an S-N bilayer, wave functions associated to electron and hole of Andreev pair are coherent inside the normal metal because the former is solution of the latter in the retro-reflection process at S interface. Trajectories overlap because wave vectors are parallel, frequencies are equal because energies are the same, both over and under the Fermi level. Waves could therefore interfere if the were of the same nature, but it is not like that: the electron is a real particle while the hole is only a lack of electron inside the Fermi sea. Moreover, they don't have the same spin since reflection invert the spin direction (?). Coherence, therefore, is not the consequence of the electron-hole interference in terms of associated waves, but, considering a double process of Andreev reflections, is what allow the conversion of a hole into a second electron that interfere with the initial one. This can realized in the presence of a second N-S interface coupled to the first one in an overall S-N-S structure (Fig. 3.5a) to obtain the coherent state in N: in this way, it is possible to transfer the coherence between the two superconductors through the normal metal (N layer). From a qualitative point of view, the above process extends the macroscopic quantum order (*i.e.* superconductivity) through the normal layer. There is also the possibility to have a coherent reflection through the completely diffusive motion of carriers inside N, which undergoes many elastic collisions up to revert to S-N interface, where they are Andreev-reflected and transformed into holes. These latter follow a path similar to that of the former electron up to be Andreev-reflected producing a new electron able to interfere with the first electron. Such a mechanism occurs only if coherence is not lost during the whole path L (-impurities inside the material play a fundamental role-) and the interference between the two waves must be constructive..

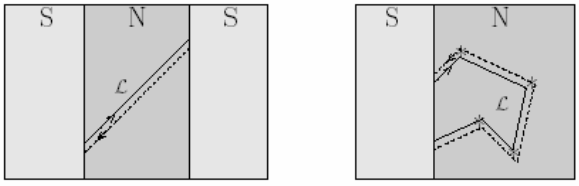


**Fig. 3.5:** Possible trajectory of an Andreev pair in diffusive regime (right); in the ballistic case (left) a second reflection can be seen occurring on the second N-S interface and generating interfering ; L is the total length of the trajectory between the two Andreev reflections.

In the case of zero energy, relative phases of electron and hole are the same in each point of the trajectory and thus the wave vectors equal each other, i.e. $k_e=k_h$ .The trajectories are perfectly overlapped and elastic collisions diffuse the two particles in the same direction: they remain coherent also on trajectories whose length is $L_\Phi$ i.e. the maximum coherence characteristic length. At finite values of energy, the electron and hole of an Andreev pair

have different wave vectors $k_e - k_h = \frac{2\varepsilon}{\hbar v_F}$ and the wave associated to the hole dephases progressively along the trajectory: the dephasing overlap 2π when the hole cover a path equal to $L > \frac{\hbar v_F}{\varepsilon}$ . Under such conditions, in a process of elastic diffusion on an impurity or defect, the most probable direction of the diffused wave vector is not more the same for starting electron and back-reflected hole, so the cannot interfere. However a characteristic length exists within whom the coherence can be preserved. This parameter is $L_\varepsilon = \sqrt{\frac{\hbar D}{\varepsilon}}$, where *D* is the diffusion length. At finite temperatures, the characteristic length is a function of T according to $L_T = \sqrt{\frac{\hbar D}{2\pi k_B T}}$. In Fig. 3.6 the different highlighted characteristic lengths are shown versus characteristic energies.

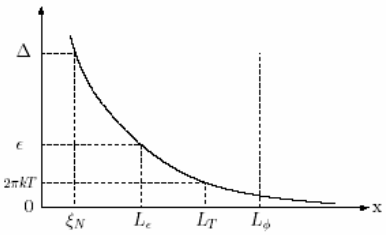


**Fig. 3.6:** Energy of an Andreev pair and characteristic lengths.

Considering the energetical aspects connected to Andreev pairs motion within a normal metal it is useful to consider a complex structure S-N-S that represents the generalization of a S-N bilayer supposing a double thick of the normal layer. The supercurrent presence in the structure, sign of a superconducting coupling between the two electrodes, is a direct consequence of the existence in N of energetic states available to Andreev pairs.

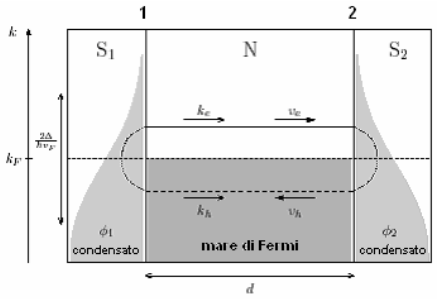


**Fig. 3.7:** S-N-S junction of length d in "ballistic regime". Notice that the "Andreev bound state" induces an electron to be over $E_F$ and a hole below by equioriented wave vectors but opposite group velocities.

The supercurrent that flows across the structure depends on the macroscopical phase difference $\Phi=\Phi_2-\Phi_1$ between the two superconductors S1 and S2 and therefore on Andreev reflections occurring at the interfaces. Referring to Fig.3.7, it can be observed that *Andreev bound states*, i.e. states that verify the constructive interference conditions following to reflections at the interfaces, can exist only if the phase coherent length $L_\Phi$ is larger than the physical dimension d of the junction, i.e. $L_\Phi > d$.

In the case of a pair by finite energy $0<\varepsilon\ll\Delta$, the wave vector of the electron in a pair presents higher absolute value, $k_e>k_h$, relative phase of the two waves associated to particles is not more constant within the normal metal and between the two interfaces the quantity $\Delta\varphi = +\frac{2\varepsilon d}{\hbar v_F}$ changes. If inside normal metal happens that $\Delta\varphi=\pi$, then the overall phase change of the pair is zero because $\varphi_1=-\pi/2$, $\varphi_2=+\pi/2$ and then $\Delta\varphi=\varphi_2-\varphi_1=\pi$ in the metal. In general, such a condition is verified for all the odd multiples of π, that correspond to equidistant levels of discrete energy:

$$\varepsilon_n = (2n+1)\frac{\pi}{2}\frac{\hbar v_F}{d} = (2n+1)\frac{\pi}{2}E_{Th} \ , \ n = 0,\pm1,\pm2,... \quad \varepsilon_n << \Delta$$

where $E_{Th} = \frac{\hbar v_F}{d}$ defines the *Thouless energy* (in ballistic regime) and $E_{th}<<\Delta$.

The shorter is the junction, the more spaced are energy levels. When $E_{th}\approx\Delta$, previous relation is not more valid and we have to consider the phases dependence to ε in interfaces relations $\varphi_1 = \Phi_1 - \arccos\left(\frac{\varepsilon}{\Delta}\right)$ and $\varphi_2 = \Phi_2 - \arccos\left(\frac{\varepsilon}{\Delta}\right)$ with $k_e>0$.

Supercurrent expression is then a periodic function (by 2π period) and it can be proved that supercurrent maximum is a function of macroscopical phase difference Φ: $I_S(\Phi) = 2\Phi\frac{E_{Th}}{eR_n}$

where $\frac{1}{R_n}$ is the N conductance in ballistic regime. The above considerations can be directly translated in terms of density of states (DoS) within the metal N with Andreev reflections occurring (of course in presence of a coupled superconductor S). In particular, in the ballistic regime (one-dimensional case), the presence of a discrete number of energetic levels by ε<Δ available for particular *trajectories* of the electron moving through N, is shown in the shape of the DoS sketched in Fig. 3.8 that in fact presents discrete states in this energy interval. For the three-dimensional case, in the diffusive regime, we must consider the *diffusive path*: for each ε a path exists $\mathcal{L}$ that satisfies the coherence conditions and then it happens that the DoS becomes a continuum of Andreev bound states, as depicted in Fig. 3.9 . Qualitatively, we expect that because of the diffusive mechanism occurring, a minimum value of energy exists starting from whom the coherence of the states begins to appear. That's the *mini-gap* $E_g = \frac{\pi}{2}E_{Th}$ origin showed in the DoS at Fig. 3.9 .

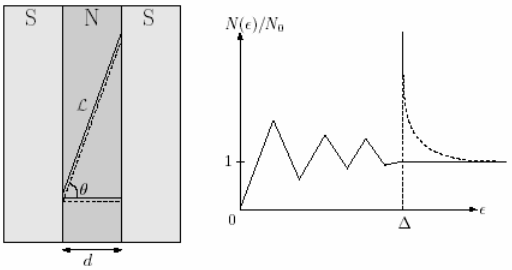


**Fig. 3.8:** Ballistic trajectory of an Andreev pair; (right) qualitative behaviour of the DoS showing some peaks in energy of bound states for θ =0.

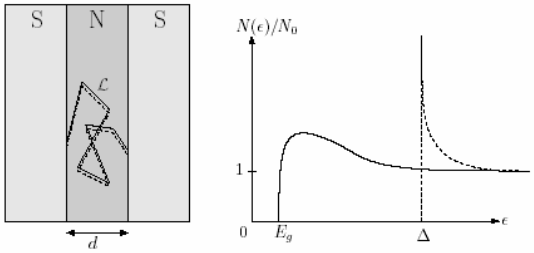


**Fig. 3.9:** Diffusive trajectory in a S-N-S junction and mini-gap in the DoS.

As already seen, the current induced by Andreev reflections in the normal metal can cause the escape of Cooper pairs from a superconductor. Direct proximity effect can be easily explained in terms of Andreev states but this is not so evident for the inverse-proximity effect: electrons leave the condensate and occupy Andreev states that propagate in normal metal. This conversion process among condensed Cooper pairs and Andreev pairs involves a layer $\xi_S$ thick at the superconductor interface: within this region, the condensate has got less pairs (disappeared for creating Andreev pairs) and energy gap reduced itself (Fig.

3.10). The gap reduction at S-N interface depends on pairs quantity that can overlap the interface and on how their coherence is destroyed. The gap reduction in S is a function of normal metal conductivity and of the interface transparency.

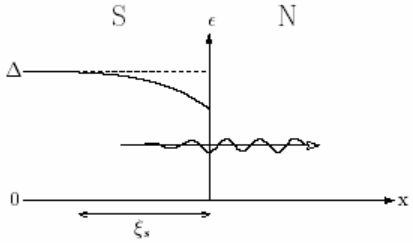


**Fig. 3.10:** Inverse proximity effect with reduction of the gap at the interface due to escape of Cooper pairs into the Andreev states.

## 3.1.2 Proximity effect in $S_1$-$S_2$ structures: the Golubov model

Let's consider now the case of two superconductors joined together to form a bilayer: $S_1$ qand $S_2$ have arbitrary thickness, $l_{S_{1,2}}$ are their mean free paths and $\xi_{S_{1,2}}$ their coherence lengths respectively $\xi_{S1,2} = \sqrt{\frac{D_{S1,2}}{2\pi T_C}}$. Let's suppose $l_{S_{1,2}} \ll \xi_{S_{1,2}}$ (called *dirty limit conditions*).

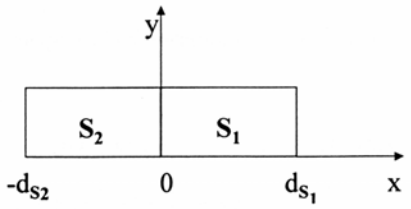


**Fig. 3.11:** Bilayer made of two superconductors.

The study of a multi-particle self-interacting system represents a quantum mechanic problem very complicated that can be solved by approximations. Under a qualitatively point of view, the system can be described by a Schröedinger-type equation solved by a particolar function, the *Green function*, tied to system wave-functions through energies $E_n$, this because the particle interactions expressed by suited potential depending on the positions.
Let's consider the $S_1/S_2$ interface as origin of the reference system (Fig. 3.11) and $d_{S1}$ and $d_{S2}$ respectively the thicknesses, the properties related to the carriers motion inside the superconductors can be described in a quasi-classical way by the following relations (in S1):

$$\frac{D_{S1}}{2}\left( G_{S1}(\omega_n,x)\frac{\partial^2 F_{S1}(\omega_n,x)}{\partial x^2} - F_{S1}(\omega_n,x)\frac{\partial^2 G_{S1}(\omega_n,x)}{\partial x^2}\right) + \\ +\omega_n F_{S1}(\omega_n,x) - \Delta_{S1}(x) G(\omega_n,x) = 0 \tag{3.8}$$

where $G_{S1}(\omega_n,x)$ e $F_{S1}(\omega_n,x)$ are the Green functions and $\Delta_{S1}(x)$ is the pair potential in S1 , $\omega_n = \pi T(2n+1)$. In the same way $S_2$ can be analysed. The F and G Green function can be thought to be functions describing both the aspect of "normal" and "super-conducting" electrons. The pair potential is, in general, solution of a self-consistency equation like

$$\Delta_S(x)\ln\frac{T}{T_{CS}} + 2T\sum_{\omega_n}\left[\frac{\Delta_S(x)}{\omega_n} - F_S(\omega_n,x)\right] = 0 \tag{3.9}$$

where S=$S_1$ or S=$S_2$. For simplicity of calculation, Green function can be written in a parametric form:

$G_S(\varepsilon,x) = \cos\vartheta_S(\varepsilon,x)$ and $F_S(\varepsilon,x) = \sin\vartheta_S(\varepsilon,x)$

with $\vartheta_S$ function satisfying the equation

$\xi_S^2 \vartheta_S''(x) + i\varepsilon \sin\vartheta_S(x) + \Phi_S(x)\cos\vartheta_S(x) = 0$ .

Starting from solutions of previous equations it is possible to go back to the DoS expression of the quasi-particles and Cooper pairs that can have the form (respectively)

$$N_S(\varepsilon, x) = \mathrm{Re}\left[\cos\vartheta_S(\omega = -i\varepsilon, x)\right] = \mathrm{Re}\left(\frac{\varepsilon}{\sqrt{\varepsilon^2 - \Phi_S^2(\varepsilon, x)}}\right) \tag{3.10}$$

and

$$P_S(\varepsilon, x) = \mathrm{Re}\left[\sin\vartheta_S(\omega = -i\varepsilon, x)\right] = \mathrm{Re}\left(\frac{\Phi_S(\varepsilon, x)}{\sqrt{\varepsilon^2 - \Phi_S^2(\varepsilon, x)}}\right)$$

with $\Phi_S(\omega_n, x) = \omega_n \tan\vartheta_S(\omega_n, x)$.

Equations (1) and (2) are verified using boundary value conditions for x=0 ($S_1/S_2$ interface)

$\gamma_B \xi_{S2} \vartheta_{S2}' = \sin(\vartheta_{S1} - \vartheta_{S2})$

$\gamma \xi_{S2} \vartheta_{S2}' = \xi_{S1} \vartheta_{S1}'$

while at free surface of the two superconductors must be

$\vartheta_{S2}'(-d_{S2}) = 0; \qquad \vartheta_{S1}'(d_{S1}) = 0;$

Characteristic parameters of above model are :

$$\gamma = \frac{\rho_{S_1}\xi_{S_1}}{\rho_{S_2}\xi_{S_2}^*}$$

$$\gamma_B = \frac{R_B}{\rho_{S_2}\xi_{S_2}^*}$$

where $\rho_{S_{1,2}}$ are the resistivities inside the two superconductors in the normal state (not proximized), $\xi_{S_2}^* = \xi_{S_2}\sqrt{\frac{T_{c,S2}}{T_{c,S1}}}$ and $R_B$ is the product between the interface $S_1$-$S_2$ resistance and the area of interface plane.

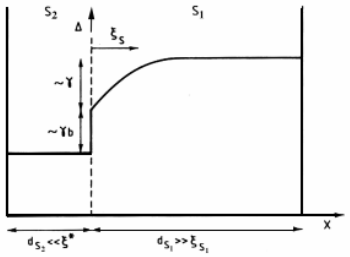


**Fig. 3.12:** Parameters of the proximity effect versus position.

$\gamma$ indicates ratio between quasi-particles density in $S_2$ and in $S_1$, nearby $S_1$ - $S_2$ interface; for $\gamma > 1$, quasi-particles diffusion within $S_1$ involves a suppression of the order parameter on lengths around $\xi_S$ (see Fig.3.12).

$\gamma_B$ parameter, instead, indicates (related to) the two superconductors' barrier transparency; the case $\gamma_B$ <<1 represents a barrier of potential that annul itself at $S_1$ - $S_2$ interface i.e. the two superconductors are in a very good electric contact, instead the opposite case indicates a low transparency barrier, so the two materials are weakly coupled. If the superconductors are very thin ($d_S \ll \xi_S$), the Golubov model reduces to McMillan one, in fact, in such a case, the expression of quasi-particles DoS (3) coincides to McMillan one being the pair potential $\Phi_S$ constant inside superconductors. In Fig. 3.13 is reported a few behaviours of DoS obtained from Nb-Al (S-N) bilayers for different value of macroscopic parameters. Notice how DoS in $S_2$ is a function of its the thickness and tends to $S_1$ DoS in the case of very little thicknesses (McMillan).

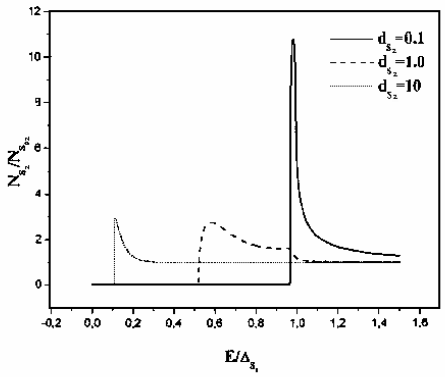


**Fig. 3.13:** Behaviour of the DoS within a $S_1$-$S_2$ bilayer (see text).

## 3.2 Proximity effect in S/F bilayers

In the previous discussion about proximity effect between a superconductor and a normal metal, it has been considered that in Andreev pair, electron and hole had opposite spins: this consideration becomes false when the superconductor proximizes a ferromagnetic material that is characterized by an electronic population in which a precise spin orientation prevails.

In a metal, electronic population is not characterized by a preferred spin orientation, even at T=0, hence two electrons by opposite spin (e.g. the case of a Cooper pair in a superconductor) can tie together because coulombian prevailing forces. In a ferromagnet, instead, the most of electronic population own a same spin orientation: in such a case, coulombian repulsion is less than magnetic forces, i.e. there is an exchange interaction between electrons with parallel spins which show a repulsion energy lower to the anti-parallel spin electrons one .

The link in terms of energy that is created between two near electrons is described by an *exchange Hamiltonian* that formally transpose a second order interaction of dipolar type between spins with the same direction:

$$H_{ij} = -J_{ij}\vec{s}_i \cdot \vec{s}_j$$

If between two electrons with opposite spins a coulombian repulsion Vc exists and if N is the number of electrons of population in the paramagnetic state, $N^2$ combinations can occur of electrons by twos with anti-parallel spins and global repulsion energy is worth $N^2V_C$ .

In the ferro-magnetic case, symmetry can brake between the two populations of electrons by $N\uparrow=N+\delta N$ and $N\downarrow=N-\delta N$: the number of possible combinations becomes $N\uparrow\ N\downarrow=N^2-\delta N^2$ and the energy of repulsion connected to such a variation is worth $V_C\delta N^2$ .

Thus the δN electrons that have changed the spin, they have to pass into the state by superior kinetic energy in the measure of $\delta E_C$ because all other states are already occupied (Fig. 3.14). Acquired kinetic energy is tied to the density of states $N_0$ through the relation $\delta N= N_0\delta E_C$, then the increase of the global kinetic energy becomes $\delta E_C\delta N= \delta N^2/ N_0$ .

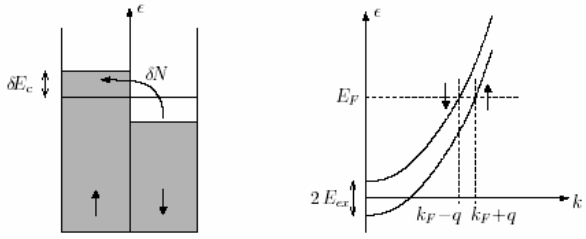


**Fig. 3.14: The Stoner Model (left) that descrive the "walking" ferromagnetism; Fermi wave-vectors (right) of the two spin populations inside a ferromagnet.**

In order that all the system reaches a minimum of total energy, it must happen that the increase of the coulombian repulsion energy overlaps the excess of kinetic energy: a criterium exists to satisfy such a condition , the *Stoner criterium* [73], according to whom the condition $V_C\delta N^2 > \delta N^2/N_0 \Rightarrow N_0V_C>1$ must be verified.

The total energy of a majority-spin electron is less than a minority-spin electron one because it is subject to a lower coulombian repulsion ($V_CN\uparrow<V_CN\downarrow$) : the system is in equilibrium and, by the moment that the total chemical potential μ (total energy) is the same for the two populations, the kinetic energy of a majority electron results in being grater than a minority electron one.
The excess of kinetic energy respect to a mean value $E_F$ is called *Exchange Energy* ($E_{ex}$)
The kinetic energy at Fermi level of electrons by majority and minority spin respectively is: $E_F\uparrow = \overline{E}_F + E_{ex}$ and $E_F\downarrow = \overline{E}_F - E_{ex}$. In the same way the wave vector at Fermi level can be defined considering the contribution due to the exchange $k_F\uparrow = \overline{k}_F + q$ and $k_F\downarrow = \overline{k}_F - q$ where $q = \frac{E_{ex}}{\hbar v_F}$, with $E_{ex} << E_F$. The process of Andreev reflections between a superconductor and a ferromagnetic metal (S-F) is similar to the one in S-N structures. Nevertheless, because the two energetic bands by anti-parallel spin are separated by a 2Eex energy gap, a spin-up electron and the reflected spin-down hole have different wave vectors, $k_e\uparrow=k_F+q$ and $k_h\downarrow= k_F-q$. Therefore the difference between these momenta produces a dephasing of the pair at zero energy: this is a new phenomenon not occurring in the S-N case. The relative phase of the electron versus the hole develops according to the relation $\Delta\varphi=\pm 2qx$, where + and – signs refers to pairs (e↑,h↓) ed (e↓,h↑). Wave functions dephase on a distance $\xi_F$ that becomes a new characteristic length . In the ballistic regime, is $\xi_F = \hbar v_F / E_{ex}$ and in the diffusive regime $\xi_F = \sqrt{\frac{\hbar D}{E_{ex}}}$, where D is the diffusion coefficient in F. Typically, $\xi_F<\xi_S$ and this is an immediate consequence of the greater dephasing in which Andreev pairs occur during their motion through a ferromagnetic material *proximized* by the presence of a superconductor.
If $E_{ex}<\Delta$, the $E_{ex}$ roll above the DoS can be understood through Fig. 3.12 [74], taking in count what discussed in the previous paragraph, in particular for the case $\Phi=\pi$ (how showed if Fig.3.12, continuous line), the overall order parameter is zero in F because supercurrent goes to zero: this means that the DoS will approach the one of a normal metal, and then with the presence also at $\varepsilon<\Delta$ of available energetic states differently to the BCS-like example (dotted line). Changing $E_{ex}$ as well as the other model parameters a series of curves can be obtained by shapes included within the two showed in Fig.3.15 .

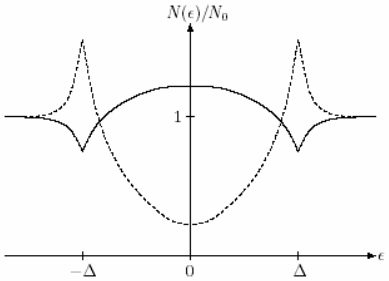


**Fig. 3.15:** Density of States at free surface (F side) of a S-F bilayer in the case for which $E_{Th}>\Delta$ ; dotted : $E_{ex}< E_{Th}$ ; continuous : $E_{ex}\approx E_{Th}$ , that is $\pi = qd = \frac{2E_{ex}d}{\hbar v_F} = \frac{2E_{ex}}{E_{Th}}$.

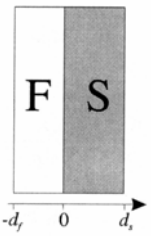


**Fig. 3.16:** typical configuration of an S-F bilayer.

Under the dirty-limit hypothesis (mean free path<<ξ), and referring to the geometrical configuration shown in Fig. 3.16, equations for the Green function G and F assume the form [75]

$$\xi_S^2 \frac{\pi T_C}{\omega G_S} \frac{\partial}{\partial x}\left[ G_S^2 \frac{\partial}{\partial x}\Phi_S \right] - \Phi_S = -\Delta \qquad \text{for } 0<x<d_S \tag{3.11}$$

$$\xi_S^2 \frac{\pi T_C}{\tilde{\omega} G_F} \frac{\partial}{\partial x}\left[ G_F^2 \frac{\partial}{\partial x}\Phi_F \right] - \Phi_F = 0 \qquad \text{for } -d_F<x<0 \tag{3.12}$$

where the pair potential is defined by $\Phi = \frac{\omega F}{G}$, $T_c$ is the critical temperature of the superconductor and $\Delta$ is the gap (not zero only within S), $\omega$ is the Matsubara frequency. The coherence lengths $\xi$ are related to diffusive coefficients D by the relation

$$\xi_{S(F)} = \sqrt{\frac{D_{S(F)}}{2\pi T_C}} \ .$$

The pair potential satisfy also the auto-consistance equation of the kind

$$\Delta \ln\frac{T}{T_C} + \pi T \sum_n \frac{\Delta - G_S \Phi_S \operatorname{sgn}\omega}{|\omega|} = 0 \ . \tag{3.13}$$

Boundary conditions at S-F interface become

$$\frac{\xi_S G_S^2}{\omega}\frac{\partial}{\partial x}\Phi_S = \gamma \frac{\xi_F G_F^2}{\tilde{\omega}}\frac{\partial}{\partial x}\Phi_F \tag{3.14}$$

$$\gamma_B \frac{\xi_F G_F}{\tilde{\omega}}\frac{\partial}{\partial x}\Phi_F = G_S\left(\frac{\Phi_F}{\tilde{\omega}} - \frac{\Phi_S}{\omega}\right) \tag{3.15}$$

with $\gamma_B = \frac{R_B A}{\rho_F \xi_F}$ and $\gamma = \frac{\rho_S \xi_S}{\rho_F \xi_F}$, where $R_B$ and $A$ are resistance and area of S-F interface, $\rho_{S(F)}$ is the S (F) layer resistivity.

When $d_F \leq l_F$, the DoS in the two layers can be obtained directly from $\Phi$

$$N_F(\varepsilon) = \operatorname{Re} G_F(\varepsilon)$$
$$N_S(\varepsilon) = \operatorname{Re} G_S(\varepsilon) \ .$$

Within the work of this thesis, a software for simulation of the DoSes has been used: in this code, a search for solution in the shape $G_{S(F)} = \cos\theta_{S(F)}$ and $F_{S(F)} = \sin\theta_{S(F)}$ has been done, obtaining $\Phi_{S(F)} = \omega \tan\theta_{S(F)}$ both for S than F layer. Consequently, DoSes have been obtained through expressions as $N_{S(F)} = \operatorname{Re}\left(\cos\theta_{S(F)}\right)$, as already done for $S_1$-$S_2$ case. At the end, the S-F bilayer model is quite similar to S-N one with the add of a new parameter $E_{ex}$ and with the definition of the coherence length as function of the same exchange energy.

All the above discussed model becomes a powerful instrument to understand the behaviour of a proximized metal, both normal and ferromagnetic, and justify consequently the usage of a ferromagnetic as cover-layer of a SPD. Independently from the shape of the device, let's focus on the multi-layer structure obtained by deposition of a thin layer of superconductor overlapped by a thinner layer of a weak ferromagnetic metal. Firstly, as well introduced in the first chapter, the dimensions and the thickness of the overall bilayer is fundamental to obtain that enucleation of the hotspot involves the sensor strip both in width as well as in depth. This occurring, the enucleated hot-spot causes a complete transition of the strip and the consequential appearance of time-variant voltage signal propagating through the strip to be read-out by appropriate electronics. Of course, the most thin the strip, the most numbers of photons will penetrate the material so multiplying the possibility to be absorbed and to trigged the electronic energetic cascade well depicted in chapter one. Similarly, the most narrow the strip, the most easier the enucleated hot-spot will cause a complete transition of the strip.

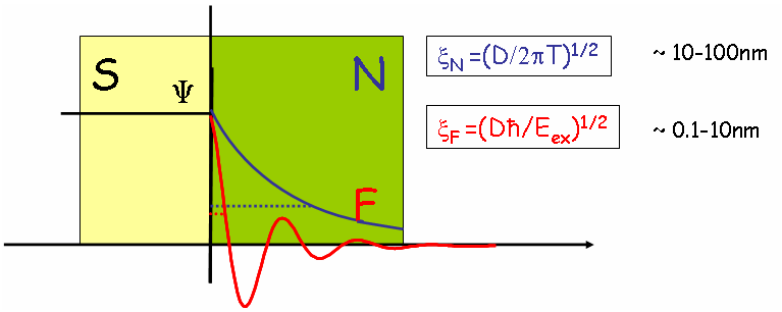


**Fig. 3.17** S-N bilayer: behaviour of macroscopic order parameter.

Eq.(3.11 2) and (3.12) can take to a solution by which macroscopic wave-function Φ has a shape as depicted in Fig 3.17. The superconductivity seems depressed as it should into any proximized metal, but Cooper pair are bosons and the two electrons constituting a pair have opposite spins. This is contrasted by magnetic nature of the proximized material that wants spins oriented in the directions of the majority population: this is the simple consideration that allows to understand the grater depression of superconductivity within such materials. As in literature, $\xi_F$ for Fe,Co,Ni coupled by Nb bulk layer is around 0.7nm, one order of magnitude circa less than the $\xi_S$ of the proximizing superconductor. The $E_{ex}$ role is fundamental in fact majority and minority spin population differ in energy of such value (Fig.3.16) and the system is kept in such a condition of stability (for the Stoner criterium) . Employing weak ferromagnetic materials, it is possible, at the end, realize thinner layer all proximized by thickness comparable to the penetration length (λ) of the photons.

References:

[65] Misener, Transaction Roy Soc Can, 1935,29, pag. 5
[66] P.Smith,S.Shapiro,J.Miles,J.Nicol, Physical Review Letters, 6,686,1961
[67] W.L.McMillan, Phisycal Review, 175, 537 , 1968
[68] A.A.Golubov,E.Houwman,J.Gijsbertsen,V.M.Krasnov,M.Kupriyanov,J.Flokstra, Phisycal Review B,51,1073, 1995
[69] A.F.Andreev , The thermal conductivity of the intermediate state in superconductors, Sov. Phys., JETP 19 (1964),1228
[70] [2] P.G. de Gennes, Superconductivity of metal and alloys, Addison-Wesley,1966
[71] J.Bardeen, L.N.Cooper, J.R.Schrieffer, Theory_of_superconductivity, Phys.Rev.108 (1957) , 1175
[72] M.Tinkham , Introduction to Superconductivity, Mc Graw-Hill, 1975
[73] Hermann Sellier, These de Physique,CEA Grenoble (France) , decembre 2002
[74] T. Kontos et al., PRL 86, p. 304, 2001
[75] K.D.Usadel, Phys.Rev.Lett. 25,507,1970

**Not referenced sources:**

[b] A.Barone , G.Paternò, Physics and Applications of the Josephson Effect, John Wiley and Sons, New York,1982
[c] H.Meissner,Physical Review,175,537 (1968)
[d] Landau,Lifsits,Fisica statistica,Ed. MIR (1997)
[d] V.Z.Kresin , S.A.Wolf , Fundamentals of Superconductivity , Plenum Press , New York and London, 1990
[e] M.Tinkham , Introduction to Superconductivity, Mc Graw-Hill, 1975
[f] T.Van Duzer , C.W.Turner , Principles of Superconductive Devices and Circuits, Elsevier , New York , 1981
[g] L.Solymar , Superconductive Tunneling and Applications, Chapman and Hall LTD , London,1972
[h] I.Giaver , K.Megerle, Study of Superconductors by Electron Tunneling,Phys.Rew. 122,1101-1111,1961
[i] A.Fetter,J.Walecka,Quantum theory of many particle system,McGraw-Hill,1971

# 4. Devices fabrication and characterization

The experimental work proposed in this thesis is mainly focused on the realization and the characterization of superconducting fast devices. The choice of materials plays a fundamental role, and the manufacturing processes employed for the geometries' definition. Accordingly, a brief review of the main characteristics of methods used for thin films deposition, of the lithography techniques, and of the physical etching processes are presented in this chapter. Moreover, the main results in terms of both morphological and transport properties are presented for various materials used for device fabrication as a frame for understanding photoresponse experiments proposed in next sections. Since most of discussed technologies are well established, widely used and largely argumented, we will not present in details but just as an overall landscape.

## 4.1 The sputtering process

Sputtering is a very simple and direct technique which is widely used to deposit highly uniform thin films of varios types of materials (mainly metals, but also oxides). In a typical sputtering system, the material to be deposited is in the form of a pellet called *target*. It is connected to the negative terminal of a dc or RF power supply, and therefore represents the cathode of the system. The substrate that faces the cathode is usually grounded, and heated if requested. After evacuation of the chamber, the process gas, typically argon ( it is a heavy gas, easy to find and characterized by a low ionization potential), is introduced and used serves as the medium by which atoms a discharge is started and sustained. Microscopically, positive ions in the discharge strike the cathode plate and eject neutral target atoms through momentum transfer. These atoms enter and pass through the discharge region and to eventually deposit on the growing film. Using the low-pressure gas and a high impedance dc power supply . the process starts with a very small current that flows at first due to the small number of initial charge carriers in the system. As the voltage is increased, sufficient energy is spread to the charged particles to create more carriers. This occurs through ion collisions with the cathode, which release secondary electrons, and by impact ionization of neutral gas atoms. With charge multiplication, the current increases rapidly, but the voltage, limited by the output impedance of the power supply, remains constant. Large numbers of electrons and ions are created. Eventually, when the electrons generated produce sufficient ions to regenerate the same number of initial electrons, the discharge becomes self-sustaining. At this point the gas begins to enlighten and the voltage drops, accompanied by a sharp rise in current. A further increase in power results in higher voltage and current density causing the real sputtering process to start.

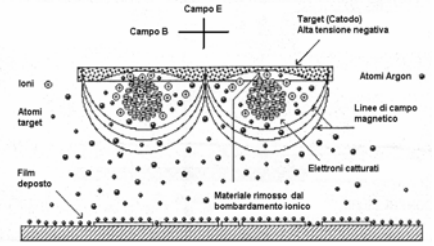


**Fig. 4.1** Sketch of a planar magnetron sputtering source. The presence of a magnetic field traps the electrons near the target, prolonging the electron residence time in the plasma and enhancing the probability of ion collisions.

The addition of a magnetic field to the plasma dynamic is used to enhance the sputtering yield: in fact, . When a magnetic field is superimposed on the electric field between the target and substrate, in this case electrons experience the Lorentz force in addition to electric field force and their trajectory becomes spiral-like. Therefore, magnetic fields enlarge prolong the electron residence time inside the plasma, and thus enhance the probability of ion collisions with ions . This leads to larger discharge currents and increased sputter deposition rates.

Ae very important parameter Fundamental is the distance between substrate and target: if it is too small, it'ld would cause a non-uniform deposition on the substrate, while if too large,

itl'ld would reduce the fraction of atoms number per unit area and time leaving the taget per time unit andwhich depositino on the substrate.
The number of atoms $N$ leaving the target per unit time is given by [76]:

$$N = \frac{J}{qZ}\gamma(E, M_1, M_2)$$

where $J$ is the current density of ions hitting the cathode, $q$ is the electronic charge, $Z$ is the number of charges per ion and $\gamma$ is the yield coefficient of the sputtering process expressed in atoms extracted from the cathode surface per hitting ion. Such a parameter is a function of ion energy $E$, of their atomic weight $M_1$ and of the atomic weight of the sputtered material $M_2$.
There is a Under a certain threshold , phenomenon is ain energy aboe which bsent, the the yeld increases rapidly : the e.g. threshold assumes values between 10eV and 100eV for generally used metals, in particular 10eV for Al, 15eV for Pd or 21eV per il Mo. To minimize the energy request for causing ejection of an atom from the target, sputtering process employs such an energy to obtain a yield of around one atom per ion, that occurs at 100eV circa. The yield decreases over a certain energy because of the ion trapping within target lattice. : this occurs at higher ion kinetic energies. To have an idea of the phenomenon we must consider that the penetration length of $Ar^{++}$ into copper is 10Å/keV, thus 100eV cause 1Å penetration, i.e. they remain on the surface, while $10^4$eV cause 100 Å depth penetration, which not negligible. Moreover, at higher energies, X-ray emissions can occur, and it's a spurious and dangerous effect.

The growth of high oriented thin films can take place in the presence of
The basic theory that accounts for the changes taking place during the formation of an epitaxial film was introduced by Frank and van der Merwe [77]. The theory predicts that any epitaxial layer having a lattice parameter mismatch with the substrate of less than ~ 9%, as in our case, would grow pseudomorphically. At the beginning, the deposit would be elastically strained to have the same interatomic spacing as the substrate; then, with increasing film thickness, the total elastic strain energy increases, and a relaxed structure would form. Regions of relatively good fit are separated by misfit dislocations that relieve a portion of the misfit. As the film continues to grow, more misfit is relieved until at infinite thickness the elastic strain is totally eliminated. The issues just raised with respect to misfit dislocations are but a part of a larger concern for defects in epitaxial films. Such defects which may degrade material properties and many device performances roperties by altering carrier concentrations and mobilities. The sources of defects in epitaxial films can be divided into the following categories [78]:

- Propagation of defects transferred from the substrate into the epitaxial layer:
- Aa classic example of this type of defect is the extension of a dislocation from the substrate surface into the growing film. In order to limit the presence of this type of defect, substrate treatments are usually carried out during the realization of electronic devices. In the case of biepitaxial junctions, the substrates were annealed to allow a partial reorganization of the surface structure or cleaned with a soft etching in oxygen. Another example is represented by the formation of defects in the YBCO films due to twin boundaries in the substrate.
- Stacking faults
- Stacking faults, i.e. are crystallographic defects in which the proper order of stacking planes in
- crystal lattice of the deposited material is interrupted (mainly for epitaxial films).
- Formation of precipitates or dislocation loops due to supersaturation of impurities.:
- Tthe precipitates and dislocations usually are the result of solid-state reactions subsequent to growth. Films containing high dopant or impurity levels are susceptible to such defects and they can change significantly the transport properties of the films.

## 4.2 Photolithography

The lithographic processes have been widely used during this thesis both for film preparation and microbridges definition.

Optical lithography is basically a photographic process by which a light sensitive resist is exposed and developed to form three-dimensional patterns on the substrate. The photoresist image has the exact shape of the intended pattern in the plane of the substrate, with vertical walls through the thickness of the resist; the parts of the substrate covered with resist will be protected from etching. The general sequence of processing steps for a typical optical lithography process is as follows: substrate preparation, photoresist spin coat, pre-bake, exposure and development. A resist strip is the final operation in the patterning process, after the resist pattern has been transferred into the underlying layer using ion milling. Substrate preparation is intended to improve the adhesion of the photoresist material to the substrate. This has been accomplished during this work by substrate cleaning to remove contamination, especially in the form of particulates that could result in defects in the final resist pattern. After cleaning, a thin, uniform coating of photoresist at a specific, well controlled thickness is realized by the process of spin coating: the photoresist is poured onto the sample, which is then spun on a turntable at a high speed, producing a resist film of a controlled thickness. Stringent requirements for thickness control and uniformity and low defect density call for particular attention to be paid to this process, where a large number of parameters can have significant impact on photoresist layer quality. The resist thickness is an important factor in this process, since it influences the exposure and development parameters and the sharpness of the pattern edges. During this work, layers about 1μm thick were found to bring the best results in terms of pattern quality and process reproducibility. After coating, the resulting resist film will contain between 20 – 40% by weight solvent. The post-apply bake process, carried out at 70-100°C, is used to dry the photoresist by removing this excess solvent. The main reason for reducing the solvent content is to stabilize the resist film. At room temperature, an unbaked photoresist film will lose solvent by evaporation, thus changing the properties of the film with time. By baking the resist, the majority of the solvent is removed and the film becomes stable at room temperature. Moreover, the film thickness is reduced, adhesion is improved, and the film becomes less tacky and thus less susceptible to particulate contamination. Typical bake processes leave between 3 and 8% residual solvent in the resist film. Unfortunately, there are other consequences of baking, among them the decomposition of the photoactive resist component, or the oxidizing of another component, the resin. Moreover, the exposure could promote the loss of oxygen and accelerate reactions with $H_2O$ and $CO_2$ to form hydroxides and carbonates (in oxide superconductors this is a big problem). Thus, during this work, the baking temperature and duration were carefully tuned to maximize the benefits of solvent evaporation and minimize the detriments both for the film and the resist. After this preparation steps, the sample is ready for UV exposure. It is placed under a glass mask (photomask) where a layer of chromium reproduces the desired pattern, and UV light is shined on. The areas not covered by chromium will be exposed. Before the exposure of the photoresist can begin, the mask must be aligned. In the case of biepitaxial junctions, the second photolithographic step, needed to define the junctions' bridges, is particularly delicate since it is necessary to align the bridges of the mask in correspondence of the grain boundaries. The alignment process is manual and helped by markers previously patterned in the seed layer mask. Contact and proximity lithography are the simplest methods of exposing a photoresist through the master pattern of the photomask. During this work, contact lithography was used to obtain high resolution: the mask is pressed against the resist-coated sample during exposure. Because of this contact, the gap between the sample and the optical disturbance (the photomask) goes ideally to zero and the diffraction effects, that would distort the pattern, are minimized. Actually, in real systems the mask contact varies across the sample surface, since neither the sample nor the mask is perfectly flat. The major disadvantage of contact lithography is the generation of defects in the sample and the mask due to the contact, but this is a minor inconvenient in the research field. The resolution of this process has two basic limits: the smallest image that can be projected onto the wafer, and the resolving capability of the photoresist. From the projection imaging side, resolution is determined by the wavelength of the imaging light and the numerical aperture (NA) of the projection lens according to the Rayleigh criterion: $R \propto \lambda / NA$. The resolving capability of the photoresist depends on the ability to reconstruct the pattern from the projected image. The resolution achieved during this work was ~1μm. After the patterns have been lithographically printed in photoresist, they must be transferred into the substrate. Etching is the most common pattern transfer approach for devices and will be described later. When the etching is complete, the resist is stripped leaving the desired pattern etched into the deposited layer. The stripping is performed by dipping the sample in an acetone bath sometimes in the presence of ultrasounds.

## 4.3 The Electron Beam Lithography (EBL)

Electron beam lithography is a special technique for creating extremely fine (sub-micron) patterns. Derived from the early scanning electron microscopes, the technique consists in scanning a beam of electrons across the surface which is covered with a resist film sensitive to electrons wavelenght, thus depositing energy in the desired pattern. The electron beam is used as a pencil which is remotely controlled. The resolution is now very high, down to few tens of nanometers. This technique is also very flexible and it can work with a large variety of materials producing an almost infinite number of patterns.

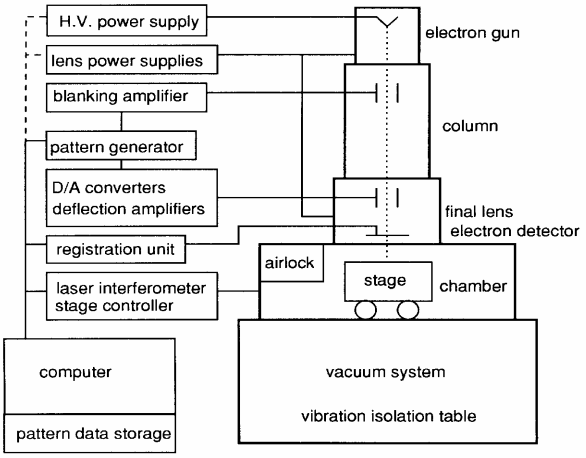


**Fig. 4.2:** Schematics of an EBL system

Fig. 4.2 clearly describes the general EBL system similar to that used at the Saitama University, Japan (Prof. H. Myoren) to fabricate the nanostructures characterized in this thesis. Briefly, a thermo-ionic electron source generates the electron beam further accelerated by an high voltage between two holed electrodes (not shown) under the source. Samples to be processed are firstly spinned by an electron beam sensitive photoresist, then a pattern generator software draw the prepared mask driving the electron beam by electrical and magnetical deflectors voltage controlled. Finally, the beam is focused to the sample by lenses to reach sub-micron resolution.

## 4.5 Ion-Beam processes for etching and cleaning

The ion beam etching technique uses the same sputtering principles explained before with the difference that now the target to be eroded is the sample. Ion milling has significant advantages in terms of directionality, and the erosion rate is not very dependent on the material specie. The basic components of an ion gun are showed in Figure 4.3. A tungsten filament, acting as a cathode, is heated using a voltage $V_f$. The electrons produced are accelerated toward the anode kept at $V_a$ voltage. They impact the argon atoms introduced in the chamber and ionize them. A grid held at a voltage Vg accelerates the ejected ions toward the target where they will impinge removing the material not protected by the mask. Ions arrive at the target surface with an energy given by

$$E_{ion} = q\left|V_p - V_g\right| = q\left|V_a + V_{pa} - V_g\right|$$

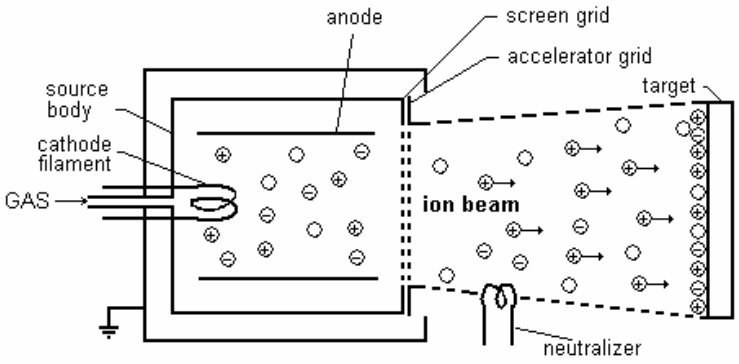


**Fig. 4.3** ION-gun sketch

extracted ion energy is controlled by changing Va and Vg. Other parameters to be tuned to optimize the ion etching or cleaning procedure (the latter obtained using lower voltages) are the argon gas pressure and the sample distance from the ion source and the tilt of the sample stage. Low beam currents and voltages have been used to reduce the damage to the smaller structures. The combination of high power levels and long etching times cause samples to reach high temperatures. It is important to stress that for low width structures the edges of the superconducting film can be severely damaged, and this effect can be quite deleterious for oxide superconductors due to their critical dependence on the oxygen stoichiometry. The depth of these damaged areas depend on many factors, such as the mask quality, the ion etching angle and above all on the parameters used for the ion milling procedure.

## 4.6 Reactive-Ion-Etching (RIE)

Also this process is very similar to the sputtering process and, as well as ion-beam sputtering (ion milling) is not a target but the film itself. The sample is posed on negative electrode and it's hitted by ions: the motion quantity transferred from ions to superficial atoms of target/sample cause them to be ablated Typical pressure for this process is $10^{-2}$ Torr to $10^{-1}$ Torr; electric field direction in usually orthogonal to taget surface thus increasing cutting efficiency and limiting shadows effects, around sample borders, that could (in case of high angle shot) cause resolution problems. As a consequence, lateral eroding speed results much less than vertical one, thus realizing an high anisotropy degree. Nevertheless, in all previously presented etching methods the main disadvantage is the very low selectivity in terms of material that presents quite similar eroding speeds so it is not possible to process one layer without leaving the understanding intact (if this is also subject to the ion attack). For the RIE method, instead, the monoatomic noble gas is substituted with a molecular one, so this plasma assisted technique presents a higher ablating speed because the surface is not simply "mechanically" attacked but also "chemically" weakened. The anisotropy degree also decreases as ions flux increase. The major advantage of this method is selectivity : using different process gasses it is possible to achieve faster erosions on different materials. This means that one specific gas is used to process one specific material: for example to mill Niobium is used a specific $CF_4$ and $O_2$ mixture, where is (F)lourine that reacts with the target metal .

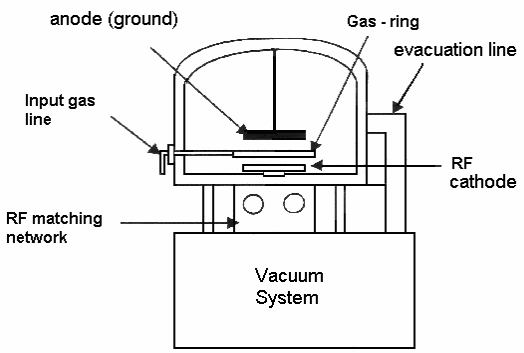

**Fig. 4.5** Typical RIE system

A typical RIE system is sketched in Fig. 4.5. The highly pure gas produces a plasma between plane and parallel electrodes and fluorine chemically act on the niubium generating radicals taken away by pumping system.

## 4.7 Superconducting Used materials for photo-response experiments

Devices measured in this thesis employed various superconducting materials, and their combinations, such as Niobium (Nb), Niobium Nitrate (NbN), and proximized structures in which the normal layer is a metallic weak ferromagnet Nickel-Copper (Ni-Cu) alloy.

Nb and NiCu were deposited by sputtering according to the process described before. In the case of NbN the sputtering was reactive, i.e. the gas used for plasma was a mixture of both Argon and nitrogen.

For Nb films the initial base vacuum was 2*10-7 Torr, and a power of 600W was applied, in the presence of an Argon partial pressure <20 mTorr, corresponding to a deposition rate of 6 Å/s when the substrate was kept at about 8cm far from the source target.

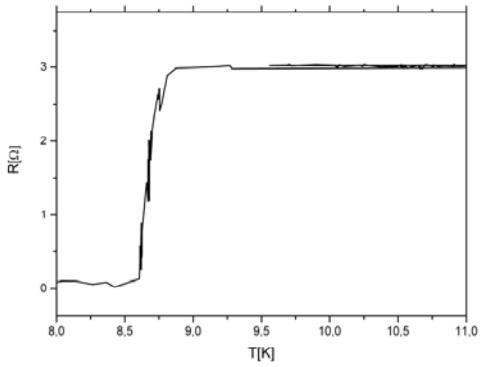


**Fig.4.6** Critical temperature of a 60nm thin niobium film on corning glass.

A typical resistive curve for deposited Nb films is shown in Fig. 4.6 where the critical temperature Tc between 8.7-8.8K is evaluated. The resistive ratio R300/R10 was found to beb close to 2.6 confirming a good quality of sputtered films.

## 4.7.2 Nb and NbN

Niobium Nitrate has been deposited on MgO (manganite oxide) at the Saitama University (Japan) by means of reactive sputtering. The main deposition conditions are summarized in Table 4.1.

Sputtering Conditions for NbN thin films

| | | |
|---|---|---|
| Base Pressure | 2x $10^{-5}$ | Pa |
| Sputtering Gas | Ar(99.999%) $N_2$(99.9999%) | |
| Ar flow rate | 80 | SCCM |
| $N_2$ flow rate | 1.2~ 5.1 | SCCM |
| Gas Pressure | 0.80~ 0.93 | Pa |
| Target-Substrate distance | 8 | cm |
| Dc power | 360 | W |
| Power density | 4.59 | W/$cm^2$ |
| Dep. rate | 20~ 40 | nm/min |
| Thickness | 2~ 20 | nm |

Substrate: MgO(100)
Substrate temperature: ambient temperature

**Table 4.1**

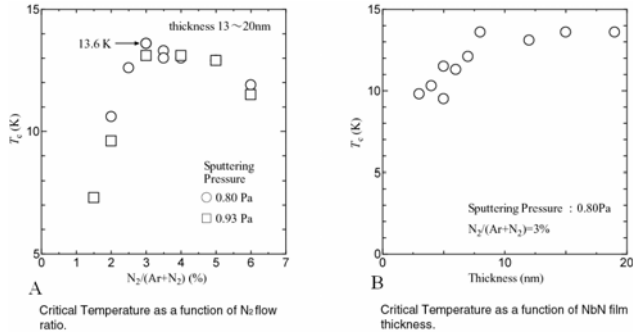


**Fig. 4.7** Critical temperature of sputtered NbN on MgO (Saitama Univ.)

The NbN critical temperature of as deposited NbN thin films was found to be very sensitive both to partial N2 pressure (Fig. 4.7a) and realized film thickness (see Fig. 4.7b). The nitrurization process strictly depends on sputtering gasses pressures, mostly on partial $N_2$ ratio on $Ar+N_2$ mixture. The best quality shows a peak at 13.6K transition temperature for 13-20nm films while less $N_2$ partial ratio strongly degrade superconductivity properties.
It is quite interesting to notice the NbN capability to preserve the superconducting state also for thinner structures (around 3 – 4 nm), and this feature makes it a quite unique choice for superconducting materials to be used as photodetectors of single photon, due to the possibility of high density of energy excitation over small structures.

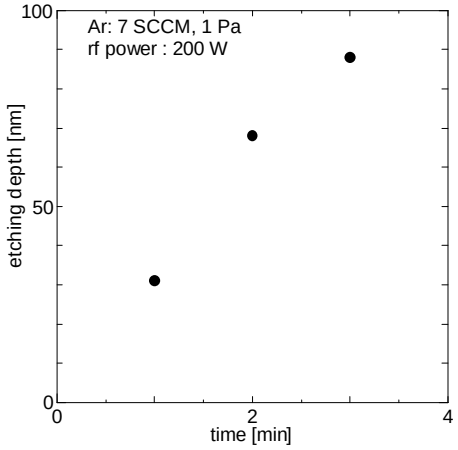


**Fig. 4.8** NbN etching rate > 30nm/min

Etching of NbN thin films (Japan) was performed by standard procedure RF assisted using a power of 200W into an evacuation chamber up to 1pa ($\approx 1.3*10^{-5}$ torr) and a little inert Ar gas flow (Fig. 4.8).

The fabrication of devices based on superconductors proximized structures represents thenovelty of this thesis in the context of non-equilibrium photoresponse. The choice of NiCu as ferromagnetic layer was suggested by it offers a simple capability to tune the magnetic properties by acting on the Ni concentration, its good processability through magnetron sputtering, and hence the easy way to be coupled to Nb-based superconductors.

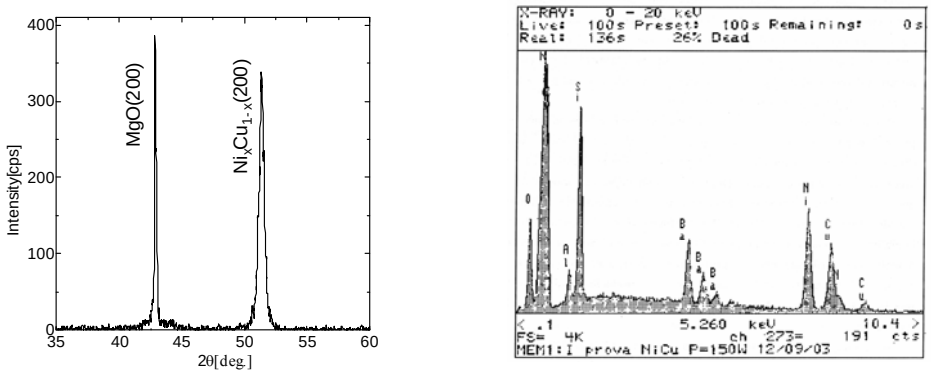


**Fig. 4.9** Comparison X-RD analisys Saitama (left)MgO/NiCu and Naples (right)corning/ NiCu

In Fig.4.9, is shown a XRD $\theta/2\theta$ analysis of a NiCu sputtered sample on MgO: the analysis of the peak position, compared to literature data, and EDS analysis performed on the same samples, suggested that, in spite of a starting $Ni_{0.5}Cu_{0.5}$ target composition, the stoichiometry is close to $Ni_{0.6}Cu_{0.4}$ while in the case of NiCu samples deposited at University of Naples the composition was close to $Ni_{0.48}Cu_{0.52}$.

Several superconductor/ferromagnetic heterostructures have been deposited and characterized using both Nb and NbN as base superconductor.
A typical cross section of Nb/NiCu bilayers is shown in Fig. 4.10a, while in Fig. 4.10b the behaviour of the critical currents of both pure Nb and Nb/NiCu samples with the same geometries are also reported.

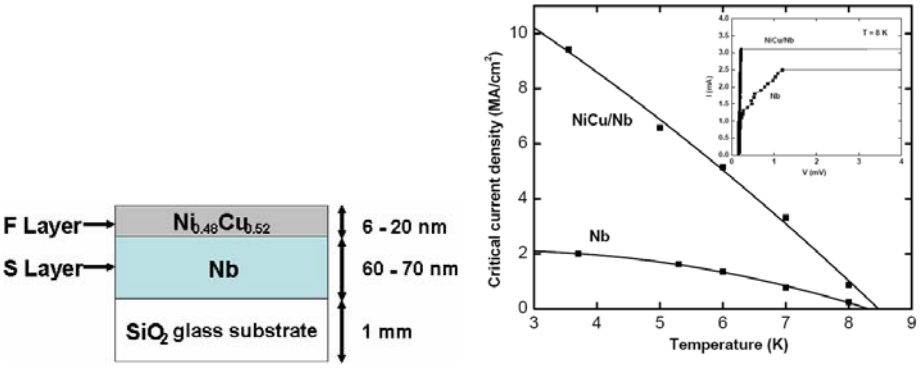


**Fig. 4.10 :** (left) sketch of manufactured $Nb/Ni_{0.48}Cu_{0.52}$ bilayers; (right) critical current density comparison between Nb only and $Nb/Ni_{0.48}Cu_{0.52}$ . In the inset is shown the decreasing of the bilayer $T_c$ if compared to Nb only thin film.

The bilayers were deposited in the different UHV systems, and before the deposition of NiCu the surface of Nb film was etched. In particular, the base pressure for NiCu was $3*10^{-7}$ Torr, the sputtering power was 200 watt, the substrate used was corning glass at 8cm from a 3'' target of the alloy $Ni_{0.5}Cu_{0.5}$.The deposition rate was found to be about 5nm/s in both cases.

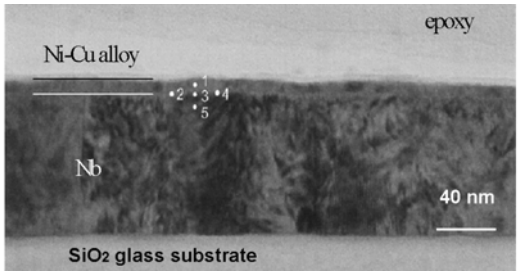


| Position | NiCu layer | NiCu/Nb interface | | | Nb layer |
|---|---|---|---|---|---|
| Point # | 1 | 2 | 3 | 4 | 5 |
| Ni | 52.7 | 73.2 | 72.9 | 62.6 | 54 |
| Cu | 47.3 | 26.8 | 27.1 | 37.4 | 46 |

**Fig. 4.11:** (left) SEM image of a Nb/NiCu section; (right) table of components stoichiometric percentage.

Fig. 4.11 shows a TEM image of a Nb/NiCu bilayer cross section: as expected the alloy composition changes significantly at the interface (see the table on the right): this phenomenon is fundamental because it could explain some interesting features which

appear to be potentially important for nonequilibrium optical response where these added magnetic "impurities" can favourite phase slipping events and/or vortex pinning phenomena. This hypothesis seems to be confirmed by Fig. 4.10b where the presence of the NiCu over-layer produces an increase of the critical current density with respect sole Nb. The presence of the magnetic overlayer results also in a decrease of the superconducting critical temperature Tc of the bilayer (see Fig. 4.12): such a diminution is well predicted by proximity effect through a non-monotonic way; nevertheless, the aims of this thesis are different from such interesting quantum features related to the physics of S/F proximized bilayers. However, the role of vortices in the mechanism of photoresponse will be detailed in next chapters.

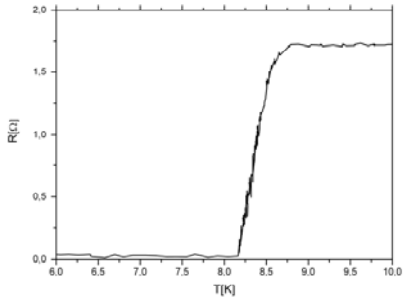


**Fig. 4.12** Resistance vs temperature behaviour of a Nb(70nm)/NiCu(6)nm bilayer

The NiCu thin films were deposited by magnetron sputtering following the conditions summarized in Table 4.2.

Sputtering Conditions for NiCu Films.

| | | |
|---|---|---|
| Base pressure | $2\times10^{-5}$ | Pa |
| Sputtering gas | Ar(99.999%) | |
| Ar flow rate | 80 | SCCM |
| Gas pressure | 0.93 | Pa |
| Target-substrate distance | 8 | cm |
| Dc power | 155 | W |
| Power density | 1.97 | $W/cm^2$ |
| Substrate Temp. | ambient temperature | |
| Dep. rate | 60 | nm/min |
| Thickness | 3∼10 | nm |

**Table 4.2 :** NiCu films on NbN (Saitama Univ.)

Fig. 4.13 shows a comparison between the R(T) vs T curves corresponding to several different samples having the same thickness of NbN as base thin film (100nm). Again, the presence of NiCu presence produces a decrease of the critical temperature of deposited bilayers. In this case, we investigated the dependence of the superconducting critical temperature of the bilayers as a function of the thickness of the magnetic layers.

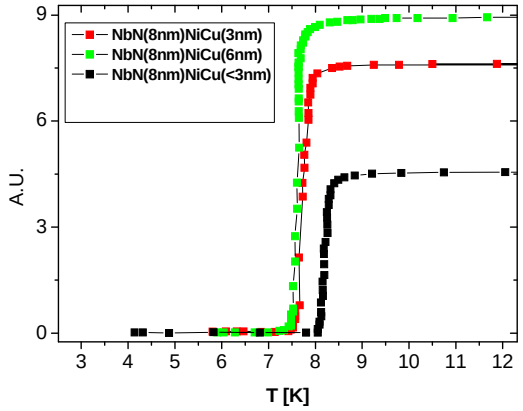


**Fig. 4.13 :** Resistance of NbN/NiCu films versus temperature. Reported graphs refer to three different $Ni_{0.6}Cu_{0.4}$ thicknesses, 6nm, 3nm, ≈2nm.

Fig. 4.14 summarizes the thickness dependence of $T_c$ vs F-layer thickness (dF) for samples measured in photoresponse experiments.

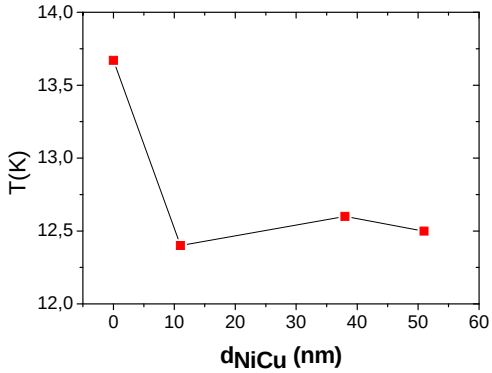


**Fig 4.14** Tc versus $d_F$

As we expect, according to literature [79] the Tc vs $d_F$ is not monotonic and a minimum is possible at T=10K. Nevertheless the poor resolution of measuremente cannot support this hypothesys completely; on the other hand the curve in Fig.4.14 will be used in chapter 6 for evaluating proximity effect parameters.

## 4.8 Micro- and nano-Manufactured structures for photoresponse experiments

The basic patterned geometry we used for photoresponse experiments was the strip (also named bridge), alone or combined to form meander shaped devices. A typical photograph of a realized bridge is shown in Fig. 4.17.

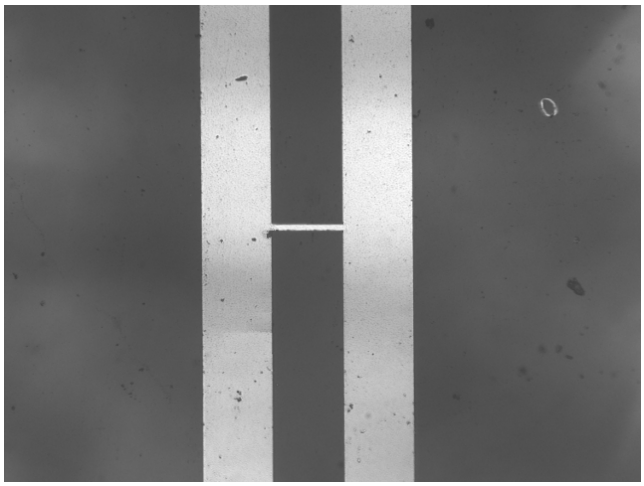

**Fig. 4.17** Patterned "H" shape nanostrip of Nb(100nm)/ NiCu(12nm). The bridge dimensions are: 50μm (lenght) x 5μm (width).

During this thesis, within the collaboration with the Saitama University (Japan), several nanowire configurations have been designed and realized. A typical patterned meander design is proposed in Fig. 4.18

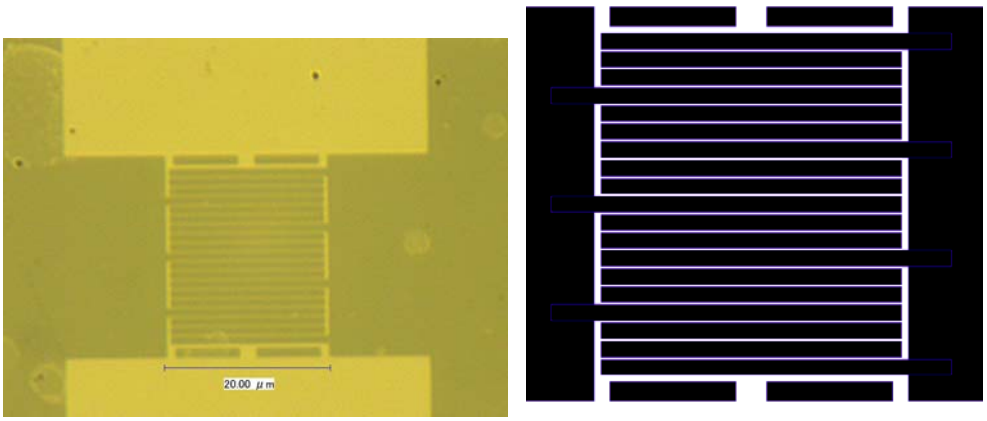


**Fig. 4.18** Patterned meander structure : it is a configuration of 3 parallel by 6 series stripes. Inner stripes thicknesses can vary from 200 to 500 nm in width. (left) microscopy image, (right) CAD drawing.

In particular, the patterned geometries had a meander shape made of three parallel stripes then connected in series of six. Such a choice has been proposed for several reasons:

- to improve the quantum efficiency of the resulting photodetector by increasing the area (meander geometry);
- the parallel configuration has been demonstrated to produce an amplitude gain mechanism during the final operation of photodetection [80].

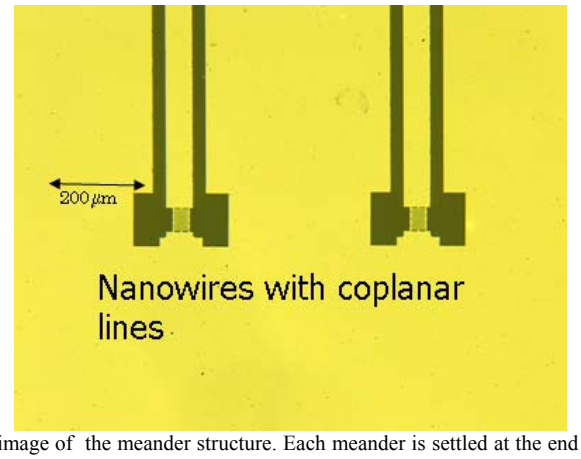


**Fig. 4.19** Microscopy image of the meander structure. Each meander is settled at the end of a balanced strip line for radio-frequency readout.

Meander structures have been patterned at the end of a planar wave-guide by 50Ω characteristic impedance (see Fig. 4.19): this feature is very important to achieve an optimal coupling between the detectors and the readout cable since the whole electronics operates at high frequencies. A common ground plate and further contacting pads realized sputtering NiCu by a proper mask on the last part of the lines allowed easy bonding by aluminium wires.

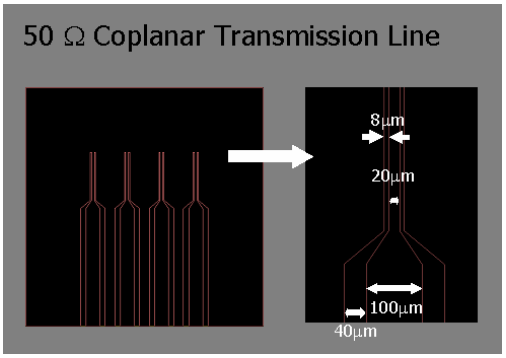


**Fig. 4.20** Particular of masks disegned at CAD to realize coupled 50Ω co-planar strip-line.

The patterning procedure is realized by Electron Beam Lithography. The pattern generator is realized by proper software and uses 10KV acceleration voltage within a low vacuum system ($P=10^{-4}$ torr). After about 90 minutes exposition the sample is ready to be developed. The etching has been realized by Reactive Ion Etching in $CF_4$+Ar in order to remove the excess bilayer. A second step of photoresist spinning and normal photolithographic procedure (exposition at UV lamps through a Cr mask) is used to define NiCu bulk contacts by lift-off procedure [81].

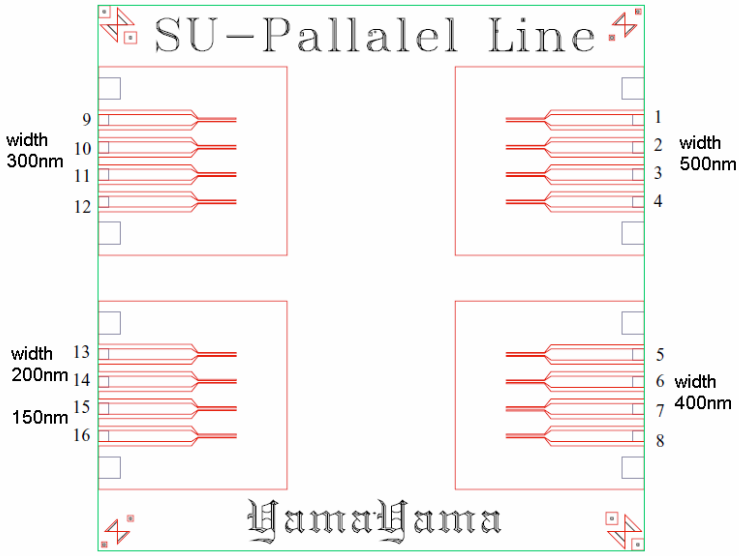


**Fig. 4.21** CAD design of main patterns and meander disposition on the sample.

References:

[76] S. Sze, Dispositivi a semiconduttore: comportamento fisico e tecnologia (Hoepli, Milano, 1995);
[79] A.Angrisani Armenio et alter,Phys. Rev. B 76, 024515, 2007
[80] M.Ejrnaes et alter,APL 95,132503, 2009
[81] Nicola Marrocco, Master Deg. Thesis, Realizzazione e caratterizzazione di dispositivi a giunzione tunnel con materiali superconduttivi non convenzionali, Univ. of Naples – Federico II,2003

**Not referenced**
[a] A. Barone, G. Paternò, *Pyisics and application of the Josephson effect* (Wiley, New York, 1981);
[b] L. Parlato, Master Degree Thesis in Physics*: "Sviluppo di una tecnologia di fabbricazione di Giunzioni Tunnel Josephson totalmente Refrattarie"*, (Università degli Studi di Napoli, 1992);

# 5. Experimental methods

The following chapter presents all experimental apparatus used for optical characterization and photoresponse experiments including cryogenic systems, optical tables arrangements, together with laser equipments, electronics, etc.. Measurements have been performed at the University of Rochester NY , the CNR-INFM Coherentia laboratories in Naples and CNR laboratories in Pozzuoli.

## 5.1 The cryogenic apparatus

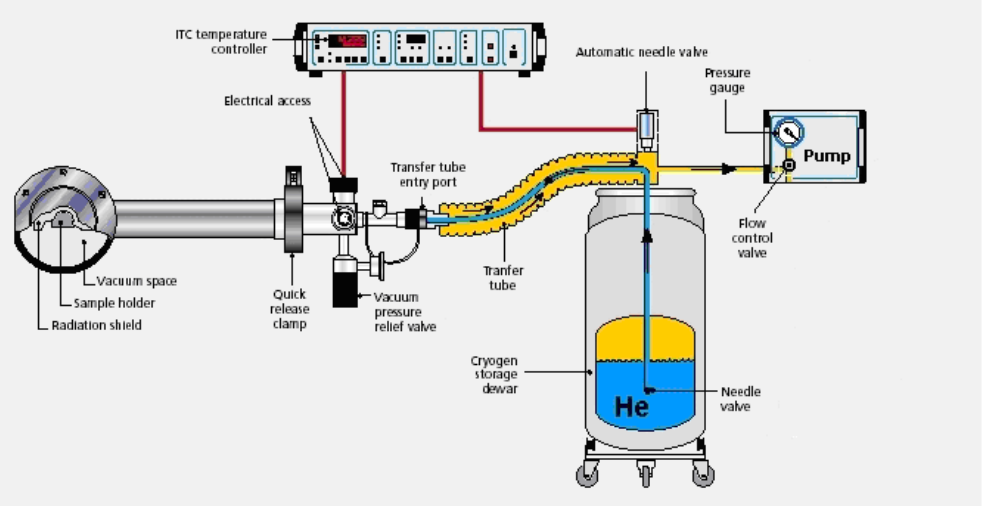


**Fig.5.1** working scheme

Fig. 5.1 shows the working principle of the cryo-system: used to cool down the cold finger in a He-flow cryostat. A medium-high vacuum evacuation ($P \approx 10^{-6}$ torr), reachable by diffusive or turbo-molecular pump is required to low the pressure in the cryostat vacuum chamber. Then, the liquid helium is transferred to the cryostat through a transfer tube, which is insulated at $P<10^{-5}$Torr with respect environment. The flow is controlled by a spin-valve and by a rotary-pump. Temperature is measured by a proper electronics able to directly power an heater connected to the cold finger, where a thermometer is positioned to feedback the loop control. Moreover, the feedback line is connected also to a step motor control of the spin valve.

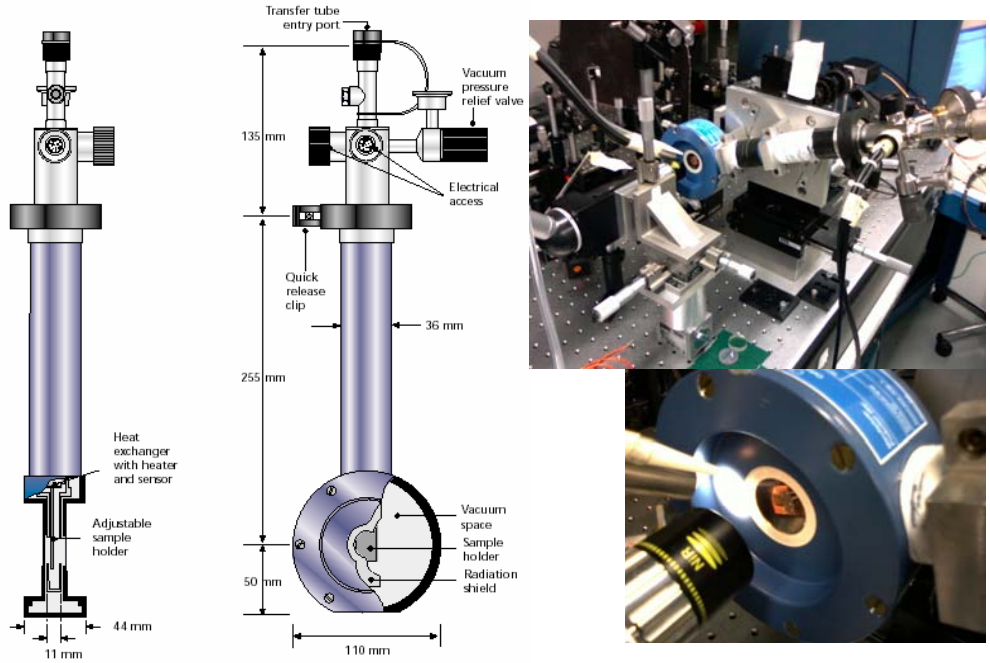


**Fig. 5.2** The cryostat: on the right particulars of the optical windows; a continuos argon gas flow at room temp by pipeline nearby evoids misting of the optical window (see the up-right image.

Fig 5.2 shows the Oxford MicrostatHe used at LLE – Rochester labs. The structure and working principles is nearly the same of Oxford Microstat Hires II used in MSA lab, Naples (see Fig. 5.3): the main differences are the loading arrangement, i.e. by an insert stick and directly on the cold finger accessible by unscrewing the optical window, respectively.

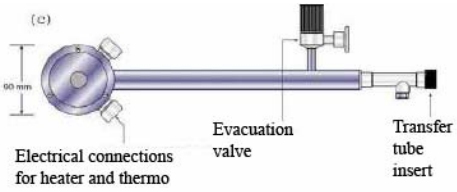


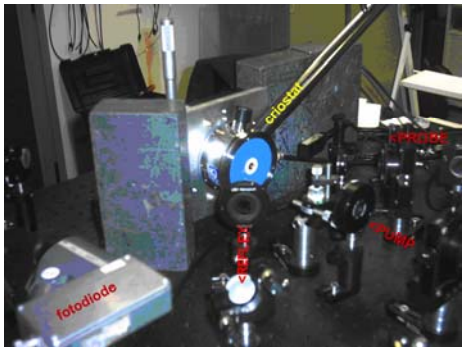


**Fig. 5.3** Oxford Microstat Hires II; on the right, the cryostat mounted on the optical table in MSA labs for Pump & Probe measurement (see below).

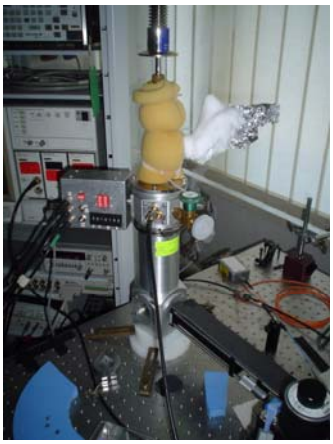

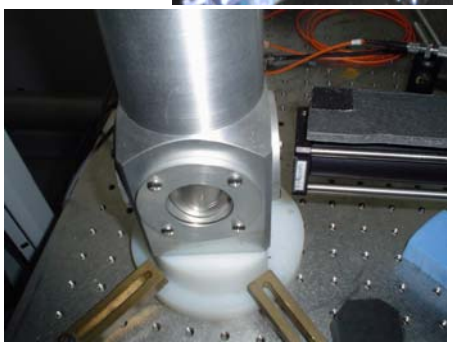

**Fig 5.4** The CNR – Pozzuoli cryostat ; on the right a particular view of the optical windows.

## 5.1 The laser equipments

The laser system consists of two units: an oscillator Ti-sapphire (Spectra Physics, Model Tsunami) powered by a pump system (Spectra Physics, Model Millennia). The Millennia is a continuous laser Nd:YVO4 optically pumped by two bars of laser diodes fiber optics linked. Within its cavity, a duplicating crystal (made by lithium triborate) allows light beam to reach a wavelength λ=532nm and 5.5W power. The obtained beam enters the oscillator to invert the polarization of active medium inside. Active media is an $Al_2O_3$ matrix doped by $Ti_2O_3$ for substituting $Al_3^+$ ions with $Ti_3^+$. In this way, by coupling the vibrational energetic levels within the crystal together with the ones of Ti ions, a band emission and a band absorption enlargement is achieved .

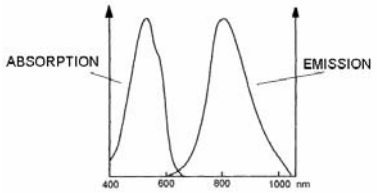


**Fig. 5.5** Ti:Sapphire Spectra

As Fig. 5.5 shows , laser emission occurs only for λ>670nm over the overlapping region of the two spectra. Out of the oscillator light pulses presents 720nm<λ<850nm and by means of both active and passive mode locking contemporary used, they achieve 100fs duration in time. Briefly, within a laser cavity, more longitudinal modes can oscillate without phase relation and with different magnitudes and frequencies: such electromagnetic waves produces several light peaks due to multi-mode interference, with varying magnitudes and randomly time departed. Active mode locking occurs when the phases of several modes are locked together by means of a variation of cavity leakages at a frequency equal to the separation between the longitudinal modes to obtain light pulses with time duration equal to the inverse of total length of gain curve and departed by a double cavity transit time. Modulation is entrusted to an opto-acoustic modulator externally driven. This technique allows to obtain pulses of 1ns duration. Passive mode locking is based on the usage of a non-linear mean (Ti:sapphire crystal) that produces differentiated losses for the different parts of the Gaussian beam walking into the cavity (see Fig. 5.5). Ti:sapphire crystal shows a refraction index *n* depending on the beam intensity hitting on it (by Kerr

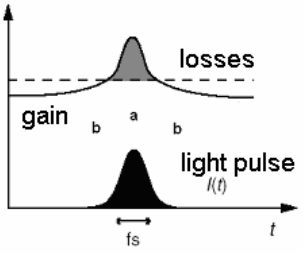


**Fig. 5.5** Profile of laser pulses

effect), so the active mean behaves as a converging lens major intensity peaks are transversally reduced in space thus decreasing their losses within the cavity respect to lower intensity peaks occupying a larger volume. Peripheral zones of the beam are so attenuated.

The COHERENT – MIRA laser at the Rochester University supply up to 10 W beam by a steady 30μm spot, tunable in frequency. Fig. 5.6 C shows the mode locking equipment .


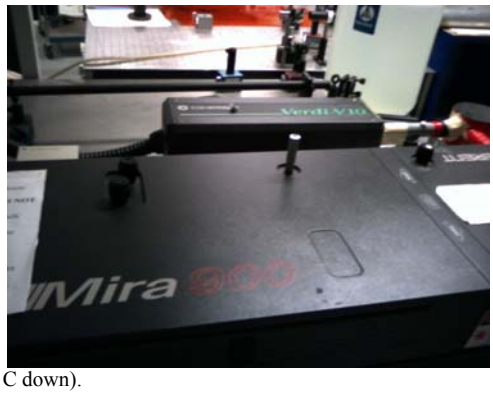


**Fig 5.6:** the laser equipment in Rochester (A left, B right, C down).

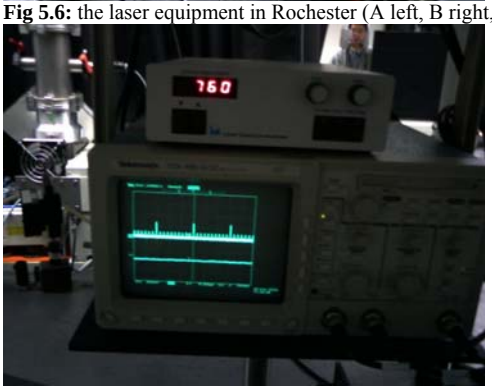

## 5.3 Pump and Probe experimental setup

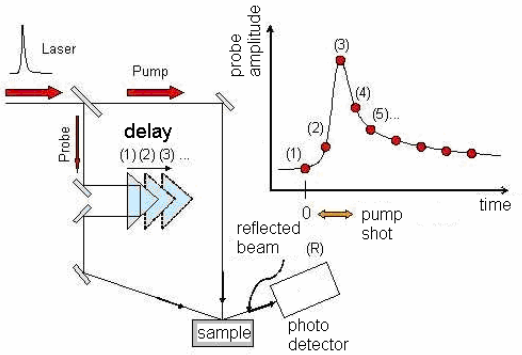


**Fig. 5.6** Pump & Probe optical setup outline.

The Pump & Probe is a spectroscopical technique time-resolved capable to reach resolution well under the picosecond using ultrafast laser sources. Two pulses comes from the same source : the pump, by higher power, locally excites the material (inside the beam spot and according to the optical penetration depth of the material under test); the probe, delayed respect to the probe, by lower power (10 to 20 times less) samples the excites region. The pump shot creates a non equilibrium condition and the hot-electrons, by *e-e* scattering interactions, take the system to a temperature, *Te*, decaying in time. The events here hinted are totally similar to the non equilibrium processes described in chapter one . The temperature changing produces the changing in reflectivity and transmissivity of the material, revealed by probe pulse "inspection" delayed from pump excitation by a controllable time interval. Repeating the test on different delay intervals, is thus possible to reconstruct in time dynamics of relaxing processes of electron and phonon systems.

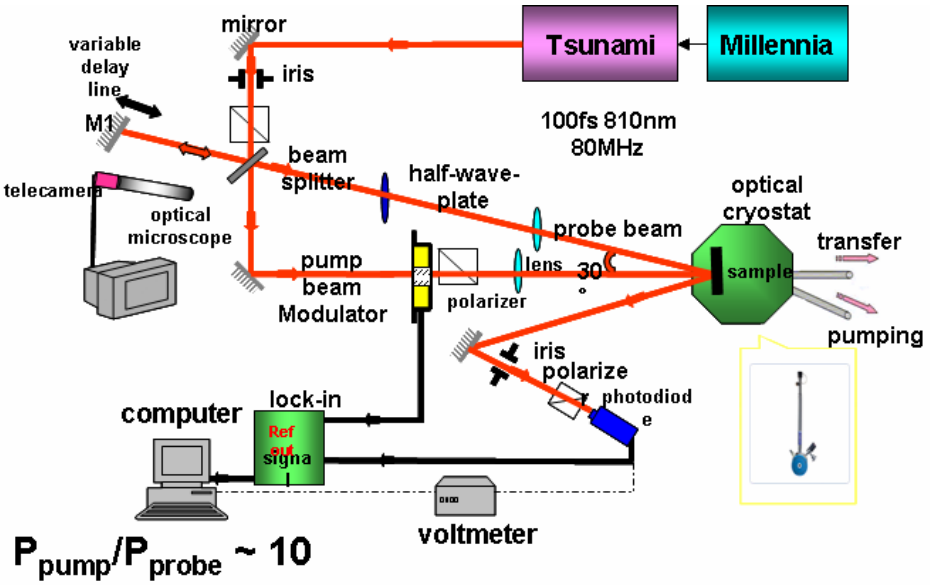


**Fig. 5.6** Pump & Probe optical setup.

The experimental setup is sketched in Fig. 5.6. Pump and probe beams are splitted by a beam splitter, then they hit the sample under different angles. A variable delay line is realized causing the light walk across prisms fixed on a motor controlled shifter . Generally the probe amplitude beam presents smaller amplitudes so it's fundamental to realize a low noise arrangement both for optical system and readout electronics as well. To achieve a high SNR (signal to noise ratio), excitation beam is modulated by a acousto-optic modulator at frequencies in the white region noise spectrum. Since the fundamental noise source of the system is the laser noise proportional to *1/f*, modulation frequencies are chosen to be in the range few Khz up to 100KHz. Output signal from a photodiode detector is sent to a lock-in amplifier able to read signal characteristics at the same frequency of the modulator also acting as notch or band-pass filter. To improve noise immunity and cut-off the slow fluctuations occurring during the measurement, a signal normalization is introduced as

$$I_R(\nu) = \frac{I(\nu) - I_0(\nu)}{I_0(\nu)}$$

where $I(\nu)$ is the intensity of readout probe signal when the pump beam excites the sample and $I_0(\nu)$ is the probe background (no pump beam). $I_R$ will be indicated in the following as $\Delta R$ .

When relaxing processes can be represented by a single exponential function and the corresponding decay time, namely $\tau$, is long if compared to pulses duty, $\tau$ can be estimated by means of a fitting procedure of the reflectivity signal. Signal must be taken out of the overlapping region (in space) of the pulses, in order to avoid spurious interference phenomena (named coherent artifacts) which are independent on relaxation dynamics. This problem is solved using for the two beams perpendicular polarizations.

Light pulse coming from laser, with a time duration of about 100fs, repetition rate 82MHz, and wavelength 810 nm walks through a polarization cube transmitting the horizontal polarized radiation, and reflecting the vertical one. Before reaching the cube, a $\lambda/2$ foil intercepts the laser thus allowing the ratio regulation of the beams powers. The pump beam goes through the acousto-optic modulator (IntraAction Corp model AOM-402A3) and it's reflected by a mirror, and sent to the prism of a manual delay line, useful to find the "zero position". Before, the pump goes through another polarization cube: the vertical component, reflected, goes to the photodiode to read modulation percentage, the vertical one, is transmitted to a focus lens well suited to three-dimensional arrangements to optimize the spot on the sample and the superposition with the probe one. The probe beam, from the first polarizer, goes to the polarizer cube on the step-motor delay line, computer controlled, with a resolution of 6.6 fs in time. The probe beam is also taken through mirrors to an adjustable in space focal lens to optimize the probe beam on the sample. The probe beam, reflected from the sample, is collected by a second photodiode (New Focus model

1801) whose output is connected to a lock-in amplifier (EG&G Instrument model 7260) , which also provides the reference signal at 200KHz for the modulator.

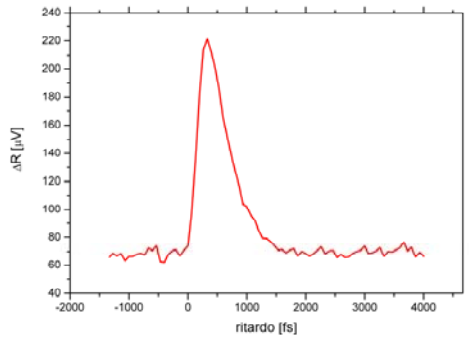


**Fig. 5.7** Reflectivity changes in a GaAs sample used as reference.

Fig 5.7 shows a typical reflectivity changes on a gallium-arsenide (GaAs) crystal used as reference for its quite clear response of 1ps width at room temperature.
The hypothesis to simulate the above signal only with a rising exponential and only a falling one seems not correct if we notice that real reflectivity curves shows a double slope in the fall that induces to model such a behaviour by a double exponential decay function. The two slopes are physically related to a fast electro-phonon scattering and a slower phonon dynamics.
A typical fitting curve used in data analysis is [82]:

$$\Theta(t-t_0)*\left(1-\exp\left(\frac{t-t_0}{\tau_S}\right)\right)-\Theta(t-(t_0+2\tau_D))*\left(1-\exp\left(\frac{t-(t_0+2\tau_D)}{\tau_D}\right)\right)$$

where $\Theta$ is the step function, the first exp is the rising part of the curve, the second is the decay side, $t_0$ the time-0 reference (see Fig. 5.8).

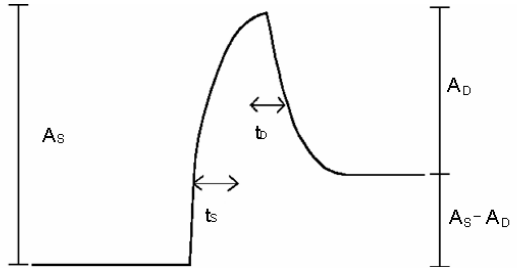


**Fit. 5.8** bi-exponential finning curve

The previous formula referable to falling slope, can be better expressed in a more complex way:

$$Y(t)=Y_0+C(1-C_1-C_2)\frac{1+\operatorname{erf}\left[\frac{\alpha(t-t_0)}{\Delta t}\right]}{2}-C\frac{1+\operatorname{erf}\left[\frac{\alpha(t-t_0)}{\Delta t}-\frac{\Delta t}{2\alpha\tau_0}\right]}{2}e^{\left(\frac{\Delta t}{2\alpha\tau_0}\right)^2-\frac{(t-t_0)}{\tau_0}}+$$
$$CC_1\frac{1+\operatorname{erf}\left[\frac{\alpha(t-t_0)}{\Delta t}-\frac{\Delta t}{2\alpha\tau_1}\right]}{2}e^{\left(\frac{\Delta t}{2\alpha\tau_1}\right)^2-\frac{(t-t_0)}{\tau_1}}+CC_2\frac{1+\operatorname{erf}\left[\frac{\alpha(t-t_0)}{\Delta t}-\frac{\Delta t}{2\alpha\tau_2}\right]}{2}e^{\left(\frac{\Delta t}{2\alpha\tau_2}\right)^2-\frac{(t-t_0)}{\tau_2}}$$

Where $Y_0$ is mean value for $t_0<0$ ,C is peck amplitude,C1,C2 relative (to C) amplitudes of secondary pecks,$t_0$ is the start-time at which pulse arrives , $\Delta t$ is the first peck duration, $\tau 0$ is the rising time,$\tau 1$ and $\tau 2$ are respectively the fast and slow falling times.

In Fig. 5.9 a reflectivity change curve obtained in the case of a Nb thin film (100nm) is shown: the aforementioned fitting curve can be adapted to exterimental responese, and thje result of the fittin are $\tau_1 \cong 0.6$ ps e $\tau_2 \cong 4.2$ ps

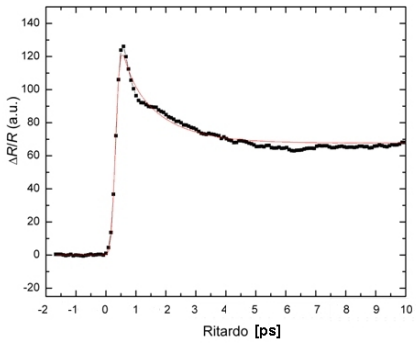


**Fig. 5.9** Experimental reflectivity change vs delay time for a thin film of Nb (100nm) deposited on a Si substrate sample : from fitting procedure $\tau_1 \cong 0.6$ ps e $\tau_2 \cong 4.2$ ps

## 5.4 Transient photoimpedance setup

The set-up of the photoimpedance measurement represents another important experimental aspect of this thesis. A schematics is showed in Fig. 5.10.

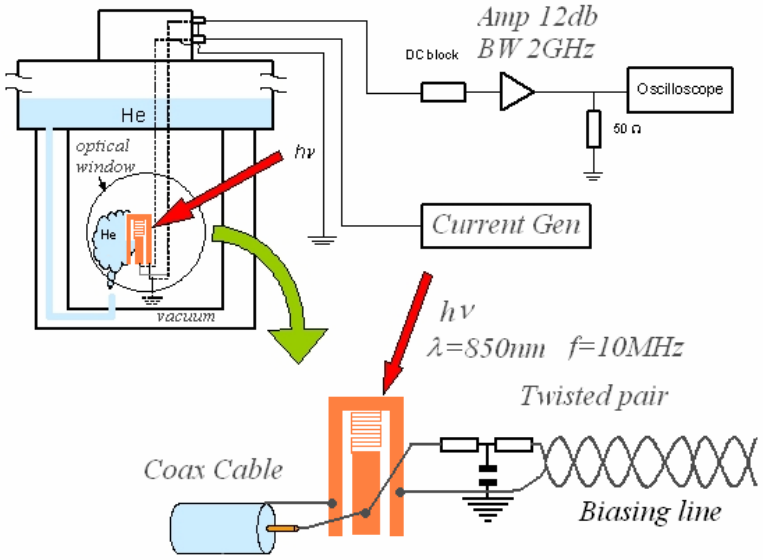


**Fig. 5.10** Photoimpedance measurement setup.

The DUT (Device Under Test) is cooled into a proper cryostat (see Section 5.1) at T<Tc By external sources the DUT is dc current biased at I<Ic and at temperatures close to Tc: this biasing procedure benefits from the recording of current voltage curves (IVCs) by suitable electronics. Noise due to spurious high frequency signals is strongly reduced by inserting a T type filtering, RC low pass and symmetrical: such a filtering stage prevents spikes to reach the DUT, and also the "switching events" from DUT to reach the biasing source stage. Switching events from synchronous laser pulses are detected by a RF coaxial cable connecting the readout room temperature front-end electronics. The latter consists of low noise and high gain RF amplifiers, ac coupled to avoid the continuous component from biasing line, and time recording systems (e.g. oscilloscopes).

A single coax cable connected from the DUT to room environment is used, passing by a bias tee in which the RF component is blocked by a coil that only allow the DC biasing while a condenser between DUT and room temp electronics allows dynamic signals to be carried along. RF cables are commercially available products by 50Ω characteristic impedance and several GHz band pass drop out.

**Fig. 5.11 LeCroy Oscilloscope, full digital, 9GHz cutting frequency.**

**Fig. 5.12** Particular of the amplifier stage (left); the waveform generator HP81104A (right).

A few specifications on ZFL-100LN+ used as signal amplifier, cascadable and often connected in pair to achieve higher gains (from G=20 of a single stage, to 400 for two cascaded amplifiers).

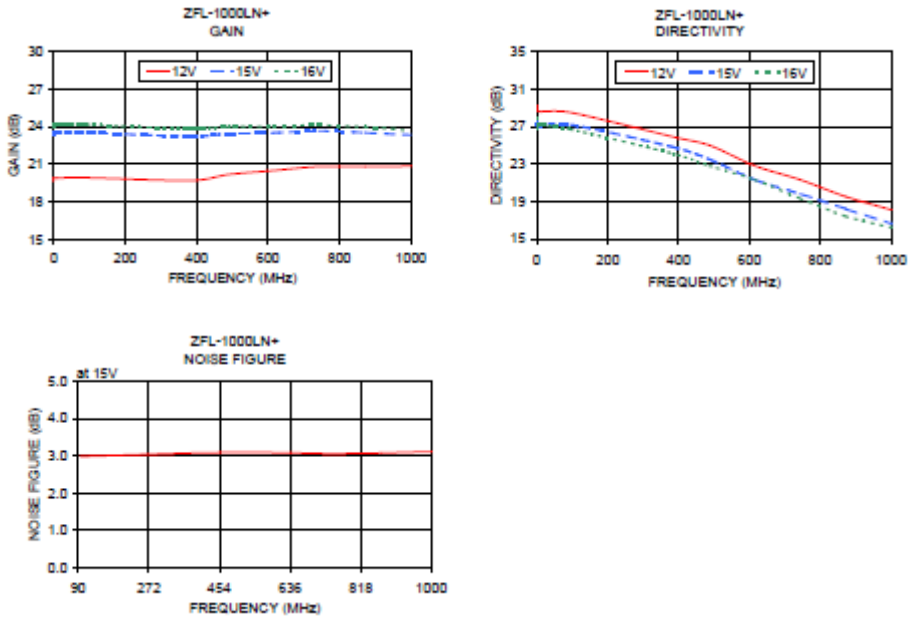


The ZFL-100LN+ shows a flat gain over all frequencies up to 1GHz, the band upper-limit. The directivity graph confirms that the amplified signal doesn't influence the amplifier input in terms of noise. The noise figure, defined as the ratio between output power signal (when the amplifier is considered as noisy) and the same power output signal but now considering the amplifier in the ideal case (no noise). HP pulse and pattern generator Mod HP81104A has been used to modulate the laser diode used to drive light on the samples.

## 5.5 Laser source fluence calculation

During photoresponse measurements two diode laser sources characterized by low powers but easy modulation up to 80MHz have been used. Three main frequencies, i.e. 5MHz, 10MHz and 20MHz as well as both 6.5ns or 20ns duty pulses have been used. An important parameter for photoresponse measurements is represented by the fluence, that is the time averaged energy per unit surface. In our experiments, in the case of a wavelength $\lambda$=1550nm, continuous laser power 1mW, spot area $1.43*10^{-4}$ $cm^2$, repetition rate 10MHz and laser pulses duty: d = 6.5ns, we found $\Phi=4.5x10^{-8}$ $J/cm^2$ , or $\Phi=3x10^{-8}$ $J/cm^2$ if the beam, before hitting the sample, was attenuated in power by a 3dB full-band-pass optical filter.
In the case of a wavelength $\lambda$=850nm, continuous laser power 1mW, spot area $1*10^{-6}$ $cm^2$, repetition rate 10MHz and laser pulses duty: d = 6.5ns, we found $\Phi=4.5x10^{-8}$ $J/cm^2$ , or $\Phi=1x10^{-10}$ $J/cm^2$ , corresponding to hitting 500 photons.

References:

[82] Vito Pagliarulo, Master Deg. Thesis, Univ. Degli Studi di Napoli – Federico II,2004

# 6. Transient reflectivity measurements

This chapter presents experimental results in terms of time resolved optical reflectivity change performed on both thin films of pure low Tc superconductors and proximized bilayers containing such superconductors as base films. The optical investigation is able to produce useful information about the energy relaxation times involved in the cascade to restore thermodynamic equilibrium inside the perturbed superconductor by investigating the optical reflectivity and its link to nonequilibrium electron distribution function. The analysis approach will be mainly related to the possibility to model this stage pf the energy cascade by defining two temperatures for the out-of-equilibrium electron and phonon populations. Part of the experimental results discussed in this section have been already published during the doctorate activity or submitted for publication.

## 6.1 Pump and Probe spectroscopy over thin films

In the following paragraphs, a series of measurements performed on pure superconducting Nb and NbN, normal NiCu thin films as well as on proximized bilayers containing the aforementioned superconductors as base thin film will be reported. The aim of this experiments was mainly that of reaching a more complete knowledge about nonequilibrium scattering processes involved in relaxation phenomena after laser absorption..

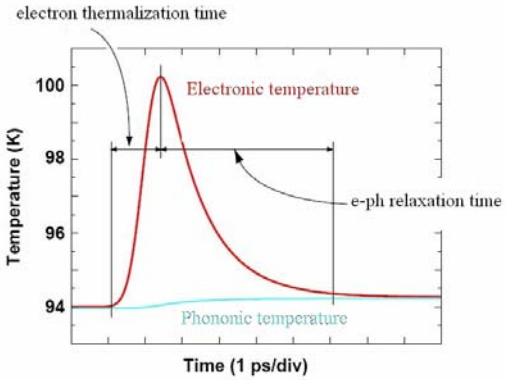


**Fig. 6.1** Sketch of electronic and phononic populations thermal evolution for an out-of-equilibrium metal [available in literature]

It has been shown how the 2T model [see Sect. 2.2.1] can describe the time dependence of the temperatures defined for both electrons (e) and phonons (ph) within a metal when an external perturbation starts a time-varying transitory in which energy exchanges prevail up to restoring the initial equilibrium.
Fig. 6.1 sketches the typical temperature trend according to the proposed model. Because of the differences in specific heats for el and ph, the time evolution will end showing an overall increase of the temperatures when they converge to a common value out-of-equilibrium: the energy absorbed by the metal, after some losses due to the phonon escape to the substrate, produces the overall change of temperature $\Delta T$. While the ultra-fast excitation absorption by electrons involves timescales of ps order and can be undoubtedly related to the first arising slope on the Fig. 6.1, the relaxation process starts first involving the (e)-(e) scattering which produces a fast thermalization, followed by an (e)-(ph) interaction phase, slower. These two phenomena can be directly observed in $\Delta R$ evaluation because the falling part of the curve sometimes can present a double slope. This induces to fit the curves using a normal bi-exponential curve function of two time constants, referred to as $\tau_1$ and $\tau_2$ or $\tau_{fast}$ and $\tau_{slow}$.

By using a 2-temperature model and considering that in general the lattice specific heat is significantly greater than the electronic specific heat ($C_l > C_e$) the absorbed energy produces out of equilibrium electrons in a faster way than the lattice excitation: this is the reason why short pulses act only on (e) population. So these “hot electrons” reach a higher temperature than the lattice. The change either in reflectivity or transmissivity, later monitored by the delayed probe pulse, can be related to the change in electron and lattice temperature. Indeed, the reflectivity in a metal can be written as:

$$|R|^2 = \frac{c\,\mu_o}{2}\frac{[1-\mathrm{Re}\,(n)]^2+[\mathrm{Im}\,(n)]^2}{[1+\mathrm{Re}\,(n)]^2+[\mathrm{Im}\,(n)]^2} \qquad (6.1)$$

where n is related to the dielectric function $\varepsilon_r$ and in a metal $\varepsilon_r - 1 \cong \frac{i\sigma}{\varepsilon_0 \omega}$ with σ is the conducibility that in Drude model [Ashcroft,[83]] can be approximated with $\frac{ne^2}{m}\tau(E)$. Considering that $n = (1+i)\sqrt{\frac{\sigma}{2\varepsilon_0\omega}}$ in the non equilibrium regime induced for example by a laser beam, the reflectivity change can be written as:

$$\Delta R = \frac{dR}{d\sigma}\Delta\sigma = \frac{dR}{d\sigma}\left(\frac{d\sigma}{dn}\frac{dn}{dT_e}\Delta T_e + \frac{d\sigma}{d\tau}\frac{d\tau}{dT_L}\Delta T_L + \ldots\right) \qquad (6.2)$$

Therefore, the transient reflectivity (or transmission) change can allow us to estimate the temperature time evolution of a metal inner subsystems of (e) and (ph). The choice of manufacturing thin films and bilayers allows also to cause the light excitation to reach the inner layers of crystal lattice or of any amorphous deposited material. The capability to excite interfaces of bilayers, for example, can give useful information not only on their quality but mostly on their physical characteristics and transport properties.
To analize the behaviour of $T_c$ both within a superconductor and a proximized ferromagnetic layer, the theoretical model proposed by Fominov [[84]] has been used. Accordingly, it is possible to find a relation between the critical temperatures of the bilayer and the thickness of the ferromagnet layer, and then use the results of fitting to numerically simulate the electron density of states of the bilayer. Such a knowledge helped us to evaluate the electron heat capacity, and hence to check the 2T model results in this novel material context [[85],[86]].

The Fominov model assumes the condition, usually experimentally verified, of a "dirty" limit, which implies that the mean free path *L* in the layers is less the coherent lengths. According to the model, in the single-mode approximation, the critical temperature of a S/F bilayer is calculated through a linearized Usadel equation for the S and F layers, whose thickness will be indicated as $d_S$ and $d_F$, respectively:

$$\ln\frac{T_{cS}}{T_c} = \Psi\left(\frac{1}{2}+\frac{\Omega_2}{2}\frac{T_{cS}}{T_c}\right)-\Psi\left(\frac{1}{2}\right)$$

$$\Omega\tan\left(\Omega\frac{d_S}{\xi_S}\right) = W(\omega_n)$$

**where**

$$W(\omega_n) = \gamma\frac{A_s(\gamma_b+\mathrm{Re}\,B_f)+\gamma}{A_s|\gamma_b+B_f|^2+\gamma(\gamma_b+\mathrm{Re}\,B_f)},$$

$$A_s = k_s\xi_s\tanh(k_s d_s), \quad k_s = \frac{1}{\xi_s}\sqrt{\frac{\omega_n}{\pi T_{cs}}}.$$

and Ψ(x) is the digamma function, $T_{cS}$ the critical temperature of the single S layer. The physical properties of the S/F bilayer are described in terms of two parameters, named γ and $\gamma_B$ defined [see Section 3.1.2], defined as:

$$\gamma = \frac{\rho_S \xi_S}{\rho_F \xi_F} \qquad \gamma_B = \frac{R_B A}{\rho_F \xi_F}$$

where $\rho_{S(F)}$ is the normal state resistivity of the S(F) layer, $R_B$ and A are the resistance and the area of the S/F interface respectively, $\xi_S$ and $\xi_F$ are the superconducting and *ferromagnetic* coherence lengths, respectively, expressed as follows:

$$\xi_S = \sqrt{\frac{\hbar D_S}{2\pi k_B T_{cS}}} \qquad \xi_F = \sqrt{\frac{\hbar D_F}{2\pi k_B T_{cS}}}$$

where $D_S(F)$ is the diffusion coefficient of S (F). $\xi_S$ is related to the Ginzburg-Landau coherence length $\xi_0$, while $\xi_F$ is a measure of the diffusive motion of the Cooper pairs in the ferromagnet and should not be confused with $\xi_F^* = \sqrt{\frac{\hbar D_F}{E_{ex}}}$ which instead measures the decay and the oscillation length of the order parameter in F.
$\gamma$ is a measure of the strength of the proximity effect between S and F layers, whereas $\gamma_B$ describes the effect of the boundary transparency between them.

Using the above mentioned parameter, a numerical DoS simulation is possible. Starting from the simulated density of states, is then possible to calculate the specific heat to introduce into the 2T model.
By assuming the relation [87]

$$u = \int_{-\infty}^{\infty} d\varepsilon\, g(\varepsilon)\varepsilon f(\varepsilon) \tag{6.3}$$

where $u$ is the free energy $u$ and $g(\varepsilon)$ the density of states, and $f(\varepsilon)$ the Fermi distribution function, it is possible to calculate the electron specific heath as follows:

$$\left| c_v = \left(\frac{\partial u}{\partial T}\right)_n = \frac{\pi^2}{3} k_B{}^2 T g(\varepsilon_F) \right| \tag{6.4}$$

linking the specific capacity of an electron gas to $u$, using a software developed in Mathlab© Mathworks Inc., it has been possible evaluate (e) capacity of the 2T model staring from the $\gamma$,$\gamma_B$ and $E_{ex}$ of S-F bilayers. Must be noticed that the operative approach was first to consider the DoS dependant on T in a negligible way so the only derivative term becomes the Fermi distribution, second to take the derivative into the integral.

## 6.1 Nb and Nb/NiCu thin films

The first test of optical reflectivity measurements have been performed on both Nb and Nb/ $Ni_{0.48}Cu_{0.52}$ bilayers. Pump and probe beams power ratio was 10:1 and a laser fluence [1] of about 100 $\mu J/cm^2$ was used. The ferromagnetic coherence length was estimated to be $\xi_F$=24nm [88] while the optical penetration depth was measured to be $\alpha$ = 10.6 nm at 810-nm by measuring the optical transmittivities of different thicknesses of $Ni_{0.48}Cu_{0.52}$ films.

[1] laser fluence is the mean power density of the laser integrated in time.

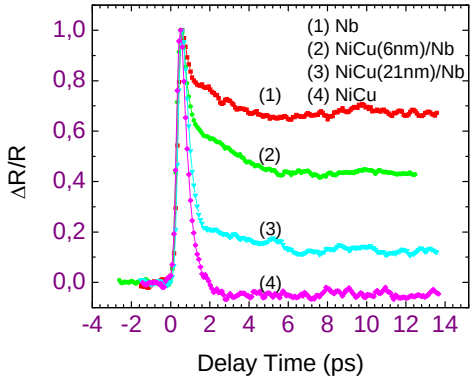


**Fig. 6.2** Normalized optical reflectivity on Nb and Nb/$Ni_{0.48}Cu_{0.52}$ samples at T=6K (left) .

Reflectivity change curves have been fitted by a two-exponential formula as previously explained obtaining a $\tau_{fast}$ sub picosecond in value which demonstrates the (e)-(ph) interaction. The $\tau_{slow}$ is of the order of picoseconds and reveals (e) inelastic interactions to acoustic (ph) and Cooper pairs recombination. The final part of the curves is related to the heat transfer to substrate by phonon escape.
It is important to notice that Nb response is mostly determined by the slow decay from phonon escape, while NiCu presents a sharp peak and almost no slow (ph) relaxation. On the other hand, the Nb/NiCu bilayers are positioned in the middle, and the slow interaction decreases as NiCu thickness increases.
Of course, the strong reduction of the "slow" recovery time makes the ferromagnetic action very attractive for fast detectors. No particular variation of $\tau_{fast}$ with temperature was recorded: it changes from 0.18 to 0.32 ps circa in the Nb/NiCu(21nm) bilayer within the range of few K, while at room temperature his values doubles. $\tau_{slow}$ time also varies 2.5 to 5.2 ps not substantially between temperatures from 3 to ≈7 K, also in the investigated Nb/NiCu(12nm) sample .

## 6.2 NbN and NbN/NiCu thin films

Let's consider now the results on NbN, that , nowadays, is the best material solution to realize ultra-fast and sensitive SPDs. The change of the critical temperature ($T_c$) and the residual resistivity ratio (RRR) as the film thickness was decreased from 100nm (bulk limit) down to 5 nm (of the same order of the NbN coherence length) have been investigated. For a 20nm thick film we obtained a $T_c$ of 13.6 K, a RRR at 20K larger than 1, and a resistivity $\rho_{NbN}$=133 μΩ cm at T= 20 K.

A NiCu overlayer ( 10nm <d< 50 nm) was deposited over the NbN films. The resistivity of a thin NiCu film was measured by using a four probe in-line technique, and found to be $\rho_{NiCu}$= 276 μΩ cm at T= 77 K. Low-temperature magnetization tests showed a Curie temperature of about 30 K and a spontaneous moment per atom $\mu_0$=0.06 μB/atom at T=4.2 A femtosecond pump–probe measurements were performed with a laser spot diameter of about 40 μm. Because the optical penetration depth at 810 nm wavelength for the $Ni_{0.48}Cu_{0.52}$ film was estimated to be about 11 nm, we tested bilayers with different thicknesses of F in order to investigate the proximity effect in this innovative superconducting system.

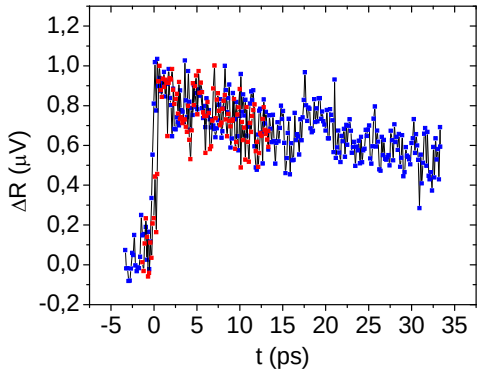


**Fig.6.1** Time resolved ΔR waveforms at T=5 K for two different bilayers: red points NbN(100nm)/NiCu(22nm), blue points NbN(100nm)/NiCu(38nm).

Differently with respect Nb based bilayers, NbN based bilayers showed a very slow decay time in the superconducting state of the whole bilayer independently on both NiCu or NbN thicknesses. This behaviour was in contrast with expected optical response for pure NbN, and observed behaviour in Nb-based proximized structures. Fig. 6.1 shows a typical transient reflectivity change of NbN-based bilayers at T=5K (see caption for details).

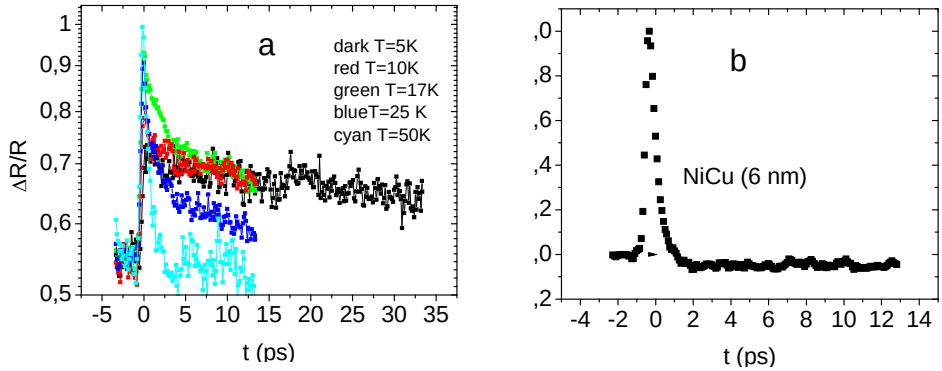


**Fig.6.2 (a)** Reflectivity measurement of an NbN(100nm)/NiCu(38 nm) bilayer at different temperatures. **(b)** comparison with simple NiCu layer.

In Fig. 6.2a the reflectivity change curves recorded at different temperatures are showed, while in Fig. 6.2b a transient curve of a pure NiCu thin film of thickness 6nm is plotted. The comparison clearly demonstrate that NiCu alone is again very fast in electron relaxation processes, but the proximity effect induces a slow relaxation of produced excitations (see curves at T<15K).

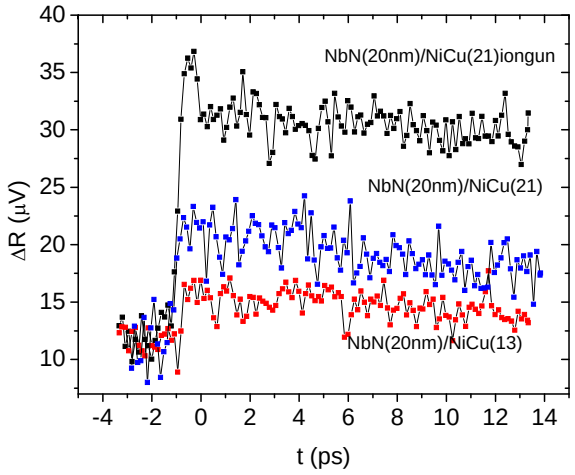


**Fig.6.3. Time resolved ΔR waveforms at T=7 K for different bilayers (NbN(20nm)/NiCu(21 nm) with surface cleaning dark points, NbN(20nm)/NiCu(21 nm) blue points, NbN(20nm)/NiCu(13 nm) red points.**

Moreover, the ΔR spectrum of the bilayers NbN(100nm)/NiCu(21nm) is quite similar to sole NiCu layer (relaxation time of 1ps).

A different behaviour is observed for a bilayer NbN (20nm)/NiCu(21 nm) where the surface of NbN was cleaned by a ion beam (Ar pressure $\approx 10^{-3}$ Pa **,**etching rate of about 0.2 nm/s) (Fig. 6.3). The reflectivity transient initially exhibits a very sharp peak, approximately t=800fs in duration, and probably related to a fast electron-phonon interaction. The cleaning process probably acts on the transparency of the interface making decoupled the dynamics of electron and phonon temperatures.

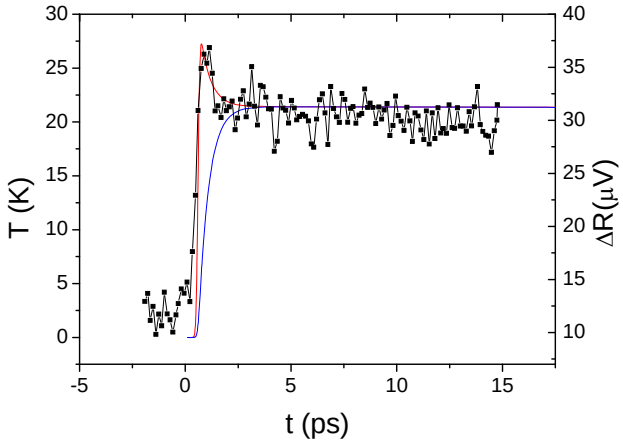


**Fig.6.4** Normalized reflectivity change as a function of time (solid point), measured a T=7 K for a NbN(20 nm)/NiCu(21nm) bilayer. The red and the blue solid lines are the electron and phonon temperatures respectively, numerically simulated by using the 2T model.

Using a 2T model approach, we obtain the best fits presented in Fig. 6.4 by assuming $C_e$=1.5 mJ/(cm$^3$K) and $C_{ph}$= 0.6 mJ/(cm$^3$K), and $\tau_{e\text{-}ph}$= 1.6 ps. Moreover, in the numerical simulation we found $\tau_{esc}$=0.16 ns, and the experimental values for the laser pulse duration $t_0$= 100 fs at a working temperature $T_0$=7 K and a critical temperature of the bilayer $T_c$=13.6 K. The ratio $C_{ph}/C_e$ = 0.4 as estimated in our samples NbN(20nm)/NiCu(21nm) is about one order of magnitude smaller than the ratio reported in literature for a pure NbN film 20 nm thick ($C_{ph}/C_e$=3.8 [89] ). This behaviour is totally opposite to the case of bilayer Nb/NiCu and pure films of Nb where we estimated a value of $C_{ph}/C_e$ equal to 6.4 and 2.7 for Nb/NiCu and Nb samples, respectively [90]. In Table 6.1 the values of the specific heats for different samples are reported.

| Sample | $C_e$ (mJ/Kcm$^3$) | $C_{ph}$ (mJ/Kcm$^3$) |
|---|---|---|
| Nb(100 nm) | 3.48 | 9.4 |
| Nb(70nm)/NiCu(21nm) | 1.54 | 9.86 |
| NbN(20 nm) | 1.3 | 3.8 |
| NbN(20nm)/NiCu(21nm) | 1.6 | 0.6 |

**Table 6.1**

By comparing the $C_e$ and $C_{ph}$ sets of values for different samples, we observe that the presence of the NiCu film in bilayer Nb/NiCu only marginally influences the phonon subsystem while a significant decreasing in $C_e$ affects the electron subsystem cooling that is the dominant mechanism in the non equilibrium relaxation processes in the bilayer ($\tau_{e\text{-}ph}/\tau_{ph\text{-}e}$ <<1). Instead, in the bilayer NbN/NiCu the overlayer F seems to act as a trap of the phonons that can break other Cooper pairs producing other excitations ($\tau_{e\text{-}ph}/\tau_{ph\text{-}e}$ >1). In other words, there is a large backflow of the phonons from to the phonon system to the electron system that not relaxes their energy fast.

By using the Fominov model described in paragraph 1, we have fitted our experimental data of the critical temperatures of the bilayer $T_{cS}$ as function of the thickness of the NiCu layer (Fig. 6.5)

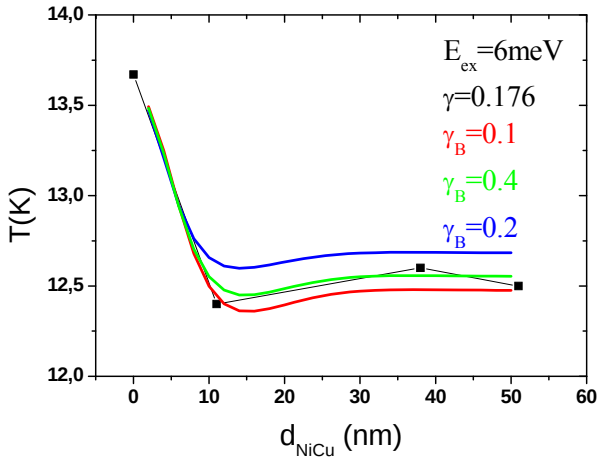


**Fig.6.5**. Superconducting critical temperatures for NbN/NiCu bilayers as a function of $d_{NiCu}$. Different lines (red, green, blue) are the results of the theoretical fit for different values of $\gamma_B$ and for $E_{ex}$= 6 meV, $\gamma$=0.176.

The result of the best theoretical fit was obtained for the following parameters: $E_{ex}$= 6meV, $\gamma$=0.176, $\gamma_B$=0.2. These results are different from other $Nb/Ni_{0.48}Cu_{0.52}$ and $Nb/Ni_{0.54}Cu_{0.48}$ [91], $Nb/Pd_{0.86}Ni_{0.14}$ [92] bilayers. In the last two bilayers a higher value of the $E_{ex}$ (12 meV) was reported, may be due to an increase of the ferromagnetism in the alloy and a higher interface transparency ($\gamma_B$=1.5 and 0.6, respectively) probably due to a different growth of the alloy over the superconducting film without vacuum breaking. If we compare the behaviour of the bilayers $NbN/Ni_{0.52}Cu_{0.48}$ and $Nb/Ni_{0.52}Cu_{0.48,}$ fabricated in the same conditions, we observe a lower transparency of the interface in the first bilayer.

The knowledge of the parameters at the interface allows, according to the proximity model for the F/S bilayer proposed in the first paragraph, to numerically calculate the energy dependence of the local Density of States N(E) at any position with respect to the F/S interface, as well as on both sides of the bilayer (see Fig.6.6).

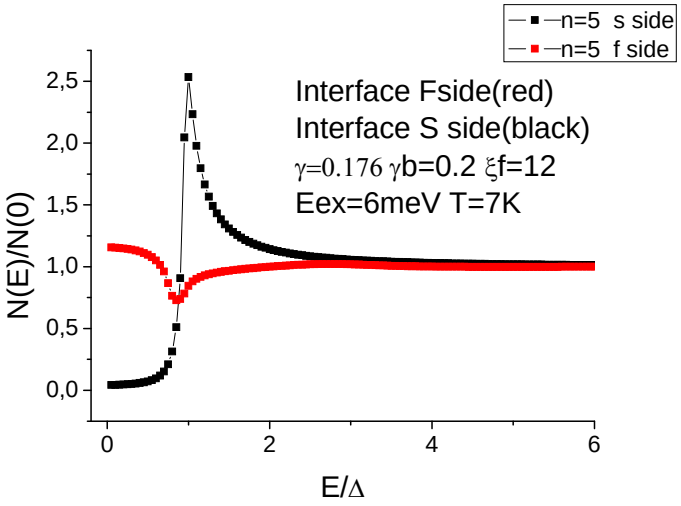


**Fig. 6.6.** Density of States versus the normalized energy, calculated based on the S/F proximity theory for NbN(20nm)/NiCu(21nm) bilayers at T/Tc=0.61 at the interface into the S layer (dark curve) and F layer (red curve).

The resulting electron heat capacity has been found to be $C_e$= 1.5 mJ/cm$^3$ K at T= 7K, the same value estimated by using a 2T model justifying our proximity model for the bilayer NbN/NiCu and the validity of our hypothesis at the interface.

References:

[83] A.D.Semenov et alter, Trans. On Appl. Supercond.,Vol.7,N.2,1997
[84] Ya.Fominov,N.Chtchelkatchev,A.Golubov, Phys.Rev. B 66,014507 (2002)
[85] A.Angrisani Armenio et alter,Upper critical fields and interface transparency in superconductor/ferromagnet bilayers, Phys. Rev. B 76,024515,2007
[86] Nicola Marrocco, Master Deg. Thesis, Realizzazione e caratterizzazione di dispositivi a giunzione tunnel con materiali superconduttivi non convenzionali, Univ. of Naples – Federico II,2003
[87] Ashcroft/Mermin,Solid State Physics,Harcourt Publ.,1976,pag.44
[88] T.Taneda et alter, Time-resolved carrier dynamics and electron-phonon coupling strength in proximized weak ferromagnet-superconductor nanobilayers, PHYSICAL REVIEW B 75, 174507, 2007
[89] A.Semenov et alter , Supercond. Sci. Tech. 15,2002,R1-R16
[90] E.Ghershenzon et alter, Sov.Phys.JEPT59,442
[91] A.Angrisani Armenio,c.Cirillo,G.Iannone,S.Prishepa,C.Attanasio, PRB 76,024515,2007
[92] G.Iannone,D.Zola,..,C.Attanasio, PRB 75,064409,2007

# 7. Transient photoimpedance measurements

In this final chapter, dynamic photoimpedance measurements performed on various superconducting materials and configurations are presented. The measurements are not of single photon counting as the original research project aim. Nevertheless, they evidenced some interesting physical aspects concerning nonequilibrium superconductivity involved in micro- and nanowires also in presence of the proximity effect (see Chapt. 3). Further improvements of the measurement setups have been postponed to future activity with the aim to obtain a complete validation of some of the theoretical aspects addressed in the first chapters. The relevant parts of experimental results presented in this chapter have been published or submitted for publication on international journals..

## 7.1 Photoimpedance of Nb and Nb/NiCu meander shaped PD

The most significant result on Nb and Nb/$Ni_{0.48}Cu_{0.52}$ has been obtained on an "H" shaped device and presented in Fig. 7.1 : samples were prepared as described in Section X.Y. The H-shaped bridges were irradiated by using a 100fs laser source with a repetition rate of 76 MHz and wavelenght λ=810nm. A complete description of the experimental photoresponse apparatus has been presented in Section X.Y.

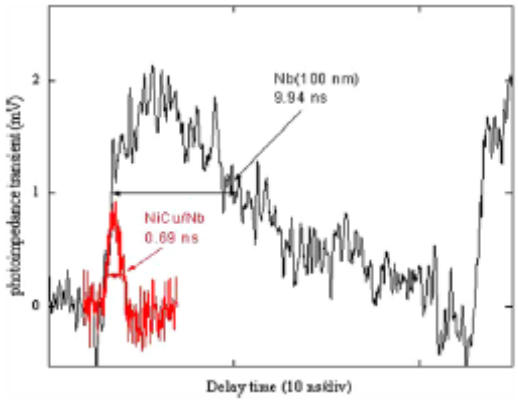


**Fig. 7.1 :** Experimental photoresponse transient of a pure Nb microbridge, recorded at 7 K with $I_b/I_C$ = 0.43, and of a NiCu/Nb microbridge at 6 K with $I_b/I_C$ = 0.43, illuminated at 225 μW and 7 μW average laser powers, respectively [93].

The photoimpedance measurement performed on both Nb and Nb/NiCu(12nm) bilayers is presented in Fig. 7.1. The presence of the overlay clearly give rise to a faster signal, even if reduced in amplitude, with a clear evidence of the inertia-like recovering of he superconducting pairs related to kinetic inductance (see further). The two measurements were performed in the almost same conditions, i.e. in particular the same ratio $I_{bias}/I_c$=0.43,diffenent laser power (7uW laser power for Nb/NiCu, 225uW for Nb), slightly different reduced temperatures (0.79 for Nb and 0.75 for the Nb/NiCu sample). In particular, the resulting FWHM of signals were 0.7ns and 9ns respectively for the bilayer and the superconductor only. We conclude that NiCu/Nb bilayer showed a dominance of electron subsystem in the nonequilibrium relaxation, as demonstrated by the kinetic inductive photoresponse [93], from which we get $L_{KIN}/R_L \approx 1$ ns, and $L_{KIN} \approx 50$ nH.

The presence of the overlayer significantly reduces the response time of the strip, and this can be an effective way for further decreasing the reset time of a Nb-based nanowire counter. Even if optical pump and probe experiments demonstrated picoseconds relaxation times in the energy down-conversion, the voltage photoresponse of films, opportunely biased in current, probes the conductivity change in a frequency range characterized by an overall response time that can be larger because of parasitic effect and lower band-pass of readout electronics. According to Ref. [94], outlet signals timings are determined not only by the (e)–(ph) relaxation times, but also by the phonon to electron heat capacity ratio, and the laser fluence. The experimental FWHM = 0.69 ns measured in the case of NiCu/Nb

microbridges is mostly due to our front end electronics limited value. The FWHM = 9.94 ns in the case of Nb is clearly demonstration of a thermal response, occurring inside the microstrip during the energy relaxation. Moreover, we estimated $C_p/C_e$=6 and 2 for NiCu/Nb and pure Nb, respectively starting from the 2T model and taking the timings from the response graph.

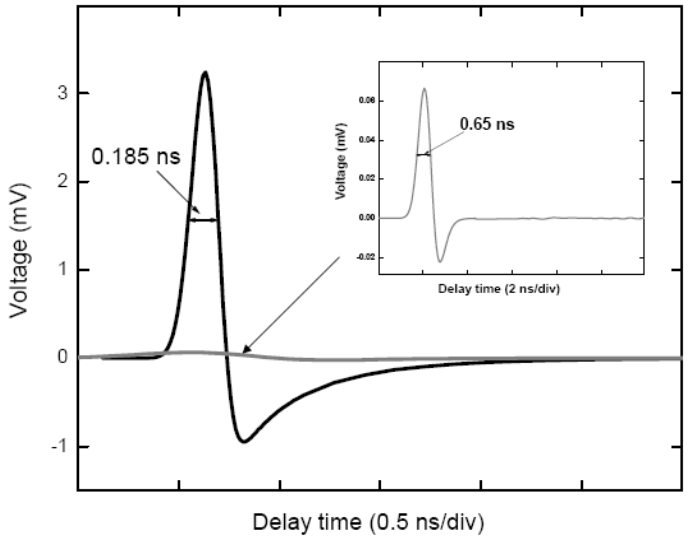


**Fig. 7.1 A** Numerical simulations of *V*kin as a function of time, obtained using the 2T-model solutions and Eqs. (below), for our NiCu/Nb (large oscillatory curve) and Nb (inset) samples.

As discussed in chapter 2.5.2, in Fig 7.1 A is reported the simulation of kinetic inductance modulation by laser pulse absorption. The evidence of inductance variation is enclosed into the undershoot that takes the voltage signal to reset.

## 7.2 NbN and NbN/NiCu superconducting nanowires: IV characterization

It is due to point out how a complete test on the samples has been conducted firstly performing the standard DC-IV curves acquisition. As expected, how the critical currents obtained seem to be related to devices' width of the stripes.

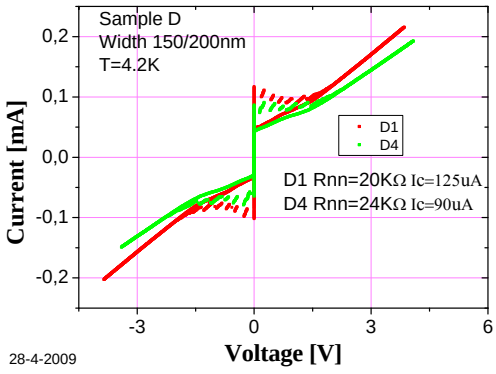


**Fig. 7.2** IV curves of a NbN(8nm)/NiCu(3nm) bylayer measured at T=4.2K on a meander shaped chip 6 series by 3 parallel bridges ; red curve refers to a bridge width=150nm structure, the green curve to a 200nm one. The 150nm meander shows an Ic=125$\mu$A and Rnn=20KΩ; the 200nm shows an Ic=90$\mu$A and Rnn=24KΩ .

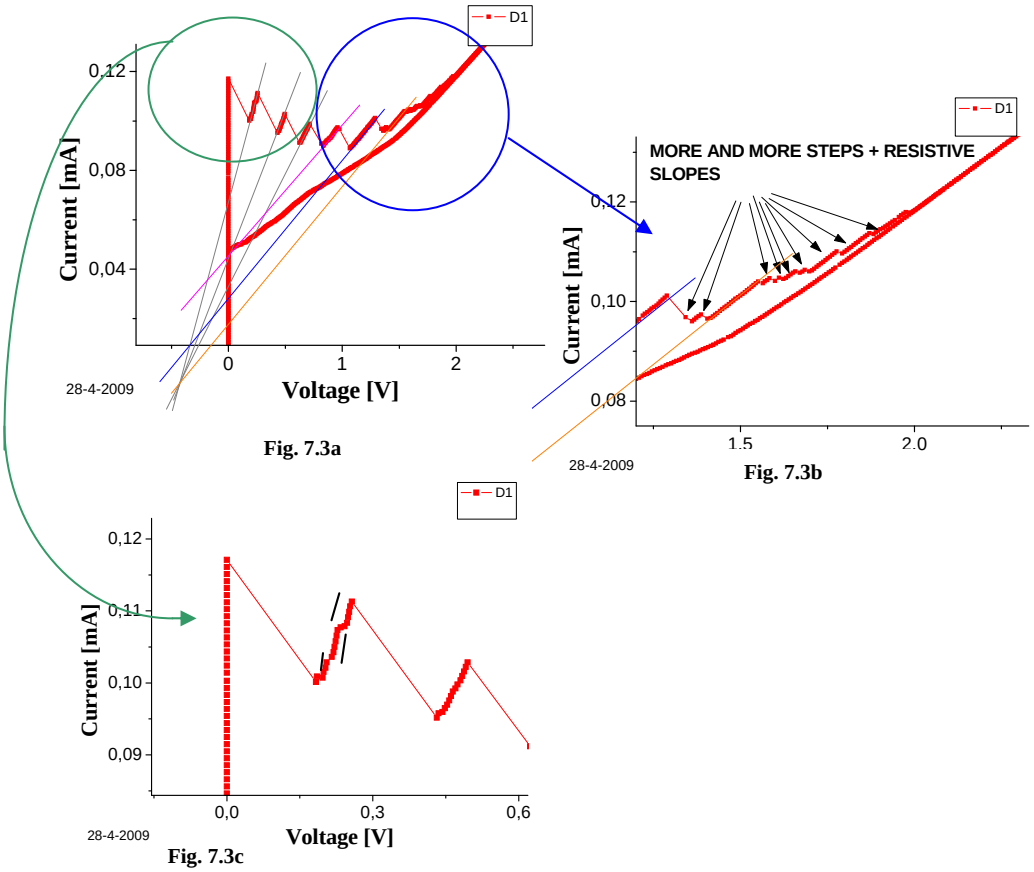


Fig. 7.3a

Fig. 7.3b

Fig. 7.3c

In Fig.7.3 the positive branches of IV curve as measured on a 150nm width nanowire is presented for a NbN(8nm)/$Ni_{0.67}Cu_{0.33}$(3nm) on MgO (see caption for details). The curves show the presence of several steps both on the polarization and return branches. Each of them presents a different slope. In some cases, slopes increase by current (see grey lines in fig 7.3a), but mostly behave randomly. Remembering that these meander DUTs are a series of parallel bridges, we believe that curves show the S/N transitions of various nanowires characterized by slightly different critical currents. Nevertheless, in some plot it is possible to count more than 18 jumps/slopes corresponding to the 6 x 3 wires. This result suggests a more exotic but physically possible explanation in terms of multiple point transitions related to the presence of phase slip centers within devices. An example, considering Fig.7.3a that grey lines point out 3 resistive transitions whose slopes increase by increasing current; they are followed by other transitions whose slopes decrease indicating a different resistive behaviour. Fig.3b and c emphasize multiple jumps. The situation is quite complex to describe completely, and we don't exclude the possibility that the observed behaviour results from both superconducting-to-normal transitions in the different nanowires and potential phase slip centers activated by the bias current and biasing.

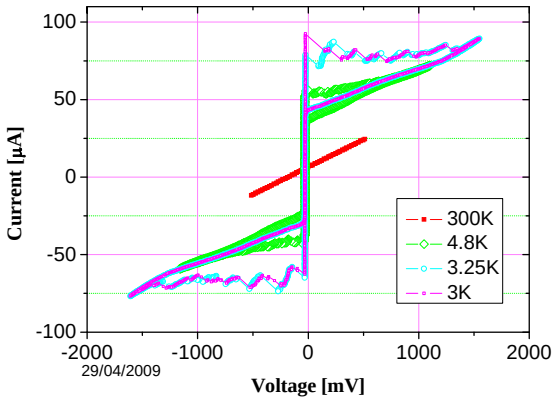


**Fig. 7.4** Current-Voltage (IV) curves of a meander shaped device NbN(8nm)/$Ni_{0.60}Cu_{0.40}$(3nm) based, bridge line width 200nm, 6 series by 3 parallel bridges(D4). IV curves acquired at different temperatures. Corresponding critical current variation inversely follows the changing T, as expected. Red curve :T=300K; green rombs curve : T=4.8K and $I_c$=56uA; cyan circles curve: T=3.25K and $I_c$=78uA; magenta little squares :T=3K and Ic=92uA; red full squares, T=298K,$R_{nn}$=27KΩ.

In Fig. 7.4 is presented the temperature dependence of the current-voltage characteristics IV curves of a meander NbN(8nm)/$Ni_{0.60}Cu_{0.40}$(3nm) (see caption for details): the critical current increases by lowering the temperature as expected. Nevertheless, it is interesting to note that the device D4 (line width 200nm) passed from an Ic=90μA to 56μA after one run of measurement: unfortunately, running time, cooling cycles and probably the laser irradiation contribute to some damage, and this reduced the number of devices useful for laser experiments. The degradation of both Ic and Rnn (after two irradiation tests, the latter passed form 24kΩ to 27kΩ) reveals that probably the fabrication process is not yet optimized for such applications, and hence further feedbacks are needed.

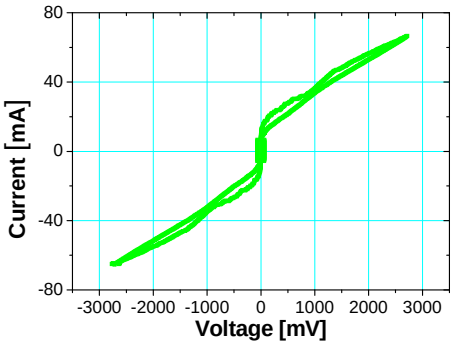


**Fig. 7.5** Current-Voltage (IV) curves of a meander shaped device NbN(8nm)/ $Ni_{0.60}Cu_{0.40}$(3nm), line width 300nm, 6 series by 3 parallel bridges (B2), T=4.2K , Ic=20μA,$R_{nn}$ =46kΩ.

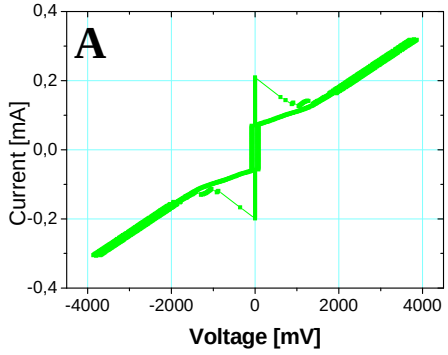


**Fig. 7.6** Current-Voltage (IV) curves of a meander shaped device NbN(8nm)/ $Ni_{0.60}Cu_{0.40}$(3nm) based, bridge line width 500nm, 6 series by 3 parallel bridges; T=4.2K: fig. **A** sample A4 , Ic=200uA,$R_{nn}$ =14kΩ.

In the case of 500nm linewidth meander a LC low-pass filtering has been added, introducing a cutting frequency of about 500MHz. Such an inductance has been demonstrated to increase the recovery time to superconducting state after the laser pulse absorption (see M. Earnjes [..] et ) by reducing the latching phenomenon. Briefly, after the hot spot has reached the maximum size, the current flows mainly through the load resistor (i.e. 50Ω in the specific case, the characteristic impedance of the used coaxial cable) since $R_{nn}>>R_L$. Then, the recovering of the superconducting state in the perturbed wire causes current to be redirected into it: but if this takes place in a time shorter than the thermal recovering time, then the nanostrip still persists in the resistive state (latching). The additional inductance has the function to delay the flowing back of biasing current into the perturbed nanowire, and allows the relaxation of the hotspot and the recovering of the initial biasing conditions for further detection. In particular, the presence of the inductance (500nH) acts as RF current filter cutting off spurious HF noise (mostly white noise). As a further consequence, the critical current has been observed to increase for enhanced EM shielding.
In Fig. 7.7 the IVCs for several 400nm linewidth nanowires on the same chip are shown. The results suggest the presence of a spread of about 8% in the measured critical current.

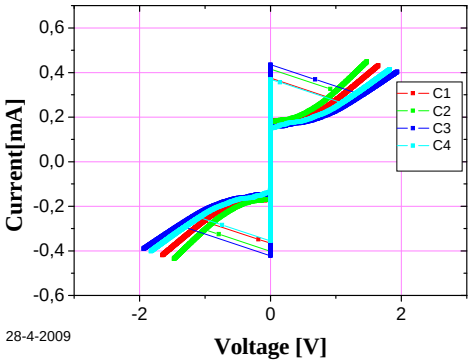


**Fig. 7.7** IV curves on a 400nm bridge width meander structure (sample C); T=4.2K;
Sample C1: Rnn=6KΩ Ic=375uA ; Sample C2: Rnn=5KΩ Ic=415uA
Sample C3: Rnn=7KΩ Ic=435uA ; Sample C4: Rnn=6KΩ Ic=370uA

## 7.3 Photoresponse of NbN and NbN/NiCu meander shaped PD

Photoresponse measurements on the superconducting Nb/NiCu nanolayers is one of the main aims of the thesis. Fig.7.7 shows the photoimpedance on a NbN/NiCu meander structure with a linewidth of 150nm. Moreover, the effect of both wavelenghts (850nm and 1550nm) and duty pulses is shown.

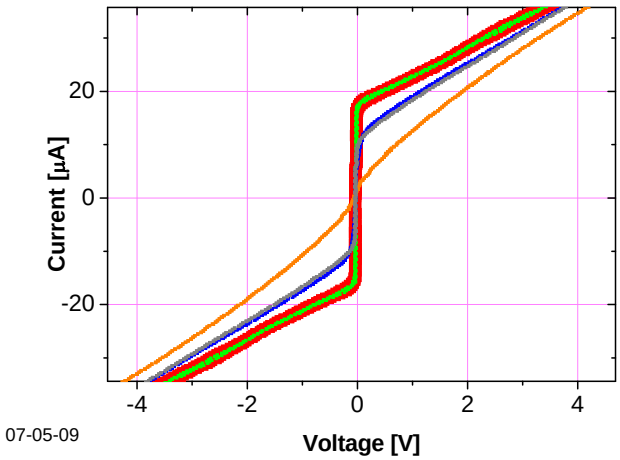


**Fig. 7.7** Laser effects on IVcurve of a meander shaped device(D1) NbN(8nm)/ $Ni_{0.60}Cu_{0.40}$(3nm) based, bridge line width 150nm, 6 series by 3 parallel bridges; Temp.=4.76K; device's $I_c$=17.5 μA; Rnn=24.7KΩ; **red** curve is without laser ; **green** is with diode generated laser by carrier wavelength $\lambda_{LASER}$=850nm; **blue** continuous laser $\lambda_{LASER}$=1550nm; **orange** laser pulsed 20ns duration laser $\lambda_{LASER}$=1550nm; **grey** laser pulsed 6.5ns duration $\lambda_{LASER}$=1550nm.

The first indicative result is that the less powerful laser (N2 laser, λ=850nm) doesn't affect the IV curves, while the infrared laser (N1 laser) acts on the meander more significantly modifying the curve shapes and depressing the critical currents. According to the fluencies calculated in Section 5.5, the sensitivity of the device can be supposed well below the nJ/cm$^2$ limit in fluence. The aim of these tests is not only to verify the response of the superconducting structures to laser sources but also to test their suitability to single photon counting in perspectives. According to literature, it has been demonstrated that the Quantum Efficiency (QE) of meander type NbN based Hot Electron Superconducting Single Photon Detectors (HE-SSPDs) depends on both the wavelengths of incident photons (see Verevkin and al [95], Gol'tsman et al [96]), and the geometrical factors such as the detector filling factor. Accordingly, Table 7.1 summarizes the filling factors of measured devices corresponding to line widths ranging from 150nm to 500nm.

| Bridge Line Width | Bridge Area | Filling Factor |
|---|---|---|
| 150 nm | 3 μm$^2$ | 0.18 |
| 200 nm | 4 μm$^2$ | 0.23 |
| 300 nm | 6 μm$^2$ | 0.27 |
| 400 nm | 8 μm$^2$ | 0.41 |
| 500 nm | 10 μm$^2$ | 0.5 |

**Table 7.1** Filling factors of measured meander devices with a total area of 20x20 μm$^2$ and lateral connections with area 6x(20/3) μm x 500nm= 20 μm$^2$

The aforementioned considerations suggest that the measured photoresponse in low filling factor devices and em coupling (e.g. 150nm), is not due to the wavelenght dependence but mainly to high employed fluences.

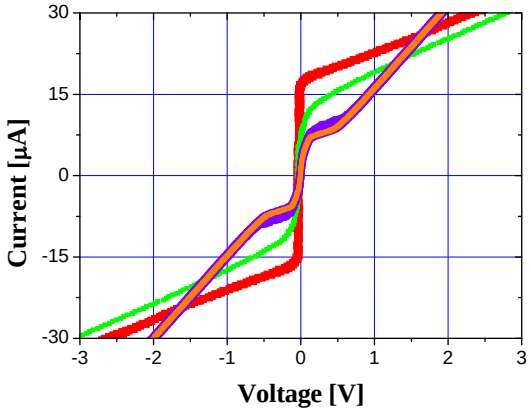


**Fig. 7.8** Laser irradiation effects on IVcurves of two meander shaped devices NbN(8nm)/$Ni_{0.60}Cu_{0.40}$(3nm) and pure NbN(8nm) nanowires with linewidth 150nm, 6 series by 3 parallel bridges, T=4.76K, λ=1550nm, 1mW continuous power. In particular, for NbN(8nm)/NiCu(3nm) the curves refer to presence (green) or not (red) of continuous laser irradiation. The same for NbN(8nm) only meander with (orange) and without (violet) laser irradiation.

Data of Fig. 7.8 demonstrate that the pure NbN device, with exactly the same geometrical properties of the proximized NbN/NiCu nanowire, shows an halved critical current. The increase of the critical current can be a signature of a potential role of pinned vortices inside the proximized structure, probably derived by the clustering of magnetic impurities along the cross section of the superconducting NbN wire. Moreover, it is also very interesting to note the higher sensitivity of the proximized structure to the presence of laser irradiation, a property which is quite promising for photoresponse and photoimpedance following experiments.

In the following we present the experimental results concerning the timings and the "fast" response of the fabricated superconducting detectors even if in a regime far from that of single photon counting. In Fig. 8.8 a typical photoresponse of a NbN(8nm)/NiCu(3nm)
meander to a laser pulse 1550nm 6.5ns . The photoresponse signal is the output of a HF amplifier cascade (gain G=400) while the laser driving voltage signal is reduced in amplitude by a passive attenuator simply to match the oscilloscope scale. The signal frequency of 10MHz has been chosen to operate within the working band of the amplifiers stage, but the frequency bandwidth of the detector is well beyond the amplifiers one.
An appreciable delay between excitation pulse and the detector output of almost 50ns can be noticed, and it's due to electronics.
Voltage output signal faithfully follows laser voltage drive and the laser time-varying pulse intensity: this observation suggests a good linearity of the detector, a fundamental parameter for any further electronic applications. The biasing current has been optimized in order to be enough close and below the critical current Ic of the meander for maintaining the detector in the superconducting state and to allow it the self-resetting.

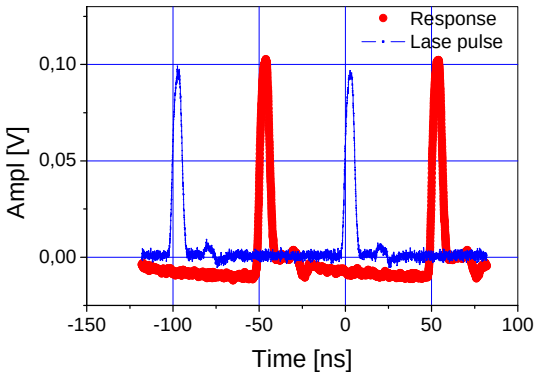

**Fig. 8.8** NbN(8nm)/NiCu(3nm) meander (red) and laser pulse excitation (blu) (the amplitude has been divided by 7) . Meander linewidth 150nm, Ic =17.5uA, T=4.7K, $I_b$=10.4uA ; Ib/Ic=0.6, λ= 1550nm, repetition rate 10MHz, pulse width 6.5ns.

Fig. 8.9 shows a comparison between the photoresponse signals from a NbN only and NbN(8nm)/NiCu(3nm) bilayer devices. The detectors were operated in almost the same Ib/Ic conditions even if with different critical currents. Of course, we expected a large value for NbN proximized bilayer photoresponse signal due to higher bias current with respect to their critical currents, but the factor 2 in the ratio of Ic's (see Fig. 7.9) doesn't explain the one order of magnitude in outlet signal amplitudes.

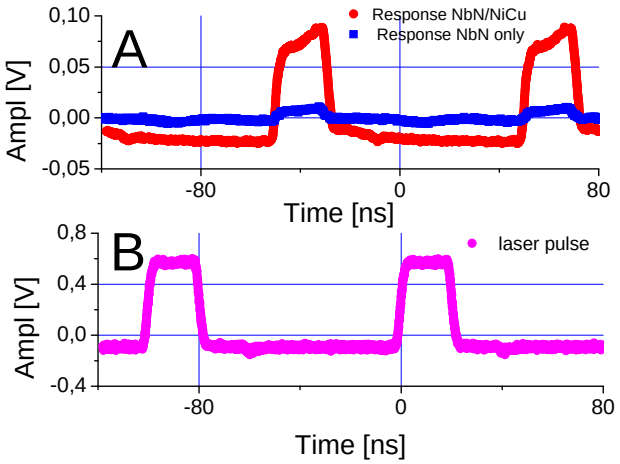


**Fig. 8.9** (A) NbN only and NbN(8nm)/NiCu(3nm) photoresponse; Ic=8uA and Ic=17.5uA respectively ; Ibias/Ic=0.83. (B) Laser pulse excitation signal showing a 20ns width [97]

Data as presented in the previous Sections give a physical picture which is at the moment not completely clear. Let's summarize the main points that can be considered important for a discussion:

(i) the NbN(8nm)/NiCu(3nm) detector shows a larger voltage amplitude with respect to pure NbN device after the irradiation by a λ=1550nm, 20ns laser pulses;
(ii) the two above structures presented different superconducting critical currents, Ic(NbN)=8μA, Ic(NbN/NiCu)=17.5 μA;
(iii) the proximity effect investigation performed on NbN-based bilayers evidenced worse interface properties compared to Nb-based heterostructures;
(iv) in these latter structures the role of proximity effect produced faster but smaller in amplitude photoresponse signals with respect to pure Nb devices.
(v) The IVCs of NbN-based devices showed a lot of steps whose physical interpretation can involve the potential role of phase slip centers which the employed nanosizes could better evidence.

We tried to find a coherent explanation for the above final considerations according to the complex physics involved in the proposed experiments. Nevertheless, to our opinion the role of vortices and their pinning in both Nb and NbN based structures can qualitatively explain most of experimental results.
Far from completeness, we argued that the the presence of a NiCu overlayer can act in creating normal clusters close to the S/F interface or in the S electrode: Fig. 4.11 clearly demonstrates such a possibility by looking at the concentration of Ni along the cross section of the bilayer. The presence of such clusters weakens the superconductivity, but acts in the direction to produce pinning centers for vortices which are present due to the II-type nature of employed superconductors. Such magnetic vortices can be pinned by normal defects amplified by the clustering following the overlayer deposition, resulting in an enhancement of the critical current of the nanowire. The pinning mechanism is widely employed in industrial manufacturing of superconducting cables for obtaining higher critical currents.
The role of vortices in the context of superconducting nanowires for single photon counting is not completely new even if recent: see for example [98]. In order to verify the such a

physical hypothesis, we performed carefull measurements of the temperature dependence of the sample resistance, also in the presence of high magnetic fields up to 1T. The latter measurements are in collaboration with the University of salerno, Dept. Physical Sciences, Prof. C. Attanasio.
Figg. 8.10 shows the R vs T curve for a pure NbN(8nm) nanowire (Fig. 8.10a), and a zoom of the superconducting transition (see fig. 8.10b)

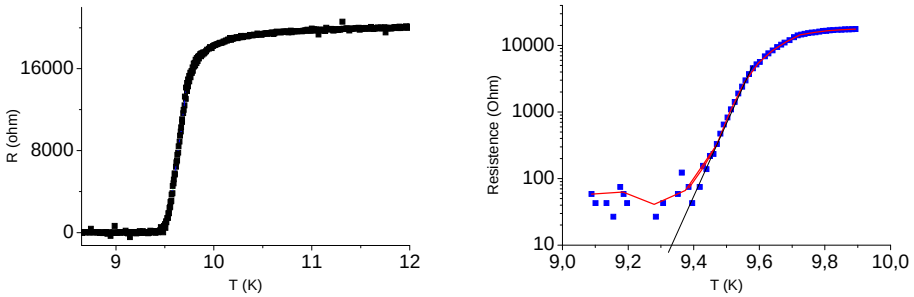


**Fig. 8.10** RvsT behaviour of a pure NbN(8nm) with 300nm linewidth.

The same measurement for a Nb(8nm)/NiCu(3nm) nanowire with 200nm linewidth is presented in Fig. 8.11.

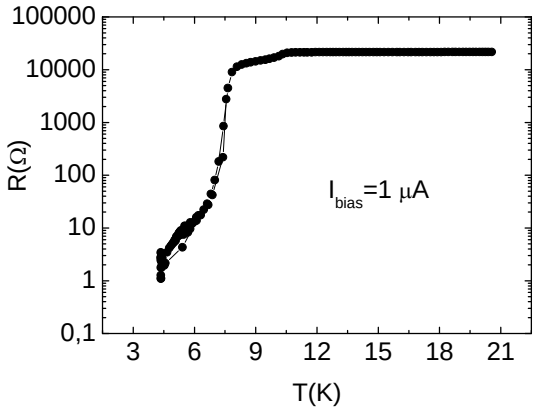


**Fig. 8.11** R vs T behaviour of a pure NbN(8nm) with 200nm linewidth

The behaviour in Fig. 8.11 clearly shows the presence of a second transition approximately at $T_{BKT}$(NbN(8nm)/NiCu(3nm))=6.7K due to the vortices action as predicted by Berezinskii-Kousterlitz-Thouless transition.[99,100]. Also in the case of pure NbN the resistive measurement seems to indicate a less pronounced BKT transition, estimated as $T_{BKT}$(NbN(8nm))≈ 9.3K.

It is important to stress that such values are the result of an analysis which is not complete while the thesis is going to print; nevertheless, the qualitative picture seems to be consistent. In fact, there is the possibility to relate the transport superconducting critical temperature $T_{on}(0)$ at zero field and that one due to vortices i.e. $T_{BKT}$ as explained in Ref. [101,102]

$$\frac{T_{BKT}}{T_c(0)} = \frac{1}{1+0.173\cdot\frac{\varepsilon_{BKT}}{\pi}\cdot R_{SN}\cdot\frac{2e^2}{h}}$$

where $R_{SN}$ is the square resistance of the device, and $\varepsilon_{BKT}$ is the polarizability of the vortices lattice. According to the dualism between a vortex system in a superconductor and a dielectric media, introduced by Buzdin and Feinberg [103] the induction ***B*** acting on vortices

is equivalent to the average charge density in the dielectric media, while compression or dilatation of the vortex lattice can be interpreted as the electrostatic polarization. The values of $R_{SN}$ normalized to different linewidths of measured devices are almost the same. Moreover, the ratios for $T_{BKT}/T_{on}(0)$ were found to be 0.95 and 0.84 for pure NbN and NbN/NiCu, respectively. This means that in the case of proximized bilayers the polarizability of the vortex lattice is larger, and hence its deformability. These quite qualitative considerations should be considered together with the appearance of multi-steps in the IVCs of proximized nanowires, that in this landscape could arise from phase slip centers due to also metallic magnetic clustering/impurities present in the S material, which influence the dynamics of the macroscopic superconducting phase.

**Conclusions**

*Accomplishments*

In summary, the proposed work investigates thin film bilayers formed by a superconductor (e.g. Nb and NbN) in close contac with a normal (ferromagnetic) overlayer (e.g. NiCu) for the realization of superconducting nanowire single photon detectors. The nanowires have been fabricated by using advanced Electron Beam Litography and realizing innovative configurations which combine series and parallel connections. In particular, we tested six blocks of three parallel nanowires connected in series: the choice of this complex geometry has been suggested by the possibility to have large detection area, intrinsic amplification mechanisms of the photoresponse voltage signal, and a control of the inductance of the device.

The characterization of fabricated devices has been performed in terms of transport and optical properties: in particular, the resistance vs temperature and the current-voltage curves have been recorded down to low temperatures, also in the presence of external magnetic fields. Moreover, in order to investigate the electron dynamics and the relaxation times governing the nonequilibrium state after the photon absorption, pure superconductors and proximized bilayers have been characterized in term of transient optical spectroscopy by means of a pump-and-probe optical (100fs time width, 80MHz repetition rate), and the results have been discussed in terms of 2T-model where the role of proximity effect has been included through the electron heat capacity and its dependence on the electron density of states.

The main experimental results have been presented in the last two chapters. In particular, in Chapter 6 the ultrafast optical electrical characterization on both Nb and NbN based bilayers shows an active role played by the weak ferromagnetic normal overlayer deposited on the superconductor. In particular, we demonstrated that the NiCu thin proximized film enhances the electron nonequilibrium temperature, while for NbN the presence of this layer seems to cancel the electron temperature peak, probably due to a faster scattering leading to the equilibrium between the electron and phonon populations. The photoresponse experiments presented in Chapter 7 are quite interesting for different reasons in both Nb- and NbN- based bilayers. In particular, Nb-based proximized micro-bridges demonstrated the possibility to have faster photoresponse voltage signals with lower amplitudes. On the other hand, NbN-based proximized nanowires revealed a higher amplitude (up to one order of magnitude) as a response to 20ns 1550nm laser diode pulses. In both cases, i.e. Nb- and NbN- structures, we observed an enhancement of the critical currents in the presence of the weak ferromagnetic overlayer. All these features address to a potential role played by the vortices which characterize the mixed state of a II-type superconductor such as NbN. Preliminary measurements of transport properties also in the presence of large magnetic fields perpendicular to the nanowire gave the first confirmations to such hypotheses, but this aspects of the research need more investigations.

*Future works*

While the main objectives of the thesis work were demonstrated in terms of innovative proximized structures in nanosized geometries and configurations, there are different tasks that need further investigations including:

- Realizing more measurements of transport properties in the presence of large perpendicular magnetic fields;
- Improving real single-photon experiments and quantum efficiency measurements;

- Investigating the role of vortices in terms of signal mechanism generation and also dark counts effects;
- Improving the detection experiments in the sub-ns range.

[93] G.P.Pepe,L.Parlato,**N.Marrocco** et alter, Novel superconducting proximized heterostructures for ultrafast photodetection,available online www.elsevier.com/locate/cryogenics, Cryogenics 2009, in press
[94] A.Semenov et alter, Analysis of the nonequilibrium photoresponse of superconducting film sto pulsed radiation by use of a two-temperature model, Phys. Rev. 1995,B52,581
[95] A.Verevkin,A.Pearlman,…,N.Gol'tsman and R.Sobolewski,Ultrafast superconducting single-photon detectors for near-infrared-wavelength quantum communications, J.Modern Optics, vol.51,pp.1447-1458,2004
[96] G.N.Gol'tsman,A.Korneev,…,A.Verevkin and R.Sobolewski, Physica Status Solidi C, Conf., vol. 2,no.5,pp. 1480-1488,2005
[97] G.Pepe,L.Parlato,..,N.Marrocco et alter, Photoresponse experiments on NbN proximized nanostructures, Eucas 2009, proceedings.
[98] H.Bartolf,…,A.Semenov, CURRENT ASSISTED, THERMALLY ACTIVATED FLUX LIBERATION IN ULTRATHIN NANOPATTERNED NbN SUPERCONDUCTING MEANDER STRUCTURES, DLR Institute of Planetary Research, Rutherfordstrasse 2, 12489 Berlin, Germany, in press
[99] Z. L. Berezinskii, Zh. Eksp. Teor. Fiz. **59,** 907 (1970); Zh. Eksp. Teor. Fiz. **61**, 1144 (1971).
[100] J. M. Kosterlitz, J. Phys. C **7**, 1046 (1974).
[101] J. E. Mooij, in *Percolation, Localization, and Superconductivity*, edited by A. M. Goldman, S. A. Wolf, *Two-Dimensional Transition in Superconducting Films and Junction Arrays* (Plenum Press, New York, p. 325, 1984).
[102] M. R. Beasley, J. E. Mooij, T. P. Orlando, Phys. Rev. Lett. **42**, 1165 (1979).
[103] A.Buzdin,D.Feinberg,Physica C 256,303-311,1996